UNIVERSITY OF CALIFORNIA SAN DIEGO

Precise Measurement of B-mode polarization signal from the cosmic microwave background with the POLARBEAR and the Simons Array

A Dissertation submitted in partial satisfaction of the
requirements for the degree
Doctor of Philosophy

in

Physics

by

Praween Siritanasak

Committee in charge:

Professor Brian Keating, Chair
Professor Samuel Buss
Professor Dusan Keres
Professor Hans Paar
Professor Gabriel Rebeiz

2018

The Dissertation of Praween Siritanasak is approved, and it is acceptable in quality and form for publication on microfilm and electronically:

_____

_____

_____

_____

_____

Chair

University of California San Diego

2018

DEDICATION

To my family.

EPIGRAPH

The Universe is under no obligation to make sense to you

– Neil deGrasse Tyson

TABLE OF CONTENTS

LIST OF FIGURES

LIST OF TABLES

ACKNOWLEDGEMENTS

The past seven years that I have been working on the POLARBEAR project would have not been possible without the encouragements, friendship, and advisement from many people in my life. First and foremost, I would like to thank my advisor, Professor Brian Keating for providing me with the opportunity, the guidance and the support thoughout my graduate study. It is my pleasure to work with Professor Kam Arnold from whom I have received a lot of technical advice and comments on my work. Also, I would like to thank Professor Hans Paar whose talk opened the CMB world to me.

My grad life would have been difficult without the UCSD crew. I received a lot of advice and encouragement, spent joyful times with, and had many wonderful experiences with Nate Stebor, Dave Boettger, Darcy Barron, Chang Feng, Stephanie Moyerman, Frederick Matsuda, Jon Kaufman, Marty Navaroli, Tucker Elleflot, David Leon, Alex Zahn, Logan Howe, Grant Teply, Nick Galitzki, Max Silva and a especially Lindsay Lowry who made me a chocolateless dessert. I owe countless thanks to my lenslets army - James, Chris, Briana, Kavon, Kevin, Calvin, Jerry, Chris Lee, Daniels, Aanchal, and Wenbo for all the work they have done for me. I also would like to extend my thanks to Laura for bringing Bullitt to the lab.

Working in the group gave me the opportunity to travel to many places, from Berkeley to San Pedro. I thank Adrian Lee for the guidance he provided to me during my stays in Berkeley and Toki for his patience and thoughtful advice. Also, I would like to thanks to Berkeley crew- Ari, Neil, Charlie, Erin, Mike, and Yuji for making my stay in Berkeley enjoyable.

I met many amazing people in Chile during my deployments. I would like to thank all of them for making me feel welcomed. Special thanks to our Chilean team, Nolberto and Jose, who helped us build and operate the telescope in Chile as well as teaching me basic Spanish words and Chilean humor.

Being outside of my home country, Thailand whould have been difficult for me without the Thai community in at UC San Diego. In particular, I am grateful to meet- Eddy, Poy, TK, P'Tee, Sing, and the GoT gang for all experience that we shared together.

Most importantly, I can not come this far without support from my family in Thailand. I would like to express my sincere gratitude to my dad and my mom for their unconditional love. They always support every decision that I made and have always stayed beside me.

Finally, I would like to thank the Royal Thai government scholarship program which gave me an opportunity to study in the US.

Figure 2.1 and 2.2 are reprints of material as it appears in: Z. D. Kermish, P. Ade, A. Anthony, K. Arnold, D. Barron, D. Boettger, J. Borrill, S. Chapman, Y. Chinone, M. A. Dobbs, J. Errard, G. Fabbian, D. Flanigan, G. Fuller, A. Ghribi, W. Grainger, N. Halverson, M. Hasegawa, K. Hattori, M. Hazumi, W. L. Holzapfel, J. Howard, P. Hyland, A. Jaffe, B. Keating, T. Kisner, A. T. Lee, M. Le Jeune, E. Linder, M. Lungu, F. Matsuda, T. Mat- sumura, X. Meng, N. J. Miller, H. Morii, S. Moyerman, M. J. Myers, H. Nishino, H. Paar, E. Quealy, C. L. Reichardt, P. L. Richards, C. Ross, A. Shimizu, M. Shi- mon, C. Shimmin, M. Sholl, P. Siritanasak, H. Spieler, N. Stebor, B. Steinbach, R. Stompor, A. Suzuki, T. Tomaru,

C. Tucker, and O. ZahnThe POLARBEAR experiment, Proc. SPIE 8452, Millimeter, Submillimeter, and Far-Infrared Detectors and Instrumentation for Astronomy VI, 84521C (September 24, 2012); doi:10.1117/12.926354. The dissertation author made essential contributions to many aspects of this work.

Figure 2.3 is reprint of material as it appears in: K. Arnold, P. A. R. Ade, A. E. Anthony, D. Barron, D. Boettger, J. Borrill, S. Chapman, Y. Chinone, M. A. Dobbs, J. Errard, G. Fabbian, D. Flanigan, G. Fuller, A. Ghribi, W. Grainger, N. Halverson, M. Hasegawa, K. Hattori, M. Hazumi, W. L. Holzapfel, J. Howard, P. Hyland, A. Jaffe, B. Keating, Z. Kermish, T. Kisner, M. Le Jeune, A. T. Lee, E. Linder, M. Lungu, F. Matsuda, T. Matsumura, N. J. Miller, X. Meng, H. Morii, S. Moyerman, M. J. Myers, H. Nishino, H. Paar, E. Quealy, C. Reichardt, P. L. Richards, C. Ross, A. Shimizu, C. Shimmin, M. Shimon, M. Sholl, P. Siritanasak, H. Speiler, N. Stebor, B. Steinbach, R. Stompor, A. Suzuki, T. Tomaru, C. Tucker, O. Zahn, The bolometric focal plane array of the POLARBEAR CMB experiment. Proc. SPIE 8452, Millimeter, Submillimeter, and Far-Infrared Detectors and Instrumentation for Astronomy VI, 84521D (September 24, 2012); doi:10.1117/12.927057.The dissertation author made essential contributions to many aspects of this work.

Figures 2.6, 2.7, 2.8 and 2.9 are reprints of material as it appears in: The POLARBEAR Collaboration: P.A.R. Ade, M. Aguilar, Y. Akiba, K. Arnold, C. Baccigalupi, D. Barron, D. Beck, F. Bianchini, D. Boettger, J. Borrill, S. Chapman, Y. Chinone, K. Crowley, A. Cukierman, M. Dobbs, A. Ducout, R. DÃijnner, T. Elleflot, J. Errard, G. Fabbian, S.M. Feeney, C. Feng, T. Fujino, N. Galitzki, A. Gilbert, N. Goeckner-Wald, J. Groh, T. Hamada, G. Hall, N.W. Halverson, M. Hasegawa, M.

Hazumi, C. Hill, L. Howe, Y. Inoue, G.C. Jaehnig, A.H. Jaffe, O. Jeong, D. Kaneko, N. Katayama, B. Keating, R. Keskitalo, T. Kisner, N. Krachmalnicoff, A. Kusaka, M. Le Jeune, A.T. Lee, E.M. Leitch, D. Leon, E. Linder, L. Lowry, F. Matsuda, T. Matsumura, Y. Minami, J. Montgomery, M. Navaroli, H. Nishino, H. Paar, J. Peloton, A. T. P. Pham, D. Poletti, G. Puglisi, C.L. Reichardt, P.L. Richards, C. Ross, Y. Segawa, B.D. Sherwin, M. Silva, P. Siritanasak, N. Stebor, R. Stompor, A. Suzuki, O. Tajima, S. Takakura, S. Takatori, D. Tanabe, G.P. Teply, T. Tomaru, C. Tucker, N. Whitehorn, A. Zahn, A Measurement of the Cosmic Microwave Background B-Mode Polarization Power Spectrum at Sub-Degree Scales from 2 years of POLARBEAR Data , The astrophysical Journal, vol. 848, no.2, p.121, 2017. The dissertation author made essential contributions to many aspects of this work.

Figure 3.1, 3.4 and 3.5 are reprints of material as it appears in: N. Stebor, P. Ade, Y. Akiba, C. Aleman, K. Arnold, C. Baccigalupi, B. Barch, D. Barron, S. Beckman, A. Bender, D. Boettger, J. Borrill, S. Chapman, Y. Chinone, A. Cukierman, T. de Haan, M. Dobbs, A. Ducout, R. Dunner, T. Elleflot, J. Errard, G. Fabbian, S. Feeney, C. Feng, T. Fujino, G. Fuller, A. J. Gilbert, N. Goeckner-Wald, J. Groh, G. Hall, N. Halverson, T. Hamada, M. Hasegawa, K. Hattori, M. Hazumi, C. Hill, W. L. Holzapfel, Y. Hori, L. Howe, Y. Inoue, F. Irie, G. Jaehnig, A. Jaffe, O. Jeong, N. Katayama, J. P. Kaufman, K. Kazemzadeh, B. G. Keating, Z. Kermish, R. Keskitalo, T. Kisner, A. Kusaka, M. Le Jeune, A. T. Lee, D. Leon, E. V. Linder, L. Lowry, F. Matsuda, T. Matsumura, N. Miller, J. Montgomery, M. Navaroli, H. Nishino, H. Paar, J. Peloton, D. Poletti, G. Puglisi, C. R. Raum, G. M. Rebeiz, C. L. Reichardt, P. L. Richards, C. Ross, K. M. Rotermund, Y. Segawa, B. D. Sherwin, I. Shirley, P.

Siritanasak, L. Steinmetz, R. Stompor, A. Suzuki, O. Tajima, S. Takada, S. Takatori, G. P. Teply, A. Tikhomirov, T. Tomaru, B. Westbrook, N. Whitehorn, A. Zahn, O. Zahn; The Simons Array CMB polarization experiment . Proc. SPIE 9914, Millimeter, Submillimeter, and Far-Infrared Detectors and Instrumentation for Astronomy VIII, 99141H (July 20, 2016); doi:10.1117/12.2233103. The dissertation author made essential contributions to many aspects of this work.

Figure 4.6 are reprints of material as it appears in: Darin Rosen, Aritoki Suzuki, Brian Keating, William Krantz, Adrian T. Lee, Erin Quealy, Paul L. Richards, Praween Siritanasak, and William Walker, "Epoxy-based broadband antireflection coating for millimeter-wave optics," Appl. Opt. 52, 8102-8105 (2013). The dissertation author made essential contributions to many aspects of this work.

Figure 4.21 and 4.23 are reprints of material as it appears in: P. Siritanasak, C. Aleman, K. Arnold, A. Cukierman, M. Hazumi, K. Kazemzadeh, B. Keating, T. Matsumura, A. T. Lee, C. Lee, E. Quealy, D. Rosen, N. Stebor, and A. Suzuki, "The broadband anti-reflection coated extended hemispherical silicon lenses for polarbear-2 experiment," Journal of Low Temperature Physics, vol. 184, pp. 553-558, Aug 2016. The dissertation author was the primary author of this paper.

Figure 5.1 was provided by Yuji Chinone.

Praween Siritanasak

La Jolla, CA

Febuary, 2018

VITA

2009	B.Sc. Physics *First-class Honours*, Mahidol University, Bangkok Thailand
2012	M.Sc. Phyiscs, University of California, San Diego, USA
2018	Ph. D. in Physics, University of California, San Diego, USA

PUBLICATIONS

The POLARBEAR Collaboration, P. A. R. Ade, M. Aguilar, Y. Akiba, K. Arnold, C. Baccigalupi, D. Barron, D. Beck, F. Bianchini, D. Boettger, J. Borrill, S. Chapman, Y. Chinone, K. Crowley, A. Cukierman, R. DuÌĹnner, M. Dobbs, A. Ducout, T. Elleflot, J. Errard, G. Fabbian, S. M. Feeney, C. Feng, T. Fujino, N. Galitzki, A. Gilbert, N. Goeckner-Wald, J. C. Groh, G. Hall, N. Halverson, T. Hamada, M. Hasegawa, M. Hazumi, C. A. Hill, L. Howe, Y. Inoue, G. Jaehnig, A. H. Jaffe, O. Jeong, D. Kaneko, N. Katayama, B. Keating, R. Keskitalo, T. Kisner, N. Krachmalnicoff, A. Kusaka, M. L. Jeune, A. T. Lee, E. M. Leitch, D. Leon, E. Linder, L. Lowry, F. Matsuda, T. Matsumura, Y. Minami, J. Montgomery, M. Navaroli, H. Nishino, H. Paar, J. Peloton, A. T. P. Pham, D. Poletti, G. Puglisi, C. L. Reichardt, P. L. Richards, C. Ross, Y. Segawa, B. D. Sherwin, M. Silva-Feaver, P. Siritanasak, N. Stebor, R. Stompor, A. Suzuki, O. Tajima, S. Takakura, S. Takatori, D. Tanabe, G. P. Teply, T. Tomaru, C. Tucker, N. Whitehorn, and A. Zahn, A measurement of the cosmic microwave background B -mode polarization power spectrum at subdegree scales from two years of POLARBEAR data. , The Astrophysical Journal, vol. 848, no. 2, p. 121, 2017.

The POLARBEAR Collaboration: P.A.R. Ade, Y. Akiba, A.E. Anthony, K. Arnold, M. Atlas, D. Barron, D. Boettger, J. Borrill, S. Chapman, Y. Chinone, M. Dobbs, T. Elleflot, J. Errard, G. Fabbian, C. Feng, D. Flanigan, A. Gilbert, W. Grainger, N.W. Halverson, M. Hasegawa, K. Hattori, M. Hazumi, W.L. Holzapfel, Y. Hori, J. Howard, P. Hyland, Y. Inoue, G.C. Jaehnig, A.H. Jaffe, B. Keating, Z. Kermish, R. Keskitalo, T. Kisner, M. Le Jeune, A.T. Lee, E.M. Leitch, E. Linder, M. Lungu, F. Matsuda, T. Matsumura, X. Meng, N.J. Miller, H. Morii, S. Moyerman, M.J. Myers, M. Navaroli, H. Nishino, H. Paar, J. Peloton, D. Poletti, E. Quealy, G. Rebeiz, C.L. Reichardt, P.L. Richards, C. Ross, I. Schanning, D.E. Schenck, B. Sherwin, A. Shimizu, C. Shimmin, M. Shimon, P. Siritanasak, G. Smecher, H. Spieler, N. Stebor,

B. Steinbach, R. Stompor, A. Suzuki, S. Takakura, T. Tomaru, B. Wilson, A. Yadav, O. Zahn. A Measurement of the Cosmic Microwave Background B-mode Polarization Power Spectrum at Sub-degree Scales with POLARBEAR. The Astrophysical Journal, 794, 171, 2014. doi:10.1088/0004-637X/794/2/171

The POLARBEAR Collaboration: P.A.R. Ade, Y. Akiba, A.E. Anthony, K. Arnold, M. Atlas, D. Barron, D. Boettger, J. Borrill, S. Chapman, Y. Chinone, M. Dobbs, T. Elleflot, J. Errard, G. Fabbian, C. Feng, D. Flanigan, A. Gilbert, W. Grainger, N.W. Halverson, M. Hasegawa, K. Hattori, M. Hazumi, W.L. Holzapfel, Y. Hori, J. Howard, P. Hyland, Y. Inoue, G.C. Jaehnig, A.H. Jaffe, B. Keating, Z. Kermish, R. Keskitalo, T. Kisner, M. Le Jeune, A.T. Lee, E.M. Leitch, E. Linder, M. Lungu, F. Matsuda, T. Matsumura, X. Meng, N.J. Miller, H. Morii, S. Moyerman, M.J. Myers, M. Navaroli, H. Nishino, H. Paar, J. Peloton, D. Poletti, E. Quealy, G. Rebeiz, C.L. Reichardt, P.L. Richards, C. Ross, I. Schanning, D.E. Schenck, B. Sherwin, A. Shimizu, C. Shimmin, M. Shimon, P. Siritanasak, G. Smecher, H. Spieler, N. Stebor, B. Steinbach, R. Stompor, A. Suzuki, S. Takakura, T. Tomaru, B. Wilson, A. Yadav, O. Zahn. Measurement of the Cosmic Microwave Background Polarization Lensing Power Spectrum with the POLARBEAR Experiment. Phys. Rev. Lett. 113, 021301, 2014. doi:10.1103/PhysRevLett.113.021301

The POLARBEAR Collaboration: P.A.R. Ade, Y. Akiba, A.E. Anthony, K. Arnold, M. Atlas, D. Barron, D. Boettger, J. Borrill, S. Chapman, Y. Chinone, M. Dobbs, T. Elleflot, J. Errard, G. Fabbian, C. Feng, D. Flanigan, A. Gilbert, W. Grainger, N.W. Halverson, M. Hasegawa, K. Hattori, M. Hazumi, W.L. Holzapfel, Y. Hori, J. Howard, P. Hyland, Y. Inoue, G.C. Jaehnig, A.H. Jaffe, B. Keating, Z. Kermish, R. Keskitalo, T. Kisner, M. Le Jeune, A.T. Lee, E.M. Leitch, E. Linder, M. Lungu, F. Matsuda, T. Matsumura, X. Meng, N.J. Miller, H. Morii, S. Moyerman, M.J. Myers, M. Navaroli, H. Nishino, H. Paar, J. Peloton, D. Poletti, E. Quealy, G. Rebeiz, C.L. Reichardt, P.L. Richards, C. Ross, I. Schanning, D.E. Schenck, B. Sherwin, A. Shimizu, C. Shimmin, M. Shimon, P. Siritanasak, G. Smecher, H. Spieler, N. Stebor, B. Steinbach, R. Stompor, A. Suzuki, S. Takakura, T. Tomaru, B. Wilson, A. Yadav, O. Zahn. Evidence for Gravitational Lensing of the Cosmic Microwave Background Polarization from Cross-Correlation with the Cosmic Infrared Background. Phys. Rev. Lett. 112, 131302, 2014. doi:10.1103/PhysRevLett.112.131302

N. Stebor, P. Ade, Y. Akiba, C. Aleman, K. Arnold, C. Baccigalupi, B. Barch, D. Barron, S. Beckman, A. Bender, D. Boettger, J. Borrill, S. Chapman, Y. Chinone, A. Cukierman, T. de Haan, M. Dobbs, A. Ducout, R. Dunner, T. Elleflot, J. Errard, G. Fabbian, S. Feeney, C. Feng, T. Fujino, G. Fuller, A. J. Gilbert, N. Goeckner-Wald,

J. Groh, G. Hall, N. Halverson, T. Hamada, M. Hasegawa, K. Hattori, M. Hazumi, C. Hill, W. L. Holzapfel, Y. Hori, L. Howe, Y. Inoue, F. Irie, G. Jaehnig, A. Jaffe, O. Jeong, N. Katayama, J. P. Kaufman, K. Kazemzadeh, B. G. Keating, Z. Kermish, R. Keskitalo, T. Kisner, A. Kusaka, M. Le Jeune, A. T. Lee, D. Leon, E. V. Linder, L. Lowry, F. Matsuda, T. Matsumura, N. Miller, J. Montgomery, M. Navaroli, H. Nishino, H. Paar, J. Peloton, D. Poletti, G. Puglisi, C. R. Raum, G. M. Rebeiz, C. L. Reichardt, P. L. Richards, C. Ross, K. M. Rotermund, Y. Segawa, B. D. Sherwin, I. Shirley, P. Siritanasak, L. Steinmetz, R. Stompor, A. Suzuki, O. Tajima, S. Takada, S. Takatori, G. P. Teply, A. Tikhomirov, T. Tomaru, B. Westbrook, N. Whitehorn, A. Zahn, O. Zahn; The Simons Array CMB polarization experiment . Proc. SPIE 9914, Millimeter, Submillimeter, and Far-Infrared Detectors and Instrumentation for Astronomy VIII, 99141H (July 20, 2016); doi:10.1117/12.2233103.

P. Siritanasak, C. Aleman, K. Arnold, A. Cukierman, M. Hazumi, K. Kazemzadeh, B. Keating, T. Matsumura, A. T. Lee, C. Lee, E. Quealy, D. Rosen, N. Stebor, and A. Suzuki, The broadband anti-reflection coated ex- tended hemispherical silicon lenses for polarbear-2 experiment, Journal of Low Temperature Physics, vol. 184, pp. 553âĂŞ558, Aug 2016.

D. Rosen, A. Suzuki, B. Keating, W. Krantz, A. T. Lee, E. Quealy, P. L. Richards, P. Siritanasak, and W. Walker, âĂIJEpoxy-based broadband antireflection coating for millimeter-wave optics,âĂİ Appl. Opt., vol. 52, pp. 8102âĂŞ8105, Nov 2013.

D. Barron, P. A. R. Ade, Y. Akiba, C. Aleman, K. Arnold, M. Atlas, A. Bender, J. Borrill, S. Chapman, Y. Chinone, A. Cukierman, M. Dobbs, T. Elleflot, J. Errard, G. Fabbian, G. Feng, A. Gilbert, N. W. Halverson, M. Hasegawa, K. Hattori, M. Hazumi, W. L. Holzapfel, Y. Hori, Y. Inoue, G. C. Jaehnig, N. Katayama, B. Keating, Z. Kermish, R. Keskitalo, T. Kisner, M. Le Jeune, A. T. Lee, F. Matsuda, T. Matsumura, H. Morii, M. J. Myers, M. Navroli, H. Nishino, T. Okamura, J. Peloton, G. Rebeiz, C. L. Reichardt, P. L. Richards, C. Ross, M. Sholl, P. Siritanasak, G. Smecher, N. Stebor, B. Steinbach, R. Stompor, A. Suzuki, J. Suzuki, S. Takada, T. Takakura, T. Tomaru, B. Wilson, H. Yamaguchi, O. Zahn, Development and characterization of the readout system for POLARBEAR-2. Proc. SPIE 9153, Millimeter, Submillimeter, and Far-Infrared Detectors and Instrumentation for Astronomy VII, 915335, 2014. doi:10.1117/12.2055611

K. Arnold, N. Stebor, P. A. R. Ade, Y. Akiba, A. E. Anthony, M. Atlas, D. Barron, A. Bender, D. Boettger, J. Borrill, S. Chapman, Y. Chinone, A. Cukierman, M. Dobbs, T. Elleflot, J. Errard, G. Fabbian, C. Feng, A. Gilbert, N. Goeckner-Wald, N. W. Halverson, M. Hasegawa, K. Hattori, M. Hazumi, W. L. Holzapfel, Y. Hori,

Y. Inoue, G. C. Jaehnig, A. H. Jaffe, N. Katayama, B. Keating, Z. Kermish, R. Keskitalo, T. Kisner, M. Le Jeune, A. T. Lee, E. M. Leitch, E. Linder, F. Matsuda, T. Matsumura, X. Meng, N. J. Miller, H. Morii, M. J. Myers, M. Navaroli, H. Nishino, T. Okamura, H. Paar, J. Peloton, D. Poletti, C. Raum, G. Rebeiz, C. L. Reichardt, P. L. Richards, C. Ross, K. M. Rotermund, D. E. Schenck, B. D. Sherwin, I. Shirley, M. Sholl, P. Siritanasak, G. Smecher, B. Steinbach, R. Stompor, A. Suzuki, J. Suzuki, S. Takada, S. Takakura, T. Tomaru, B. Wilson, A. Yadav, O. Zahn. The Simons Array: expanding POLARBEAR to three multi-chroic telescopes. Proc. SPIE 9153, Millimeter, Submillimeter, and Far-Infrared Detectors and Instrumentation for Astronomy VII, 91531F, 2014. doi: 10.1117/12.2057332

Y. Inoue, N. Stebor, P. A. R. Ade, Y. Akiba, K. Arnold, A. E. Anthony, M. Atlas, D. Barron, A. Bender, D. Boettger, J. Borrilll, S. Chapman, Y. Chinone, A. Cukierman, M. Dobbs, T. Elleflot, J. Errard, G. Fabbian, C. Feng, A. Gilbert, N. W. Halverson, M. Hasegawa, K. Hattori, M. Hazumi, W. L. Holzapfel, Y. Hori, G. C. Jaehnig, A. H. Jaffe, N. Katayama, B. Keating, Z. Kermish, Reijo Keskitalo, T. Kisner, M. Le Jeune, A. T. Lee, E. M. Leitch, E. Linder, F. Matsuda, T. Matsumura, X. Meng, H. Morii, M. J. Myers, M. Navaroli, H. Nishino, T. Okamura, H. Paar, J. Peloton, D. Poletti, G. Rebeiz, C. L. Reichardt, P. L. Richards, C. Ross, D. E. Schenck, B. D. Sherwin, P. Siritanasak, G. Smecher, M. Sholl, B. Steinbach, R. Stompor, A. Suzuki, J. Suzuki, S. Takada, S. Takakura, T. Tomaru, B. Wilson, A. Yadav, H. Yamaguchi, O. Zahn. Thermal and optical characterization for POLARBEAR-2 optical system. Proc. SPIE 9153, Millimeter, Submillimeter, and Far-Infrared Detectors and Instrumentation for Astronomy VII, 91533A (August 19, 2014). doi:10.1117/12.2055572

D. Barron, P. Ade, A. Anthony, K. Arnold, D. Boettger, J. Borrill, S. Chapman, Y. Chinone, M. Dobbs, J. Edwards, J. Errard, G. Fabbian, D. Flanigan, G. Fuller, A. Ghribi, W. Grainger, N. Halverson, M. Hasegawa, K. Hattori, M. Hazumi, W. Holzapfel, J. Howard, P. Hyland, G. Jaehnig, A. Jaffe, B. Keating, Z. Kermish, R. Keskitalo, T. Kisner, A. T. Lee, M. Le Jeune, E. Linder, M. Lungu, F. Matsuda, T. Matsumura, X. Meng, N. J. Miller, H. Morii, S. Moyerman, M. Meyers, H. Nishino, H. Paar, J. Peloton, E. Quealy, G. Rebeiz, C. L. Reichart, P. L. Richards, C. Ross, A. Shimizu, C. Shimmin, M. Shimon, M. Sholl, P. Siritanasak, H. Spieler, N. Stebor, B. Steinbach, R. Stompor, A. Suzuki, T. Tomaru, C. Tucker, A. Yadav, O. Zahn. The POLARBEAR Cosmic Microwave Background Polarization Experiment. J. Low Temp. Phys. Vol. 176, 5-6, pp 726-732, 2014. doi:10.1007/s10909-013-1065-5

A. Suzuki, P. Ade, Y. Akiba, C. Aleman, K. Arnold, M. Atlas, D. Barron, J. Borrill, S. Chapman, Y. Chinone, A. Cukierman, M. Dobbs, T. Elleflot, J. Errard, G.

Fabbian, G. Feng, A. Gilbert, W. Grainger, N. Halverson, M. Hasegawa, K. Hattori, M. Hazumi, W. Holzapfel, Y. Hori, Y. Inoue, G. Jaehnig, N. Katayama, B. Keating, Z. Kermish, R. Keskitalo, T. Kisner, A. Lee, F. Matsuda, T. Matsumura, H. Morii, S. Moyerman, M. Myers, M. Navaroli, H. Nishino, T. Okamura, C. Reichart, P. Richards, C. Ross, K. Rotermund, M. Sholl, P. Siritanasak, G. Smecher, N. Stebor, R. Stompor, J. Suzuki, S. Takada, S. Takakura, T. Tomaru, B. Wilson, H. Yamaguchi, O. Zahn. The POLARBEAR-2 experiment. J. Low Temperature Physics, 2014. doi:10.1007/s10909-014-1112-x

H. Nishino, P. Ade, Y. Akiba, A. Anthony, K. Arnold, D. Barron, D. Boettger, J. Borrill, S. Chapmann, Y. Chinone, M. A. Dobbs, J. Errard, G. Fabbian, C. Feng, D. Flanigan, G. Fuller, A. Ghribi, W. Grainger, N. Halverson, M. Hasegawa, K. Hattori, M. Hazumi, W. L. Holzapfel, J. Howard, P. Hyland, Y. Inoue, A. Jaffe, G. Jaehnig, Y. Kaneko, N. Katayama, B. Keating, Z. Kermish, N. Kimura, T. Kisner, A. T. Lee, M. Le Jeune, E. Linder, M. Lungu, F. Matsuda, T. Matsumura, N. J. Miller, H. Morii, S. Moyerman, M. J. Myers, R. O'Brient, T. Okamura, H. Paar, J. Peloton, E. Quealy, C. L. Reichardt, P. L. Richards, C. Ross, A. Shimizu, M. Shimon, C. Shimmin, M. Sholl, P. Siritanasak, H. Spieler, N. Stebor, B. Steinbach, R. Stompor, A. Suzuki, J. Suzuki, K. Tanaka, T. Tomaru, C. Tucker, A. Yadav, O. Zahn. POLARBEAR CMB Polarization experiment. Proceedings of the 12th Asia Pacific Physics Conference, 2014. doi:10.7566/JPSCP.1.013107

T. Matsumura, P. Ade, Y. Akiba, C. Aleman, K. Arnold, M. Atlas, D. Barron, J. Borrill, S. Chapman, Y. Chinone, A. Cukierman, M. Dobbs, T. Elleflot, J. Errard, G. Fabbian, G. Feng, A. Gilbert, W. Grainger, N. Halverson, M. Hasegawa, K. Hattori, M. Hazumi, W. Holzapfel, Y. Hori, Y. Inoue, G. Jaehnig, N. Katayama, B. Keating, Z. Kermish, R. Keskitalo, T. Kisner, A. Lee, F. Matsuda, H. Morii, S. Moyerman, M. Myers, M. Navaroli, H. Nishino, T. Okamura, C. Reichart, P. Richards, C. Ross, K. Rotermund, M. Sholl, P. Siritanasak, G. Smecher, N. Stebor, R. Stompor, J. Suzuki, A. Suzuki, S. Takada, S. Takakura, T. Tomaru, B. Wilson, H. Yamaguchi, O. Zahn. Cosmic microwave background B-mode polarization experiment POLARBEAR-2. Proceedings of the 12th Asia Pacific Physics Conference, 2014. doi:10.7566/JPSCP.1.013108

K. Arnold, P.A.R. Ade, A.E. Anthony, D. Barron, D. Boettger, J. Borill, S. Chapman, Y. Chinone, M.A. Dobbs, J. Errard, G. Fabbian, D. Flanigan, G. Fuller, A. Ghribi, W. Granger, N. Halverson, M. Hasegawa, K. Hattori, W.L. Holzapfel, J. Howard, P. Hyland, A. Jaffe, B. Keating, Z. Kermish, T. Kisner, M. Le Jeune, A.T. Lee, E. Linder, M. Lungu, F. Matsuda, T. Matsumura, N.J. Miller, X. Meng, H. Morii, S.

Moyerman, M.J. Myers, H. Nishino, H. Paar, E. Quealy, P.L. Richards, C. Reichardt, C. Ross, A. Shimizu, C. Shimmin, M. Shimon, M. Sholl, P. Siritanasak, H. Spieler, N. Stebor, B. Steinbach, R. Stompor, A. Suzuki, T. Tomaru, C. Tucker, and O. Zahn. The bolometric focal plane array of the POLARBEAR CMB experiment. Proceedings of the Society of Photo-optical Instrumentation Engineers (SPIE), 8452 (49), 2012. doi:10.1117/12.927057

Z. Kermish, P.A.R. Ade, K. Arnold, A.E. Anthony, D. Barron, D. Boettger, J. Borill, S. Chapman, Y. Chinone, M.A. Dobbs, J. Errard, G. Fabbian, D. Flanigan, G. Fuller, A. Ghribi, W. Granger, N. Halverson, M. Hasegawa, K. Hattori, W.L. Holzapfel, J. Howard, P. Hyland, A. Jaffe, B. Keating, T. Kisner, M. Le Jeune, A.T. Lee, E. Linder, M. Lungu, F. Matsuda, T. Matsumura, N.J. Miller, X. Meng, H. Morii, S. Moyerman, M.J. Myers, H. Nishino, H. Paar, E. Quealy, P.L. Richards, C. Reichardt, C. Ross, A. Shimizu, C. Shimmin, M. Shimon, M. Sholl, P. Siritanasak, H. Spieler, N. Stebor, B. Steinbach, R. Stompor, A. Suzuki, T. Tomaru, C. Tucker, and O. Zahn. The POLARBEAR experiment. Proceedings of the Society of Photo-optical Instrumentation Engineers (SPIE), 8452 (48), 2012. doi:10.1117/12.926354

T. Tomaru, M. Hasumi, A.T. Lee, P.A.R. Ade, K. Arnold, D. Barron, J. Borrill, S. Chapman, Y. Chinone, M.A. Dobbs, J. Errard, G. Fabbian, A. Ghribi. W. Grainger, N. Halverson, M. Hasegawa, K. Hattori, W.L. Holzapfel, Y. Iuoue, S. Ishii, Y. Kaneko, B. Keating, Z. Kermish, N. Kimura, T. Kisner, W. Kranz, F. Matsuda, T. Matsumura, H. Morii, M.J. Myers, H. Nishino, T. Okamura, E. Quealy, C.L. Reichards, P.L.Richards, D. Rosen, C. Ross, A. Shimizu, M. Sholl, P. Siritanasak, P. Smith, N. Stebor, R. Stompor, A. Suzuki, J. Suzuki, S. Takada, K. Tanaka and O. Zahn. The POLARBEAR-2 experiment. Proceedings of the Society of Photo-optical Instrumentation Engineers (SPIE), 8452 (53), 2012. doi:10.1117/12.926158

T. Matsumura, P.A.R. Ade, K. Arnold, D. Barron, J. Borrill, S. Chapman, Y. Chinone, M.A. Dobbs, J. Errard, G. Fabbian, A. Ghribi. W. Grainger, N. Halverson, M. Hasegawa, M. Hasumi, K. Hattori, W.L. Holzapfel, Y. Iuoue, S. Ishii, Y. Kaneko, B. Keating, Z. Kermish, N. Kimura, T. Kisner, W. Kranz, A.T. Lee, F. Matsuda, T. Matsumura, H. Morii, M.J. Myers, H. Nishino, T. Okamura, E. Quealy, C.L. Reichards, P.L. Richards, D. Rosen, C. Ross, A. Shimizu, M. Sholl, P. Siritanasak, P. Smith, N. Stebor, R. Stompor, A. Suzuki, J. Suzuki, S. Takada, K. Tanaka and O. Zahn. et al. POLARBEAR-2 optical and polarimeter designs. Proceedings of the Society of Photo-optical Instrumentation Engineers (SPIE), 8452 (124), 2012. doi:10.1117/12.926770

ABSTRACT OF THE DISSERTATION

Precise Measurement of B-mode polarization signal from the cosmic microwave background with the POLARBEAR and the Simons Array

by

Praween Siritanasak

Doctor of Philosophy in Physics

University of California San Diego, 2018

Professor Brian Keating, Chair

Throughout history, human beings have always sought to answer the question "what was the origin of the universe?" The Cosmic Microwave Background (CMB) is one of the most essential scientific tools that will help us better understand the universe. The temperature maps of the CMB have allowed us to study the nature of the early universe through the standard ΛCDM model as well as to describe

its evolution. Nevertheless, many questions remain. The next step in finding the answer lies in the measurement of the B-mode polarization of the CMB. These faint signals from the primordial universe are expected to be key pieces of evidence of the inflationary gravitational wave. Successful detection of this B-mode polarization would not only serve as direct evidence of the inflation theory but also lead to constraining of inflationary model and the energy scale of inflation. Moreover, the gravitational lensing of CMB E-mode polarization to B-mode polarization signal at small angular scales will allow us to trace back to the distribution of matter in our universe.

This dissertation describes the details of the POLARBEAR instrument which is designed to detect CMB B-mode polarization. The results from the first and second observational season are also described. Furthermore, this dissertation discusses the development of the Simons Array instrument, which is the expansion of POLARBEAR with expanded capabilities and increased sensitivity. The Simons Array is scheduled to deploy in 2018.

Chapter 1

Introduction

One of the philosophical questions that humanity always seeks an answer to is "What caused the origin of the universe?" Around 12th century BC, the ancient Indian Rigveda said that the universe originated from the monistic Hiranyagarbha (the 'golden womb' or 'golden egg') [1]. In the 5th century BC, the ancient Greek philosopher named Anaxagoras of Clazomenae propounded an idea that *nous* (intellect or mind) was the motive cause of the cosmos and the original state of the universe was a mixture of all its ingredients, but the mixture is not entirely uniform [2]. Humanity never have a chance to prove any hypotheses until 1964, when the cosmic microwave background (CMB) radiation was accidentally discovered by two scientists at the Bell Telephone Laboratories in New Jersey, Penzias and Wilson. Their discovery led to a new era of modern cosmology [3]. Another milestone in the field of CMB observation happened in 1990 when the Cosmic Background Explorer (COBE) satellite showed that the CMB exhibits a nearly perfect black body spectrum, a major supporting

pieces of evidence of the Big Bang theory. In this chapter, I will walk you through what is the CMB. More specifically what is the CMB polarization, the current status of its measurement, and its role in modern cosmology.

1.1 Modern Cosmology

In November 1915, Albert Einstein presented what is now known as the theory of general relativity (GR) which became the fundamental groundwork for all subsequence development of modern cosmology. This theory enables us to ask questions with testable answers about the universe such as "How the universe began", and "Why are we here?". One of the widely accepted answers is that our universe started from a high temperature, high-density state then expanded and gradually cooled down to the state as we see today. This model of the origin of the universe is known as the "Big Bang theory".

1.1.1 The Expanding Universe

Before we discuss the expanding universe, I will first introduce the fundamental assumption of modern cosmology which states that the distribution of mass and energy of universe will be the same everywhere (homogeneous), and any point in space is the same (isotropy). In another words, "There is nothing special about our location in the universe" [4]. This assumption is known as the Cosmological principle. While this principle holds on a scale larger than 100 Mpc, it is invalid on small scales. For example, consider multiple spheres in the universe with a radius of

less than 3 AU. There is a high probability that some of these spheres will contain stars while some will not thus making these spheres very different from one another.

The key evidence that proved the universe is expanding is Hubble's law. The basis of this law was first derived from General Relativity in 1927 by Georges Lemaître [5]. It was popularized after Edwin Hubble showed the velocity of distant galaxies is proportional to their distance from the Earth.

$$v = H_0 r \tag{1.1}$$

where H_0 is the Hubble constant. Hubble's law serves as a cornerstone of the expanding universe theory. One of the conceptual models that helps illustrate this idea is the balloon model showed in Figure 1.1. Consider two dots on the balloon's surface seperate from each other by the distance χ. Once the balloon is inflated, two dots move futher away from each other, and the distance between these dots increases by the scale factor, a.

1.1.2 The General Relativity

In General Relativity, we can use 4x4 metric tensor to describe the four-dimensional space-time coordinate. The curvature of the universe can be expressed in metric $g_{\mu\nu}$. We can write down the distance between events in four-dimensional space-time coordinate as,

$$ds^2 = g_{\mu\nu} dx^\mu dx^\nu \tag{1.2}$$

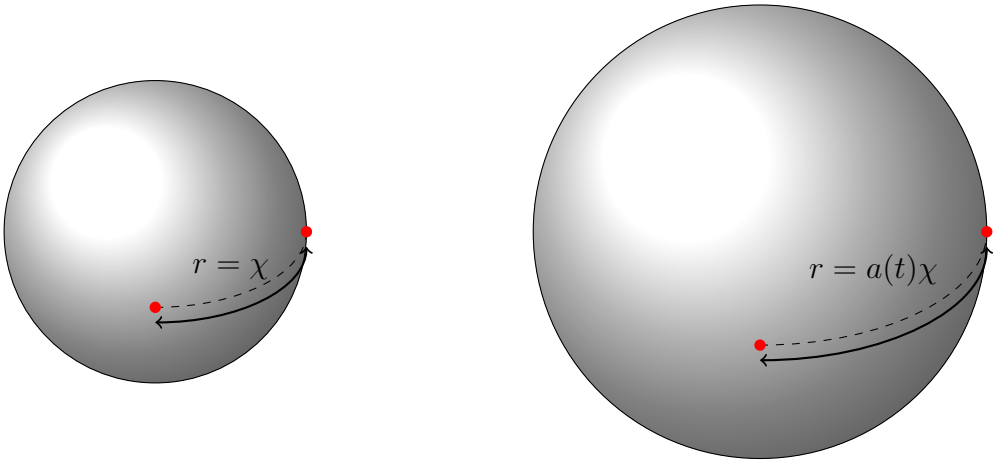

Figure 1.1: This diagram illustrates the expanding universe. On the left, two red dots on the surface of the balloon are separated by a comoving distance χ. As time passes, the balloon is expanding, the dot see each other moving futher away, and the distance between the two red dots becomes $r = a(t)\chi$ where r is a physical distance between two dots and $a(t)$ is a scale factor.

where ds is related to the proper time by $ds^2 = -d\tau^2$. The relationship between space-time curvature and the distribution of mass and energy due to the interaction of the gravitation can be described with a set of ten coupled nonlinear differential equation known as Einstein Field Equations (EFE). The EFE can be written down in the tensor equation as,

$$R_{\mu\nu} - \frac{1}{2}Rg_{\mu\nu} + \Lambda g_{\mu\nu} = 8\pi G T_{\mu\nu}{}^{1} \tag{1.3}$$

where $R_{\mu\nu}$ is the Ricci curvature tensor, R is the scalar curvature, Λ is the cosmological constant, G is the gravitational constant, c is the speed of light in vacuum and $T_{\mu\nu}$ is the stress-energy tensor. Since the field equations are non-linear, it is hard to

[1]We choose to use in natural units where $c = \hbar = k_B = 1$ and thus c is omitted here.

find an exact solution without any assumption to break the symmetries to simplify the equations.

The simplest assumption that can we make is that the distribution of mass and energy of the universe will be the same everywhere (homogeneous) and that all points in space are the same (isotropy). This assumption is known as the Cosmological principle. The metric which follows the cosmological principle is the Friedman-Robertson-Walker (FRW) metric.

$$ds^2 = -dt^2 + a^2(t)\left[\frac{dr^2}{1-kr^2} + r^2(d\theta^2 + \sin^2\theta d\phi^2)\right], k = 0, \pm 1 \tag{1.4}$$

where t, r, θ and ϕ are the coordination of any point in space and time, k is the value that will determine the curvature of space; closed flat or open for $k = -1, 0, 1$ respectively and $a(t)$ is a scale factor that describes the expansion of the universe. The Hubble parameter can be written using the scale factor as,

$$H(t) \equiv \frac{\dot{a}}{a} \tag{1.5}$$

Under the case of the universe that is a perfect isotropic fluid, we can describe the stress-energy tensor as,

$$T^{\mu}_{\nu} = \begin{bmatrix} -\rho & 0 & 0 & 0 \\ 0 & P & 0 & 0 \\ 0 & 0 & P & 0 \\ 0 & 0 & 0 & P \end{bmatrix} \tag{1.6}$$

where ρ and P are density and pressure of the fluid. Using the FRW metric (1.4)

and (1.6), we can write the conservation law in an expanding universe as,

$$\frac{\partial \rho}{\partial t} + \frac{\dot{a}}{a}[3\rho + 3P] = 0 \tag{1.7}$$

We can treat the universe as a perfect fluid and use their equations of state which relates pressure and density.

$$P = \alpha\rho \tag{1.8}$$

where α is the equation of state parameter that is determined by the source of energy. Substituting (1.8) back to (1.7) yields,

$$\rho \propto a^{-3(1+\alpha)} \tag{1.9}$$

This gives us the evolution of energy densities with respect to the scale factor.

The FRW models assume a simple model for the cosmological fluid consisting of three noninteracting components, matter, radiation and vacuum. In each case, the energy densities can be explained as,

1. Non-relativistic partical $\alpha = 0$, for example dust, where pressure is zero. This will create a matter dominated universe

$$\rho_m \backsim \Omega_m \propto a^{-3}. \tag{1.10}$$

2. Relativistic matter $\alpha = 1/3$, for example photons, will create a radiation dom-

inated universe

$$\rho_\gamma \backsim \Omega_\gamma \propto a^{-4}. \tag{1.11}$$

3. Cosmological constant $\alpha = -1$, for example a vacuum energy, will create a cosmological constant-type of vacuum energy dominated universe

$$\rho_\Lambda \backsim \Omega_\Lambda \propto \text{const.} \tag{1.12}$$

From the EFE (1.3), we can seperate the time-time component from the space-space component. $G^{00} = 8\pi T^{00}$, giving us the first Friedman equation

$$\left(\frac{\dot{a}}{a}\right)^2 = \frac{8\pi G\rho}{3} - \frac{k}{a^2} + \frac{\Lambda}{3}. \tag{1.13}$$

The second Friedman equation is

$$\frac{\ddot{a}}{a} = -\frac{4\pi G}{3}(\rho + 3P) + \frac{\Lambda}{3}. \tag{1.14}$$

Here, we defined the critical as,

$$\rho_c \equiv \frac{3H^2(t)}{8\pi G}. \tag{1.15}$$

We can see from the first Friedman equation (1.13) that if the the density of universe is larger than the critical density ($\rho > \rho_c$) then $k = 1$ and space is positively curved. If the density of universe is equal to the critical density ($\rho = \rho_c$), the curvature of space is flat. Finally if the density of universe is less than the critical density ($\rho < \rho_c$)

then space is negatively curved.

1.1.3 The Big Bang Model

The expanding universe as described above is known as the hot Big Bang model. In 1921, Georges Lemaître first proposed the idea that an expanding universe can be traced back to an original singularity. Later, Hubble discovered the galactic redshift and concluded that galaxies are moving apart, reaffirming the hypothesis of the Big Bang model. In 1964, another significant pieces of evidence was discovered when Penzias and Wilson discovered the CMB. (we will discuss this in section 1.2.) Still, many problems arise after the development of the Big Bang theory. For example;

- **The horizon problem** This problem comes from the fact that nothing can travel faster than the finite limit of the speed of light. The CMB photon has been traveling nearly age of the universe to reach us. These photons had no time to travel to the opposite from where they came. Therefore, there is no way that thermal information from two opposites is communicating because nothing can exceed the speed of light. That means the temperature of the CMB should not be uniform because the CMB photon should have been causally disconnected after the time of the last scattering. The result from the CMB map contradicts this hypothesis. It shows a remarkable uniformity of temperature across the whole sky with a variation less than 0.2 mK.

- **The magnetic monopole problem** The Big Bang model predicts that the

early stage of the universe produced a number of heavy stable magnetic monopoles. However, we have never been able to observe any magnetic monopoles.

- **The flatness problem** This problem is associated with the FRW metric (See (1.4)). Introducing the density parameter $\Omega(t) = \rho(t)/\rho_c$, we can rewrite the Friedmann equation as,

$$1 - \Omega(t) = -\frac{k}{R_0^2 H^2(t) a^2(t)}. \tag{1.16}$$

  The current value of Ω can be any number from 0.1 to 10. The result from Planck satellite shows the current Ω is 1 within a margin of error of 0.4% [6]. The result confirms the flatness of our universe. The scale factor $a(t)$ is increasing as the universe is expanding, the right hand side of (1.16) showed that any deviations from $\Omega = 1$ would be amplified with time. This means that at a time of recombination Ω should differ from 1 by less than 10^{-16}. The number 1 seems an arbitrary, oddly unstable value for the geometry of the universe. The universe in the early stage needed to be in a particular condition which come as a surprise to cosmologists as raising another question: why do we live in such a finely tuned universe?

Can we presume the Big Bang model dead because of those problems? Not entirely. It just did not provide us the complete picture of our universe. In fact, these questions encourage us to rethink and find the missing puzzle pieces in the Big Bang model.

1.1.4 The Inflation Theory

Inflation was initially proposed by Alan Guth in 1981 to solve the flatness and horizon problems [7]. Later, it was modified by Andrei Linde, Paul Steinhardt, and Andy Albrecht [8, 9]. The theory states that there is a period of rapid exponential expansion of the universe before the more gradual Big Bang expansion. During this period, a cosmological constant-type of vacuum energy dominated the universe. The inflationary epoch began from 10^{-36} seconds and lasted for only a fraction of a second. During the epoch, the universe increased in size by a factor of $\sim 10^{26}$. This rapid expansion of the universe can answer all three problems raised by the Big Bang theory. In the case of **the horizon problem**, prior the inflationary epoch, the theory allows for distant regions to be in casual contact, thermally equilibrate and achieve a uniform temperature before inflation. For **the magnetic monopole problem**, the inflation theory allows the primordial universe to have magnetic monopoles prior the inflationary epoch. Because of the expansion during inflation, the density of magnetic monopoles declines rapidly and drops to undetectable levels. The inflation theory also helps solve **the flatness problem**. Imagine you live on the surface of the balloon; you can easily observe that you are living on a curvatured surface. However, once you increase the size of the balloon to the size of Earth, it is hard to see that you are living in a curvature, but rather on a flat surface. According to the inflation theory, our observable universe[2] is just a small portion of the entire universe. It stretches out any initial curvature of the 3-dimensional universe to near

[2]The observable universe is the maximum spherical region of the universe which can be observed from the earth at the present time.

flatness. Moreover, the origin of structure in the universe could be explained by the inflation theory. In the early stage of the universe before the inflation period, the observable universe that we see today was microscopic. Quantum fluctuations in the density of mass-energy in the early universe expanded to a macroscopic scale during the inflation. Higher density regions condensed and became stars, galaxies and formed the large-scale structure.

The inflation also generated the primordial gravitation wave from the tensor perturbations in the gravitational metric. These perturbations are not coupled to the density, so they do not affect the evolution of the large-scale structure that we can observe today. However, they do induce the fluctuation in the CMB and imprint a unique B-mode polarization signal in the CMB.

The inflation theory seems to be the most viable candidate to fullfill the Big Bang model. However, it has yet to be proven by any observed evidence. Proving the inflation theory remains to be one of the most active and challenging field of experimental cosmology. The smoking gun that many cosmologists hunt for is the CMB primordial B-mode polarization. Later in this chapter, we will discuss what the CMB B-mode polarization is and how we can detect it.

1.2 The Cosmic Microwave Background

The CMB was formed billions of years ago during the period known as recombination and is the oldest light that we can observe today. It was first predicted in 1948 by Gamow, Alpher, and Herman [10, 11] with an estimated temperature of

5 K. In 1964, Penzias and Wilson accidentally discovered the CMB which led them to win the Nobel Prize in 1978. The CMB has two important properties. First, the CMB radiation is nearly-perfect "black-body radiation". The Far-InfraRed Absolute Spectrophotometer (FIRAS) instrument on the COBE satellite measured the near-perfect black body temperature of the CMB to be 2.725 ± 0.002 K (See more detail in Figure 1.2). Second, the CMB radiation is isotropic on large scales and anisotropic on small scales. The temperature anisotropy can be expressed as,

$$\frac{\Delta T}{T}(\theta, \phi) = \frac{T(\theta, \phi) - T_0}{T_0} \tag{1.17}$$

which gives the temperature fluctuation as a fractions of the mean temperature T_0 and an angular position on the sky.

1.2.1 The Formation of the CMB

From the current ΛCDM model[3], the early stage universe can be modeled as a hot dense plasma soup of different particles called the 'baryon-photon' fluid. The reactions in the plasma are in equilibrium. In this period, the universe can be considered as a radiation dominated universe. The plasma is effectively opaque since the mean free path of each photon is very short before colliding with electrons. Photons and electrons are coupled through Thomson scattering. As the universe begins to cool down and expand, its density declines and the reaction rates drop, resulting in increasing mean free paths. The acceleration of the reaction is not enough to keep

[3] ΛCDM is a specific name of the Big Bang cosmological model of the universe which include a cosmological constant Λ, associated with dark matter and cold dark matter, CDM

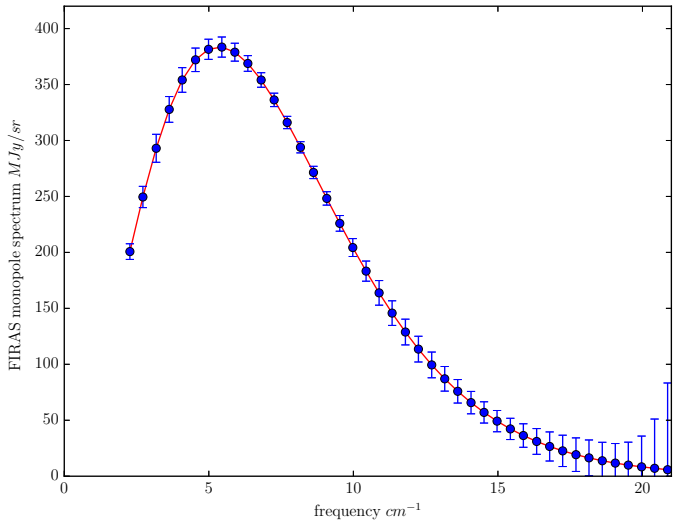

Figure 1.2: Cosmic background radiation monopole spectrum measured by FIRAS instrument on the COBE satellite. The red line shows a theoretical curve of the black body spectrum at 2.725 K. Data is taken from [12]

the particles in thermal equilibrium. This stage is called **decoupling**. Eventually, the universe cooled to an estimated temperature about 3700 K [4]. During this time, the formation of neutral hydrogen is created and the number of free electrons and protons decreases. This reduces the rate of Thomson scattering so that the photon can start to stream freely. This period happened after approximately 300,000 years after the Big Bang, is called **recombination**. As a result, the Universe became transparent, and photons reach present-day observers as the Cosmic microwave background radiation.

1.2.2 The CMB Anisotropy

As discussed earlier, there are small fluctuations or anisotropies in the CMB. There are two sources of anisotropies; **primary anisotropies** which created at the same time as the CMB was generated and **secondary anisotropies** which generated after the recombination era. As we know from Figure 1.2, the CMB spectrum is a nearly perfect blackbody. We can describe this observable of the CMB in the term of a temperature fluctuation as a function of sky direction $\hat{\mathbf{n}}$ as

$$\Theta(\hat{\mathbf{n}}) = \frac{\Delta T}{T}. \tag{1.18}$$

Assuming the fluctuations are Gaussian, we can expand the temperature pattern into multipole moments ℓ which can be correlated to angular seperation on the sky θ as $\ell \approx \pi/\theta$.The term of spherical harmonics $Y_{\ell m}$,

$$\Theta_{\ell m} = \int d\hat{\mathbf{n}} Y^*_{\ell m}(\hat{\mathbf{n}})\Theta(\hat{\mathbf{n}}). \tag{1.19}$$

are fully characterized by their angular power spectrum C_ℓ,

$$\langle \Theta^*_{\ell m}\Theta_{\ell' m'}\rangle = \delta_{\ell\ell'}C_\ell. \tag{1.20}$$

In the small region in the sky, we can assume the sky is flat. The spherical harmonics can be approximated as the ordinary two-dimensional Fourier expansion. In a typical analysis, the power spectrum is usually express as the power per logarithmic interval

in wavenumber, defined as,

$$\Delta_T^2 \equiv \frac{\ell(\ell+1)}{2\pi} C_\ell T^2. \tag{1.21}$$

The fundamental limitation of the CMB power spectra is determined by "cosmic variance". Because of the fact that there is only one universe which we can observe the CMB and there are only $2\ell+1$ samples of the power spectrum in a given multipole moment, especially at very low ℓ. The error can be displayed as the inverse of the square root of the number of possible samples,

$$\Delta C_\ell = \sqrt{\frac{2}{2\ell+1}} C_\ell. \tag{1.22}$$

An example power spectrum is shown in Figure 1.3. This result was measured by Planck satellite which was launched in 2009 and observed the sky until 2013 [13]. Data at low ℓ range (below $\ell = 50$) shows a high uncertainty from cosmic variance. On the large scale, there has not been enough time for the universe to evolve so that we can only see mainly the initial fluctuation. More interestingly, this plot shows the multiple peaks in the power spectrum. Those series of peaks are called the acoustic peaks corresponding to acoustic oscillations of the photon-baryon fluid in the recombination epoch. The first peak is due to the photon-baryon fluid reach to its first maximum compression at decoupling. The position of the first peak also gives us information about the curvature of the universe, showing that our universe is spatially flat. The second peak shows us the amount of matter in the universe, and the third peak indicates the density of dark matter in the universe. The peaks

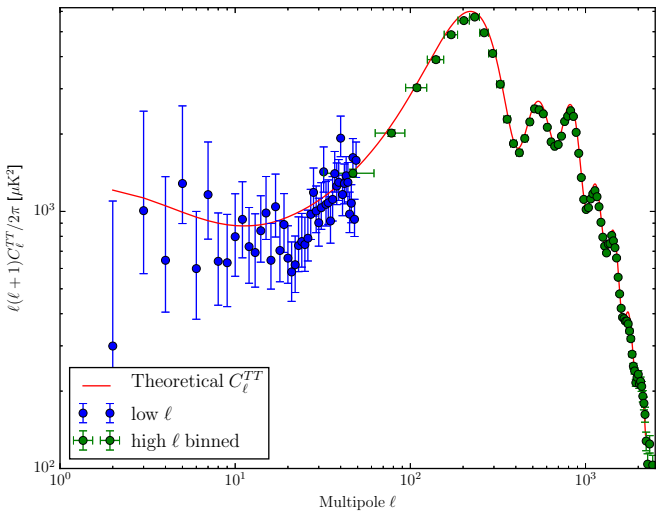

Figure 1.3: The CMB C_ℓ^{TT} power spectrum from the Planck satellite. The result from low ℓ and from high ℓ are shown in blue and green, respectively. The large uncertainties in low ℓ are due to the cosmic variance. A fit to the ΛCDM model is shown in the red solid line. Data is taken from [13].

in higher ℓ are damped as a result of photon diffusion.

1.2.3 The Polarization of CMB

Another feature of the CMB is polarization, a powerful tool for investigating the early universe. The polarized CMB photon is generated from Thomson scattering at the time of decoupling. When an unpolarized photon collided with a free electron, the scattered photon is polarized in the direction perpendicular to the incident direction. That means only the incident photon from quadrupole moment can create a net polarized photon. There are three sources that can generate quadrupole anisotropies the recombination: scalar perturbations, vector perturbations, and tensor perturbations. The first represents the perturbation in the mass-energy density of the fluid at the last scattering. The second is vortical motions of the plasma similar to "eddies" in water. These vector perturbations are predicted to be negligible at the recombination. The third is caused by "the gravitational wave" which are produced from inflation. They created an anisotropic stretching of space and correspondingly the frequency of CMB photons.

It is common to describe the polarization of CMB in the term of the Stokes parameters.

$$\begin{aligned} I &= |E_x|^2 + |E_y|^2, \\ Q &= |E_x|^2 - |E_y|^2, \\ U &= 2\mathbf{Re}(E_x E_y^*), \\ V &= -2\mathbf{Im}(E_x E_y^*). \end{aligned} \tag{1.23}$$

The Stokes parameter I represents the total intensity of the photon, Q rep-

resents the linear polarization in horizontal and vertical direction, U represents the linear polarization in diagonal, and V represent the circular polarization. However, those parameters depend on the choice of the coordinate. For example, parameter Q and U rely on the angle between the polarization axes and the reference frame. A better option is E-mode (electric field like) polarization which is a curl-free component and B-mode (magnetic field like) polarization which is a gradient-free component. E and B mode are non-local quantities and can represent the global properties of polarization field.The relationship between these parameters can be written in 2D Fourier transform space as,

$$\begin{aligned} E(\ell) &= Q(\ell)\cos(2\phi_\ell) + U(\ell)\sin(2\phi_\ell), \\ B(\ell) &= -Q(\ell)\sin(2\phi_\ell) + U(\ell)\cos(2\phi_\ell). \end{aligned} \tag{1.24}$$

where ϕ_ℓ is the angle between X-axis and the polarization direction. And the reverse operation can be expressed as,

$$\begin{aligned} Q(\ell) &= E(\ell)\cos(2\phi_\ell) - B(\ell)\sin(2\phi_\ell), \\ U(\ell) &= E(\ell)\sin(2\phi_\ell) + B(\ell)\cos(2\phi_\ell). \end{aligned} \tag{1.25}$$

Similar to (1.20), the power spectra for temperature, E and B-mode including cross-correlations can be written as,

$$C_\ell^{XY} = \langle \Theta_{\ell m}^{X*} \Theta_{\ell m}^{Y} \rangle, \tag{1.26}$$

with $X, Y \in [T, E, B]$.

The theoretical CMB polarization power spectra are shown in Figure 1.7 using the current ΛCDM parameters. Comparing all three power spectra, C_ℓ^{BB} has the faintest signal across all multipole. Scalar perturbations generate only E-mode polarization, but tensor perturbations produce both E and B-mode polarization. Hence, B-mode polarization becomes the smoking gun for primordial gravitational waves and inflation. Currently, it is a challenging for the CMB experiment community to improve the sensitivity of the instrument for detecting the B-mode polarization CMB. Two primary sources of the primordial B-mode signal are the presence of the gravitational waves at the surface of the last scattering [14, 15] and the lensing of CMB photons between last scattering and our observation from weak gravitational lensing [16, 17].

1.2.4 Gravitational Lensing of the CMB

As photons propagate through the universe since thirteen billion years ago from the surface of the last scattering to the earth, they are randomly deflected by the gravitational force from inhomogeneous mass distribution [16]. This distortion effect can occur in both temperature and polarization anisotropy patterns. The effect on the temperature anisotropy power spectrum is not significant; it will smear out sharp features in the power spectrum [19,20]. However, the effect on the polarization anisotropy can lead to the mixing mode between E and B-mode polarization. The characteristic shapes of primordial B-mode and lensing B-mode are different. The lensing power spectrum has a peak at small angular scale or high multipoles (ℓ) as shown in Figure 1.7. For a high tensor-to-scalar ratio r, the peak of primordial

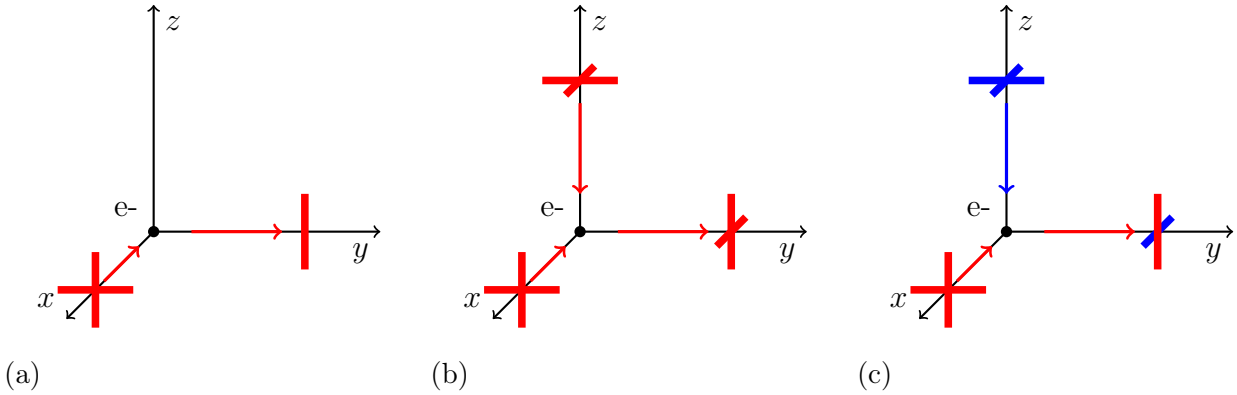

(a) (b) (c)

Figure 1.4: A polarized CMB photon arising from Thomson scattering. Red lines and blue lines represent the polarization of the incident photon. **(a)**. When unpolarized photon from $+\hat{\mathbf{x}}$ direction collides with electron, it will re-emit the photon and scatter to $+\hat{\mathbf{y}}$ whose polarization is perpendicular to the incoming photon. **(b)**. When two incoming photons from $+\hat{\mathbf{x}}$ and $+\hat{\mathbf{z}}$ have the same intensity, there no net polarized photon is produced. **(c)**. Blue (red) lines denote hot (cold) spots. When the intensity of photons varies at 90 degrees(quadrupole moment), the outgoing photon has a polarization intensity along the y-axis greater than x-axis and the linear polarized photon can be created.

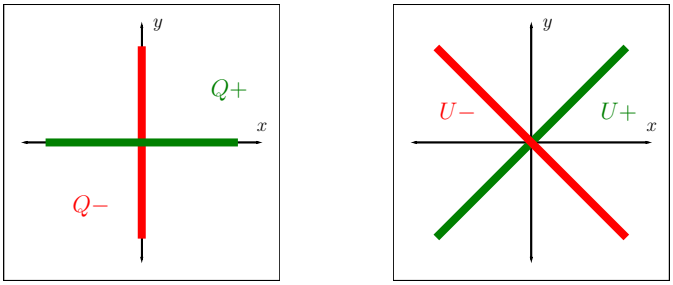

Figure 1.5: An illustration of Strokes parameter Q and U, Q is showed in the left box. Positive Q (green) is a linear polarization along X-axis, and negative Q (red) is a linear polarization along Y-axis. U is showed in a right box. Positive U (green) is a linear polarization with 45 degrees rotation by the X-axis and negative U (red) is a linear polarization with 45 degrees rotation by the Y-axis.

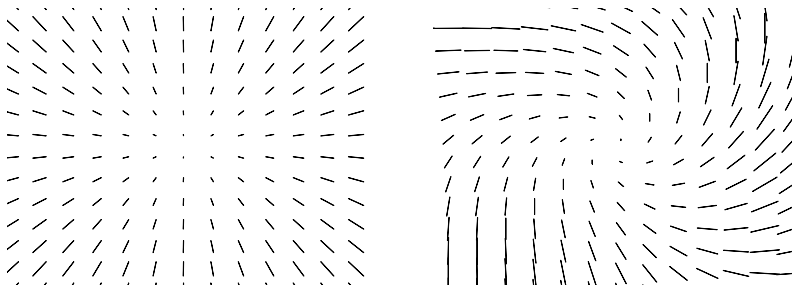

(a) (b)

Figure 1.6: An illustration of E-mode and B-mode polarizations. **(a)**, shows E-mode patterns or curl-free patterns. **(b)**, shows B-mode patterns or gradient-free patterns.

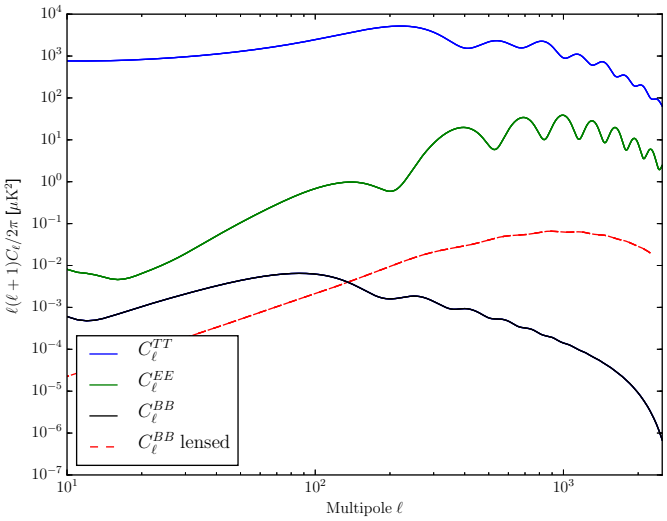

Figure 1.7: Theoretical polarization power spectrum of CMB anisotropies. The blue line is temperature C_ℓ^{TT}, the green line is E-mode polarization C_ℓ^{EE}, the black line is B-mode polarization C_ℓ^{BB} calculated using tensor-to-scalar ratio $r = 0.1$ and the dashed red line is C_ℓ^{BB} from weak gravitational lensing. Power spectrum is calculated from CAMB package [18].

B-mode is still detectable. The analysis for lensing removal is called "de-lensing" is needed to recover the primordial B-mode signal for a small r. The limit on the minimum value of r for the detectable level is around 2×10^{-4} [21].

The lensing signal itself contains useful cosmological information such as a mass distribution across the sky between the surface of the last scattering to now. The correlation between E-mode and B-mode can be used to re-construction the gravitational field and to generate the mass distribution. The shape of the mass distribution will give us constraints on cosmological parameters and its peak is sensitive to a sum of the neutrino masses.

1.2.5 Foreground Contamination

Foreground contamination is one of the main limiting factors for ground-based CMB experiments. There are many sources of foreground contaminants which we have to characterize and remove from the CMB signal including the atmospheric contamination, galactic synchrotron foreground, and interstellar dust.

Atmospheric Contamination

For ground-based experiments, the atmosphere can play a significant role in creating contamination and reducing the sensitivity of the measurement. Water vapor and dioxygen molecules in the atmosphere can absorb photons in millimeter wavelength range. The atmosphere also creates an excess thermal loading to the detectors. The atmospheric contamination is also not a static foreground. For example, wind can change the composition of an atmosphere from time to time. This effect

can generate low-frequency noise in the time-ordered data which can be mitigate by using signal modulation or by faster scan speed. The site location can help to reduce effects from the atmosphere as well. Two locations which have a high elevation and low Precipitable Water Vapor (PWV), such as the South Pole or the Atacama desert in Chile. These locations are considered as the driest places in the world and are the optimal location for a ground-based CMB observation.

Figure 1.8 shows the transmission spectrum from the atmosphere observed at an elevation of 60°. The majority of the absorption comes from water vapor in the air absorption creating lines around 20 and 180 GHz, oxygen with around 60 and 120 GHz, and hydrogen with absorption line around 190 GHz. Futhermore the opacity of the atmosphere at a frequency higher than 300 GHz make it difficult to observe the CMB from the ground.

The emission from the atmosphere is expected to be largely unpolarized, only oxygen molecules can exhibit Zeeman splitting from the earth magnetic field, which creates a circular polarization. Although the CMB is not expected to have a circular polarization, at a large angular scale, $\ell \approx 1$, circular polarization can convert to linear polarization and produce a B-mode signal [22,23]. This B-mode leakage signal can be fixed in Earth's reference frame and seperated from the CMB signal. Hence, this foreground is most likely not expected to create an additional signal to the CMB polarization.

Balloon-borne experiments and satellites experiments, can mitigate foreground contaminants and excess optical loading from the atmosphere, resulting in an increased sensitivity of the detector compared to ground-based experiments. However,

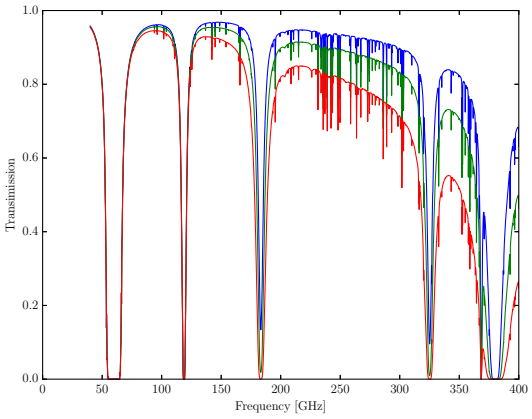

Figure 1.8: Atmospheric transmission in the Llano de Chajnantor, Chile. The plot shows the transmission spectrum of a precipitable water vapor (PWV) of 0.5 mm (blue), 1 mm (green) and 2 mm (red) at elevation 60° and at an altitude of 5,100 meters. Historically, PWV=0.5 mm can be observed around for 25% of a whole year with median of PWV of 1mm. The atmospheric model is calculated using the ATM package [24]

mechanical challenges and weight create a constraint on the size of the focal plane and the number of the detectors.

Galactic Synchrotron Foregrounds

Galactic synchrotron radiation is generated by accelerated cosmic-ray electrons passing through the galactic magnetic field. This radiation has a high impact at frequencies below 70 GHz. Synchrotron emission decreases follows a power law $T \propto \nu^{-\beta}$, where the theoretical spectral index is in the range between 2 and 3, depending on the position and frequency [25].

Interstellar Dust

The polarization from dust emission is one of the major polarized contaminant sources for CMB experiments. The emission from dust dominates at frequencies higer than 70 GHz even at high galactic latitudes has a peak around 2000 GHz. These polarized signals arise from asymmetrical dust grains with sizes around 0.1 μm aligning with the galactic magnetic field. The polarization from dust can create false B-mode polarization. The recent joint analysis of BICEP2/Keck array and Planck data showed that the polarized foreground power from dust can be similar or even larger than the primordial B-mode signal itself [26].

One way of estimating the polarization power from dust is using the publicly available Planck 2015 sky map at 353 GHz then using the power law $T \propto T_0 \nu^{\beta}$ where the spectral index $\beta \approx 2$ to scale down to observing frequencies [27]. Observation of the CMB at multiple frequencies is required to improve the estimation of the polarization for dust. Many of new generation of CMB experiments are deployed with multi-frequencies detectors such as the Simons Array [28], the SPT3G [29], and the AdvACT [30].

Chapter 2

The POLARBEAR Experiment

2.1 Introduction

POLARBEAR is a cosmic microwave background (CMB) polarization experiment; one of the several current experiments aiming to observe evidences of inflation. The POLARBEAR was first assembled for engineering run in 2010 at the Inyo Mountains, California. In late 2011, it was deployed at the James Ax Observatory on Cerro Tocco in the Atacama desert in Northern Chile at an altitude of 5,200 meters. The POLARBEAR receiver was installed on the 2.5 meter Huan Tran Telescope and started observation in 2012. It consists of 1274 polarization-sensitive transition edge sensor (TES) antenna-couple bolometers operating at 250 mK with a spectrum band centered at 148 GHz [31]. The primary goal of the POLARBEAR experiment is to detect small angular scale B-mode signals from gravitational lensing as well as a large angular scale B-mode signals from inflationary gravitational waves. In the

chapter, we will examine the scientific goals behind the project, the POLARBEAR instrumentations, and discuss the result from two season observation result.

2.2 Scientific Goals

As discussed in Chapter 1, one of the most ambitious goals in CMB experiment is to finding an evidence of inflation theory. A detection of the B-mode polarization will provide a direct proof to support the inflationary paradigm and it will help us constrain the cosmological parameters.

Not only primordial gravitational wave from tensor perturbation imprint B-modes signal to the CMB, but also E-modes leaking to B-modes cause by weak gravitational lensing from the large scale structure. This leads to the B-mode polarized signal in small angular scale and limit our ability to measure the tensor-to-scale ratio r as described in Section 1.2.4. Nevertheless, lensing B-modes offer us information about the large scale structure including the constraint on the neutrinos masses and testing the general relativity. The POLARBEAR was designed to characterize B-mode polarization signal on both the large and small angular scales. The observation patches of the POLARBEAR are chosen to minimize the level of dust foreground contamination from the galactic plane overlap with optical and infrared galaxy surveys which enable us to cross-correlate these data for better understanding in the nature of lensing effect. These lensing B-modes have been discovered recently on small angular scales by the POLARBEAR and other experiments [32–35].

2.3 Instrument overview

To distinguish the B-mode signal, we have to design a state-of-the-art receiver with high sensitivity and minimize the systematic effect that can be mixed with the faint B-mode signal. The current technology of a detector development is limited by the photon noise of the thermal background. To increase an overall performance and sensitivity of the receiver, the POLARBEAR utilizes a unique 637 lenslets-coupled focal plane with the center band at 148 GHz with a bandwidth of 38 GHz integrated with cold re-imaging optics. In this section, we will give a brief discussion of the key elements of the design and development of the POLARBEAR experiment.

2.3.1 The Huan Tran Telescope

The Huan Tran Telescope (HTT) is a 2.5 meter diameter telescope at the James Ax observatory on which the POLARBEAR receiver was installed. The HTT is an off-axis Gregorian-Dragone design, consists of two-off axis mirror. The off-axis design was chosen because of the lack of supporting structure on the secondary mirror which is required for an on-axis system that can obstruct a beam and diffract or scatter signal from the ground to the main beam. To minimize the cross-polarization and astigmatism over a large diffraction-limited field of view, the HTT's design is chosen to satisfy the Mizuguchi-Dragone condition.

Figure 2.1 shows the HTT in the Atacama desert, northern Chile and the ray traced optics elements. The HTT precision primary mirror is a 2.5 meter diameter monolithic aluminum alloy mirror that is machined from a single piece of aluminum

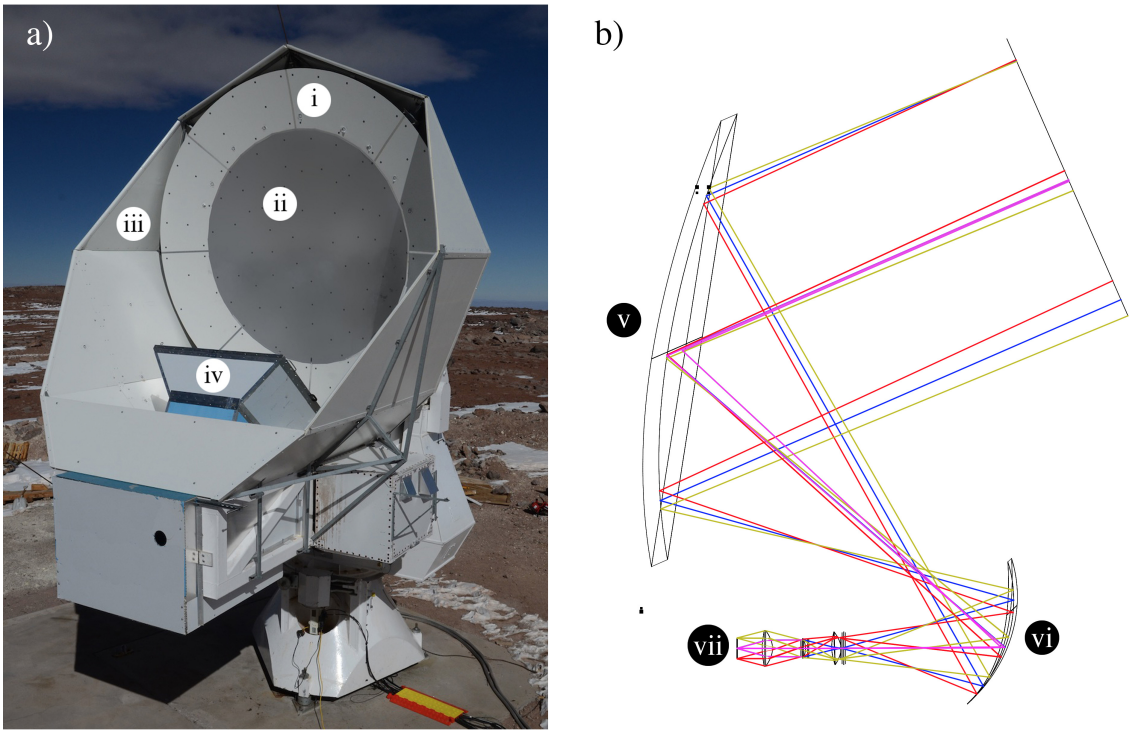

Figure 2.1: The Huan Tran Telescope. **(a)**: HTT at the James Ax Observatory in Atacama desert in Chile. In the image, (i) the primary guard ring, (ii) the primary mirror, (iii) the co-moving ground shield and (iv) the prime focus baffle. **(b)**: a ray trace schematic of the telescope optic. The focus created by (v) the primary and (vi) the secondary mirror are reimaged by cold re-imaging optics to the (vii) focal plane. Figure from [31]

with surface RMS accuracy of 53 μm. Combined with the low surface precision guard ring, the primary paraboloid can be extended out to 3.5 meter in diameter. The guard ring is designed to reduce loading toward receivers and to redirect any spillover power that does not come from the sky which can potentially caused side-lode of the non-ideal shape of the main telescope beam. The high surface accuracy mirror fabrication helps limiting loss from diffuse scattering caused by the roughness of the surface. The primary mirror provides 3.5 arcminutes FWHM beam at 148 GHz. The secondary mirror is 1.4 m monolithic cast aluminum that sits inside the baffling enclosure. The co-moving ground shield prevents potential contaminated signals from the ground and surrounding objects. This design enables the HTT telescope to observe to $\ell \approx 2500$ and to characterize the peak of lensing B-mode at $\ell \sim 1000$.

2.3.2 POLARBEAR's Cryogenic Receiver

In order to measure a weak signal from the CMB, the detector arrays need to be cooled cryogenically to reduce their thermal noise carrier to be below the background loading noises from the sky. Moreover, all the elements in the optical path can contribute to the thermal loading of the detector array. Therefore cooling these additional components besides the detector arrays in the optical path is needed. The POLARBEAR receiver is cooled down to base temperatures of 50 K and 4 K by a two stage pulse tube refrigerator (a commercial PT45 model[1]). Figure 2.2 shows a cross-sectional drawing of the POLARBEAR receiver. The main elements of the

[1]http://www.cryomech.com

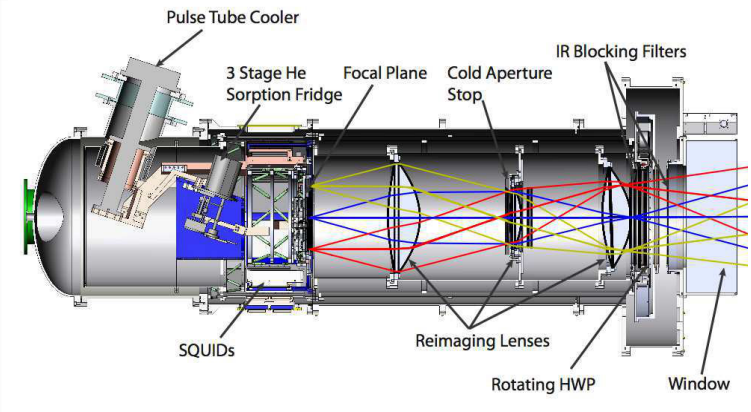

Figure 2.2: A cross-sectional drawing of POLARBEAR receiver cryostat. Ray traces overlaid the cross-sectional drawing show the optical path from the secondary mirror to the focal plane through three re-imaging lenses. The major components are identified in the image. Figure from [31]

POLARBEAR cryogenic receiver are the Zotefoam windows, IR blocking filter, half-wave plate (HWP) made from 3.1 mm thick single crystalline sapphire, and three re-imaging lenses which coupled the reflective optic from the secondary mirror to the focal plane. These re-imaging lenses are manufactured from ultra-high molecular weight polyethylene (UHMWPE) and coated with a single layer of porous polytetrafluoroethylene (PTFE). The reimaging optics give the telescope a 2.4 degrees diffraction-limited field of view for a 19 cm focal plane. The sub-Kevin focal plane is cooled by a three stages helium sorption fridge[2] provides two cooling stages at 0.35 K and 0.25 K.

[2]http://www.chasecryogenics.com

2.3.3 POLARBEAR's focal plane

The POLARBEAR focal plane consists of 637 pixels on seven hexagonal wafers, totaling of 1,274 polarized-sensitive antenna-coupled TES bolometer [36]. Each wafer is fabricated at the Berkeley Nanolab. Each pixel uses dielectric lenslet to couple the telescope's optical system. The advantages of a lenslets-coupled antenna are

- The antenna on the thick dielectric substrate such as silicon wafer, which has a relative dielectric constant ϵ_r =11.7, can suffer from a power loss due to the total internal reflection in a substrate. Lenslets can increase that total internal reflection [37].

- The antennas on the dielectric substrate tend to radiate most of their power to the dielectric substrate, creating an unidirectional pattern. The ratio of radiation power between the dielectric substrate side and air is $\epsilon_r^{3/2}$ [38].

- Since the refractive optics have a broadband spectrum and low loss in the medium. This allows for multichroic antenna to be coupled to lenslets, which extends the focal plane ability to measure multi-spectral band in a single pixel [39, 40].

The reflection loss on the surface of lenslets can be costly due to the high dielectric constant of silicon. To relieve this reflection loss, an AR coating is applied on the lenslet surface. The POLARBEAR lenslets are coated with uniform quarter-wavelength of 148 GHz thickness thermoformed polyetherimide with an optical index of 1.7.

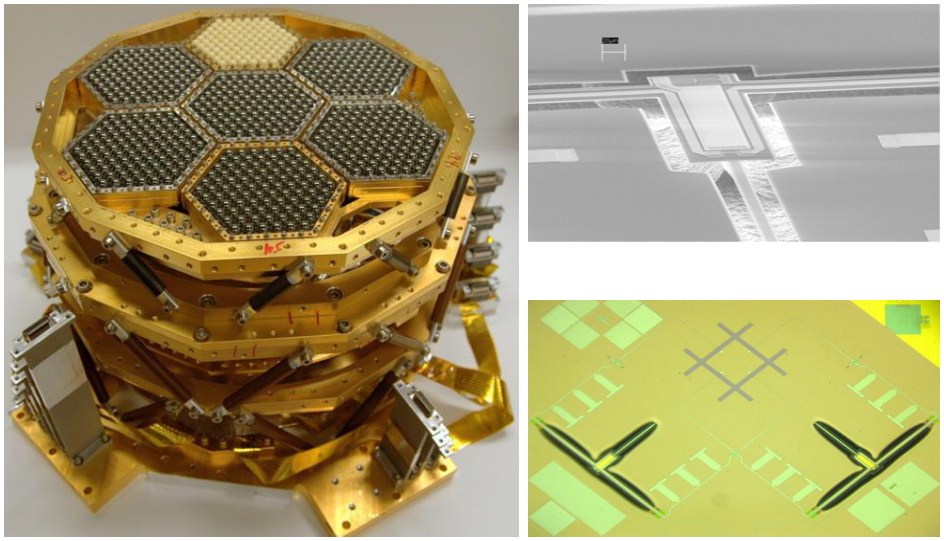

Figure 2.3: The POLARBEAR focal plane. Left: A photograph of the POLARBEAR completed focal plane tower including lenslets array and supporting structures. Top right: Scanning electron micrograph of a POLARBEAR bolometer. Bottom right: A photograph of a dual-polarized slot antenna coupled to two TES bolometers via microstrip lines.

The underside of each lenslet has a dual-polarized slot antenna oriented to be sensitive to polarizations of the incoming photon as shown in Figure 2.3. Each antenna is coupled to TES bolometer via a microstrip line. This antenna design offers us an excellent radiation pattern, a low impedance, wide bandwidth, and low cross polarization [41].

Transition Edge Sensor Bolometer

As discussed earlier, the POLARBEAR uses TES bolometer to convert an optical power to a measurable signal. As shown in Figure 2.4, a bolometer consists of a thermistor with a thermal capacity C which has a weak thermal link to a heat bath with a temperature of T_{bath} and thermal conductance G. Once a thermistor

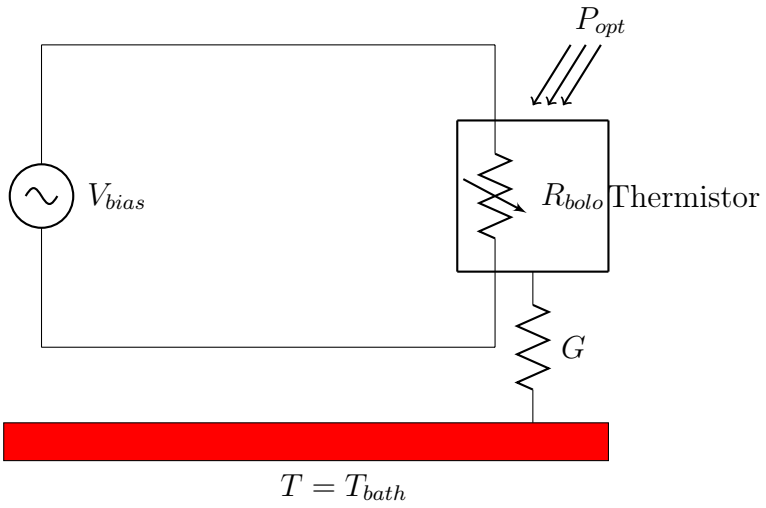

Figure 2.4: Cartoon diagram of a bolometer. P_{opt} is the power of the incident photons. The total operating power of the thermistor comes from the constant voltage V_{bias} and P_{opt}. The thermistor is connected to the wafer (red box, temperature = T_{bath}) via a weak thermal link, G.

receives the optical power P_{opt}, the temperature of the thermistor changes by ΔT if this change is slower than the time constant $\tau = C/G$. In the operation, a constant voltage bias V_{bias} is applied to the bolometer. The total operating power of the bolometer can be written as,

$$P_{tot} = P_{opt} + P_{elec} = G\Delta T. \tag{2.1}$$

The TES bolometer is designed to operate in the transition between a normal and a superconducting phase which gives an advantage of the large value of dR/dT. When the incident photon with P_{opt} increases the temperature of bolometer T and causes the resistance R to increase, the constant voltage bias will give a negative electrothermal feedback by decreasing the electric power $P_{bias} = \frac{V^2}{R}$ which will result

in $P_{tot} \approx constant$. Hence, the power of the incident photon can be obtained by measurement of the current from the bolometer which driven by the constant voltage bias. Miscalculation of the optical loading can drive the TES out of the superconducting transition and cause the bolometer power to saturate. For a ground base experiment like POLARBEAR, the expected optical loading is not only from CMB photon, but also from the atmosphere and the instrument itself.

2.3.4 Multiplexing readout

It is a challenge to have an electrical connection for all 1,274 detectors at the cryogenic focal plane to a warm electronics for a readout and give a voltage bias without creating an excessive thermal load to the sub millikelvin stage. Many CMB experiments use a multiplexing system where multiple detectors can be read out by a single pair of wires and voltage biased by another pair of wires. There are three main multiplexing systems which are commonly used among CMB experiments, time-domain multiplexing, frequency domain multiplexing and code division multiplexing. The POLARBEAR uses frequency domain multiplexing system.

In the POLARBEAR setup, each bolometer is connected in series with an LC filter which tuned to different resonant frequencies as shown in Figure 2.5. The bias resistor R_{bias} is located in 4 K stage that connects to a chain of LC-filter and bolometers by a single pair of wires to ensure only a small power is dissipated to the focal plane. The POLARBEAR uses eight multiplexing factor which means eight bolometers share a pair of readout and a pair of a voltage bias. AC voltage biases are generated at different carrier frequencies that correspond to LC-resonance frequencies

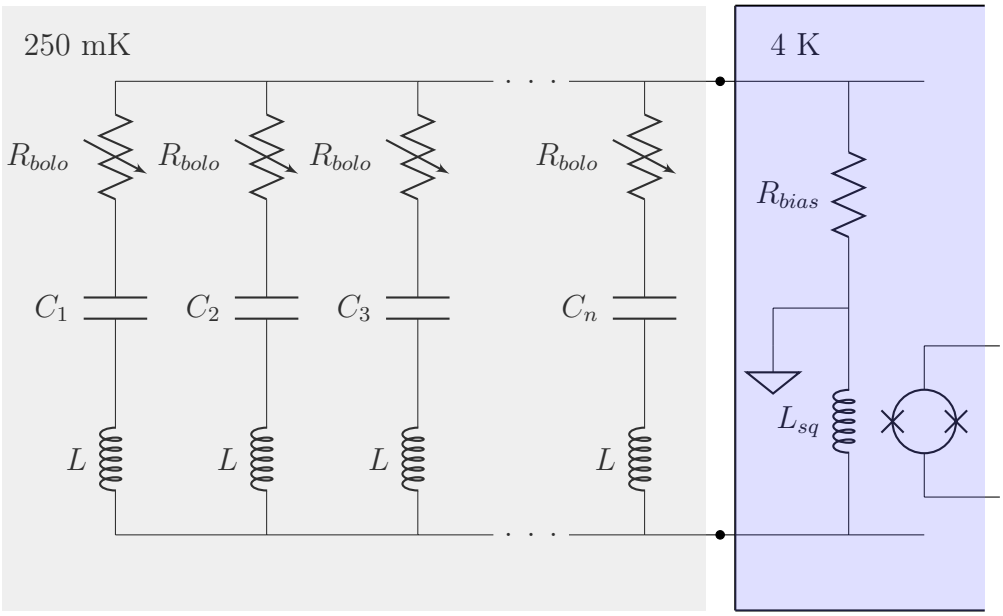

Figure 2.5: Circuit diagram of the cold portion of the frequency-domain multiplexing readout system. The box on the left shows the TES bolometers (R_{bolo}) and channel-defining LC filters. The box on the right shows the SQUID. The nominal temperature of each box is 250 mK and 4 K, respectively.

so that each bolometer will see only one voltage bias. The sum of the current from individual bolometer is measured by super-conducting quantum interference device (SQUID). The multiplexed data from bolometers goes to room temperature readout on 168 pairs of analog wires and digitized by Digital Frequency-Domain Multiplexing (DfMux) boards [42].

2.4 First and Second Season Results

The POLARBEAR collaboration published three results from the first season of observations in 2014 [35, 43, 44] and published the result from the first and second season of observations in 2017 [45]. As we discussed earlier in Section 2.2, the first and second observation season goal of the POLARBEAR is to characterize the CMB B-mode at a small angular scales on the sky, in which the dominant source is the gravitational lensing of the CMB by large-scale structure. The POLARBEAR observation strategy was designed to scan three small patches with total effective sky area of 25 $\deg^2$ with a resolution of 3.5 arcminutes. Those patches are chosen because of a low dust intensity, high observation availability throughout the day, a long distance from the Galactic plane, and overlapped observation areas to other observations for cross-correlation studies [35]. The three patches are called RA4.5, RA12 and RA23 based on their right ascension as shown in Figure 2.6. RA23 and RA12 were selected to overlap with Herschel-ATLAS observations while RA4.5 and RA23 overlaps with QUIET observations.

The first observation season began in May 2012 to June 2013 and the second

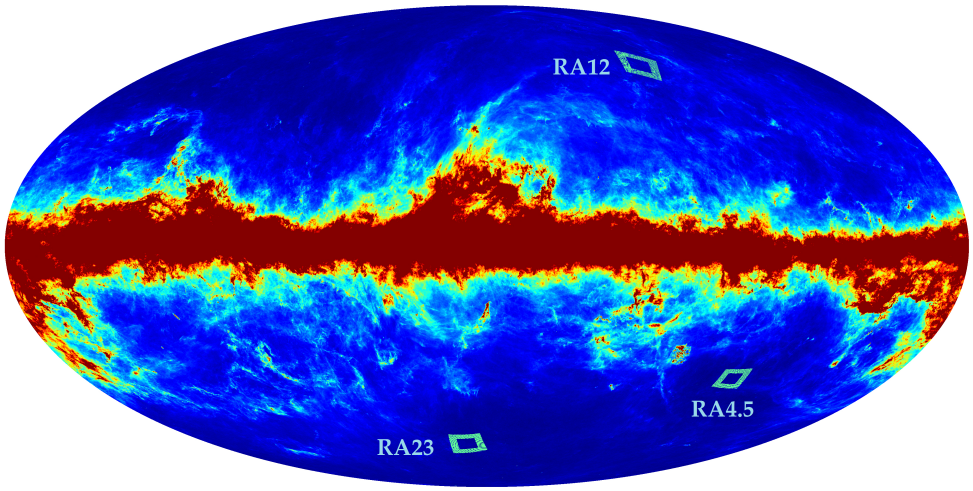

Figure 2.6: The POLARBEAR first and second season CMB patches. Three patches overlaid on the full-sky 857 GHz from Planck [46].The patches are choosen base on the low dust emission, overlap with other experiment and availability to observe throughout the day from James Ax Observatory in Chile. Figure is taken from [35]

observation season started from September 2013 to April 2014. The total observation time for the two seasons with three CMB patches was 4,700 hours.

The first result is the direct measurement of the C_ℓ^{BB} from the angular multipole range of $500 < \ell < 2100$, which is also the first direct detection of C_ℓ^{BB}. The spectrum is shown in Figure 2.9. The result rejects the null hypothesis of no gravitational lensing B-mode with 3.1σ confidence. After these data were subtracting the foreground contaminate from thermal dust, the polarized Galatic forgrounds and synchrotron using data from Planck [47, 48], then fit the band power using Planck 2015 ΛCDM parameters. We find $A_{BB} = 0.60^{+0.26}_{-0.24}(\text{stat})^{+0.00}_{-0.04}(\text{inst}) \pm 0.14(\text{forground}) \pm 0.04(\text{multi})$, where "stat" refers to the 68.3% confidence interval of the estimated quantity, "inst" refers to the systematic uncertainty from instrument,

"multi" refers to multiplicative calibration uncertainties and foreground refers to the total foreground uncertainty.

In order to prevent observer bias in data selection and analysis, the POLARBEAR analysis performed "blind", meaning no one looked at C_ℓ^{BB} power spectrum until the data selection and the analysis with systematic error tests were completed. The data were analyzed using two independent pipeline analysis and the results are in agreement. To verify all the data meet the criteria, we ran null tests in 12 divisions of data. Another important step in the analysis is ensuring the systematic uncertainties are small compared to the statistical uncertainty level that does not create a false B-mode signal. Shown in Figure 2.8, nine systematic uncertainty models were created-: i) uncertainty in instrument polarization angle, ii) uncertainty in relative pixel polarization angles, iii) uncertainty in instrument boresight pointing model, iv) differential pointing between the two detectors in a pixel, v) the drift of the gains between two consecutive thermal source calibrator measurements, vi) relative gain calibration uncertainty between the two detectors in a pixel, vii) crosstalk in the multiplexed readout, viii) differential beam size, and ix) differential beam ellipticity. We found that all nine systematic uncertainties and their combination produce a spurious B-mode signal below the statistical uncertainty level. A full description of analysis and results can be found here [45].

In addition to the result from C_ℓ^{BB} power spectrum which was discussed previously, the POLARBEAR also has two additional analyses to prove the lensing B-mode signal from the gravitational lensing. The first one was published in 2014, using the deflection power spectrum C_ℓ^{dd} which calculated using data from the first observation

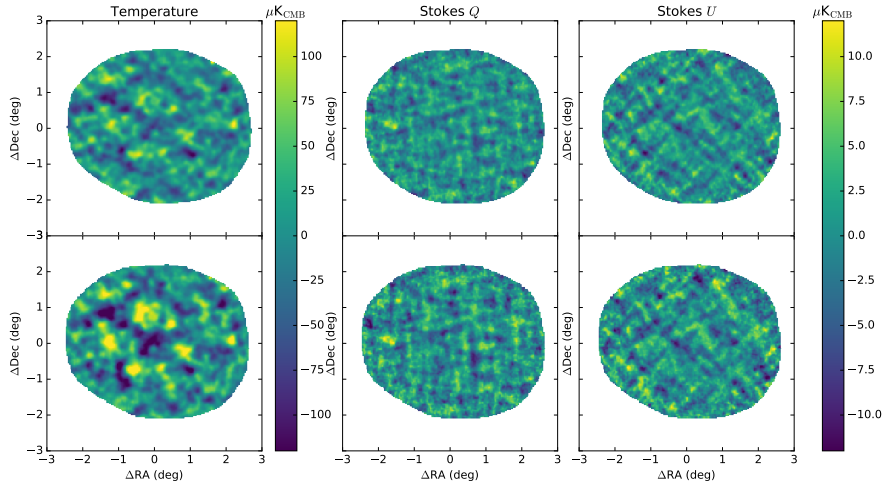

.

Figure 2.7: CMB polarization maps of RA23 in the equatorial coordinates. Left, center, right show map of intensity, Q and U respectively. Tops are generated by Pipeline A and bottoms are generated by Pipeline B. Figure is taken from [45]

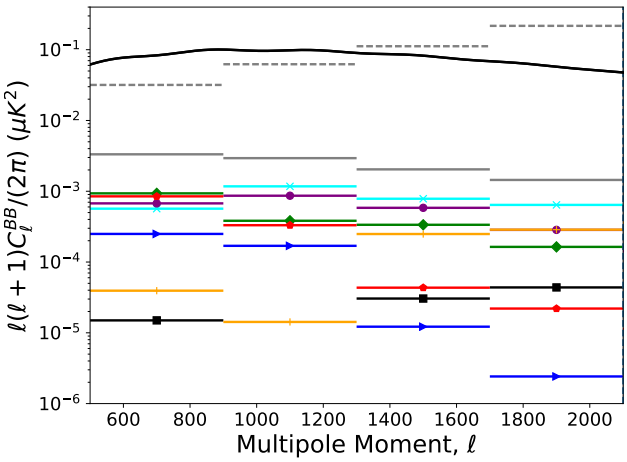

.

Figure 2.8: Systematic error simulation. The dashed horizontal lines show statistical uncertainty, the solid black lines show lensing B-mode spectrum from theoretical Planck 2015 ΛCDM, the solid horizontal grey lines show the combination of all nine systematic uncertainty effects and the rest of the solid lines show individual systematic uncertainty effects. Figure is taken from [45]

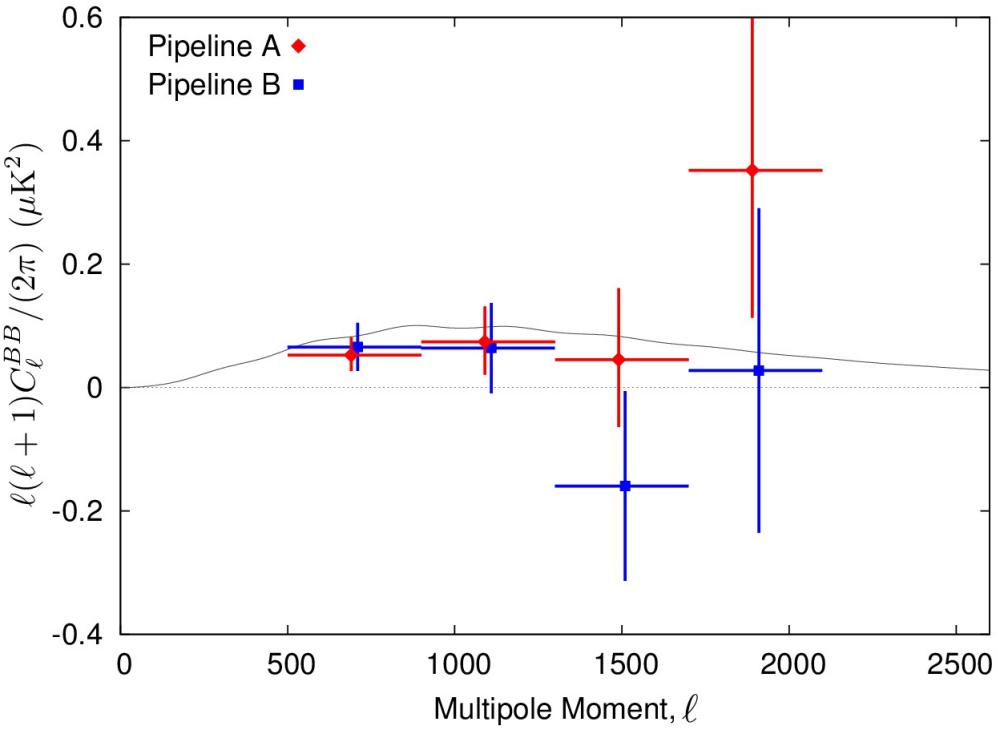

Figure 2.9: C_ℓ^{BB} power spectrum result from the two seasons. Red diamonds (blue squares) show the measure power spectrum from pipeline A (pipeline B). The solid black line shows a theoritical Planck 2015 ΛCDM lensing B-mode power spectrum. Figure is taken from [45]

season. Because CMB B-mode photons are deflected by large-scale structures and the conversion of E-mode photons, using E-mode and B-mode information and the conversion from Gaussian primary anisotropy to non-Gaussian lensed anisotropy, the maps of gravitational lensing deflection can be reconstructed. C_ℓ^{dd} was calculated using two four-point correlations estimators, $< EEEB >$ and $< EBEB >$. We found evidence of a presence of the signal of polarization lensing and lensing B-mode at 4.2σ significance. The amplitude of deflection power spectrum was measured to be $\mathcal{A} = 1.06 \pm 0.47^{+0.35}_{-0.31}$. The full analysis and further discussion can be found in [43].

The CMB also can be cross-correlated with the Cosmic Infrared Background (CIB) at a wavelength of 500 μm which also contains information about the large scale structure such as a high-redshift distribution of luminous galaxies [49]. We can use the advantage of the overlaps in observation patches with Herschel satellite to cross-correlate CMB data from the POLARBEAR and CIB maps from Herchel. The result supported the evidence of lensing B-mode at 2.3σ significance. Additional detail about the analysis and results are discussed in [44]

2.5 Acknowledgement

Figure 2.1 and 2.2 are reprints of material as it appears in: Z. D. Kermish, P. Ade, A. Anthony, K. Arnold, D. Barron, D. Boettger, J. Borrill, S. Chapman, Y. Chinone, M. A. Dobbs, J. Errard, G. Fabbian, D. Flanigan, G. Fuller, A. Ghribi, W. Grainger, N. Halverson, M. Hasegawa, K. Hattori, M. Hazumi, W. L. Holzapfel, J. Howard, P. Hyland, A. Jaffe, B. Keating, T. Kisner, A. T. Lee, M. Le Jeune, E.

Linder, M. Lungu, F. Matsuda, T. Mat- sumura, X. Meng, N. J. Miller, H. Morii, S. Moyerman, M. J. Myers, H. Nishino, H. Paar, E. Quealy, C. L. Reichardt, P. L. Richards, C. Ross, A. Shimizu, M. Shi- mon, C. Shimmin, M. Sholl, P. Siritanasak, H. Spieler, N. Stebor, B. Steinbach, R. Stompor, A. Suzuki, T. Tomaru, C. Tucker, and O. ZahnThe POLARBEAR experiment, Proc. SPIE 8452, Millimeter, Submillimeter, and Far-Infrared Detectors and Instrumentation for Astronomy VI, 84521C (September 24, 2012); doi:10.1117/12.926354. The dissertation author made essential contributions to many aspects of this work.

Figure 2.3 is reprint of material as it appears in: K. Arnold, P. A. R. Ade, A. E. Anthony, D. Barron, D. Boettger, J. Borrill, S. Chapman, Y. Chinone, M. A. Dobbs, J. Errard, G. Fabbian, D. Flanigan, G. Fuller, A. Ghribi, W. Grainger, N. Halverson, M. Hasegawa, K. Hattori, M. Hazumi, W. L. Holzapfel, J. Howard, P. Hyland, A. Jaffe, B. Keating, Z. Kermish, T. Kisner, M. Le Jeune, A. T. Lee, E. Linder, M. Lungu, F. Matsuda, T. Matsumura, N. J. Miller, X. Meng, H. Morii, S. Moyerman, M. J. Myers, H. Nishino, H. Paar, E. Quealy, C. Reichardt, P. L. Richards, C. Ross, A. Shimizu, C. Shimmin, M. Shimon, M. Sholl, P. Siritanasak, H. Speiler, N. Stebor, B. Steinbach, R. Stompor, A. Suzuki, T. Tomaru, C. Tucker, O. Zahn, The bolometric focal plane array of the POLARBEAR CMB experiment. Proc. SPIE 8452, Millimeter, Submillimeter, and Far-Infrared Detectors and Instrumentation for Astronomy VI, 84521D (September 24, 2012); doi:10.1117/12.927057.The dissertation author made essential contributions to many aspects of this work.

Figures 2.6, 2.7, 2.8 and 2.9 are reprints of material as it appears in: The POLARBEAR Collaboration: P.A.R. Ade, M. Aguilar, Y. Akiba, K. Arnold, C. Bac-

cigalupi, D. Barron, D. Beck, F. Bianchini, D. Boettger, J. Borrill, S. Chapman, Y. Chinone, K. Crowley, A. Cukierman, M. Dobbs, A. Ducout, R. DÃijnner, T. Elleflot, J. Errard, G. Fabbian, S.M. Feeney, C. Feng, T. Fujino, N. Galitzki, A. Gilbert, N. Goeckner-Wald, J. Groh, T. Hamada, G. Hall, N.W. Halverson, M. Hasegawa, M. Hazumi, C. Hill, L. Howe, Y. Inoue, G.C. Jaehnig, A.H. Jaffe, O. Jeong, D. Kaneko, N. Katayama, B. Keating, R. Keskitalo, T. Kisner, N. Krachmalnicoff, A. Kusaka, M. Le Jeune, A.T. Lee, E.M. Leitch, D. Leon, E. Linder, L. Lowry, F. Matsuda, T. Matsumura, Y. Minami, J. Montgomery, M. Navaroli, H. Nishino, H. Paar, J. Peloton, A. T. P. Pham, D. Poletti, G. Puglisi, C.L. Reichardt, P.L. Richards, C. Ross, Y. Segawa, B.D. Sherwin, M. Silva, P. Siritanasak, N. Stebor, R. Stompor, A. Suzuki, O. Tajima, S. Takakura, S. Takatori, D. Tanabe, G.P. Teply, T. Tomaru, C. Tucker, N. Whitehorn, A. Zahn, A Measurement of the Cosmic Microwave Background B-Mode Polarization Power Spectrum at Sub-Degree Scales from 2 years of POLARBEAR Data , The Astrophysical Journal, vol. 848, no.2, p.121, 2017. The dissertation author made essential contributions to many aspects of this work.

Chapter 3

POLARBEAR-2 and the Simons Array

3.1 Introduction

From the successful deployment and multi seasons of POLARBEAR experimental observations, we gained a better understanding in the instrumental development, which led to a development of the Simons Array , an expansion to the POLARBEAR experiment. The Simons Array will increase the number of detectors and the field of view of multi-frequencies measurements. The first Simons Array telescope will be deloyed with the POLARBEAR-2 receiver with detectors sensitive to 95 and 150 GHz. The duplicated receiver with same frequencies bands will be installed in the second new telescope shortly after the first one. Later in 2018, the original POLARBEAR receiver in the HTT telescope will be replaced by the third receiver which contains multichroic detectors with the spectral band of 220 GHz and 270 GHz. The Simons Array will have a total of 22,764 detectors. The combination of the multi-frequencies

range and high sensitivity detectors will allow the Simons Array to measure the CMB signal with high fidelity, leading to a better understanding of the nature of inflation. In this chapter, I will walk you through the scientific goal and the key to the improvement of the POLARBEAR-2 receiver, and current developmental status of the Simons Array .

3.2 The Simons Array's Scientific Goal

The Simons Array shares a similar scientific goal with the POLARBEAR experiment. By increasing the number of detectors and observable frequencies, the result for the Simons Array will give us a better understanding in the foreground contamination, a strong constraint on the tensor-to-scalar ratio r, the sum of the neutrino masses, and the spectral index n_s of the inflation potential.

At the elevation angle of 30 degrees from Chile, the Simons Array will be able to access to 80% of the sky. Excluding 20% of the sky due to the galactic avoidance, the Simons Array will survey of 65% of the sky. With three years of observations, the Simons Array will contribute significantly to cosmology. Figure 3.1 shows the projection of binned power spectrum from three years of observations on the theoretical C_ℓ^{BB} power spectra from ΛCDM model and the lensing signal. The sensitivity of the Simons Array allow us to measure the amplitude of the tensor-to-scalar ratio $r > 0.01$ with 5σ significance. The Simons Array will have a capability to precisely measure C_ℓ^{EE} at small angular scale which will help us to constrain the spectral index, n_s, to $\sigma(n_s) = 0.0015$ by characterizing the E-mode polarization

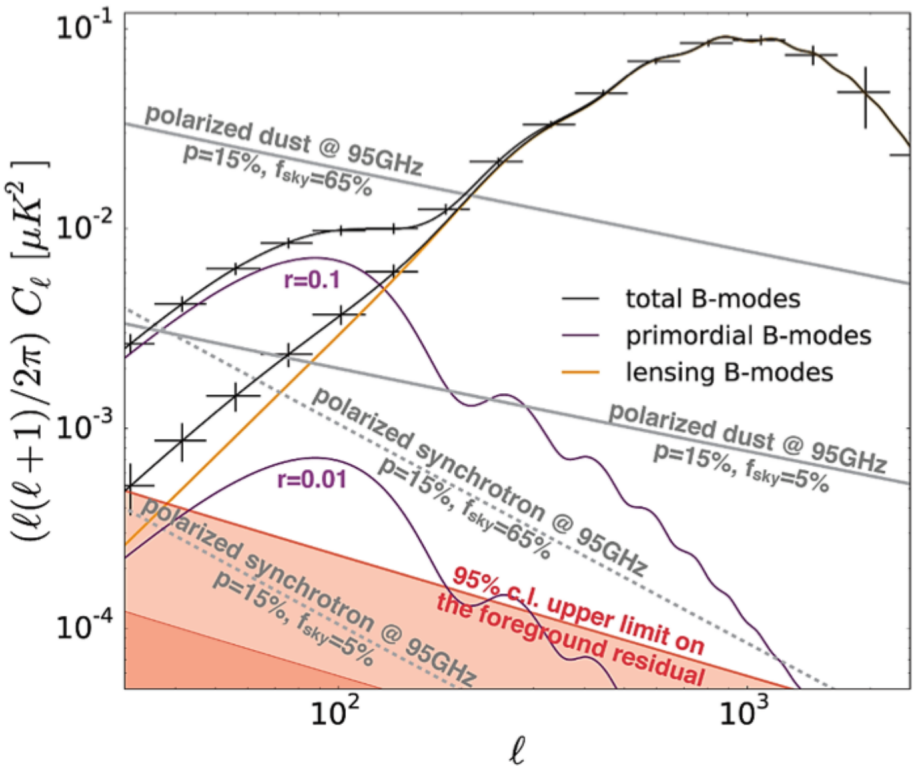

Figure 3.1: The forecasted sensitivity of the Simons Array. The theoretical B-mode CMB polarization power spectra from a ΛCDM model with tensor-to-scalar ratio $r = 0.1$ and $r = 0.001$ (purple curve) and the lensing signal (orange curve) are shown. Binned error bars from three years observation with $f_{sky} = 0.65$ are plotted. This figure is taken from [28].

power spectrum. The results from r and n_s will allow us to better understand the inflation model. The Simons Array also will also have the capability to constrain the sum of the neutrino masses by using the gravitational lensing signal to 40 meV at 1σ significant level when combining the result with DESI experiment [50].

3.3 Telescope

Using learnings from the POLARBEAR experiment, the Simons Array uses the same design as the HTT telescope - the off-axis Gregorian Dragone design with a wide diffraction-limited field of view with an angular resolution of 3.5 arcminutes at 150 GHz (more detail showed in Section 2.3.1). Most of the reflective components of the telescope are kept the same except for the co-moving shield. Two new telescopes were installed at the site in early 2016 as shown in Figure 3.2. The first POLARBEAR-2 receiver will be installed in the northern telescope. Shortly after, the second duplicated POLARBEAR-2 receiver will be installed in the southern telescope, while the third receiver will replace the current POLARBEAR receiver in the HTT telescope.

3.4 Observational Strategy

Unlike an observation from the south pole with a limited view to the sky area, the Simons Array located in Northern Chile has a sky access up to 80% of the total sky above an observation elevation angle of 30 degrees. This helps decreasing the limitation of samples variance which is very important for the search of the primodial

Figure 3.2: The Simons Array site at 5,200 meter above sea level in Northern Chile. The first POLARBEAR-2 receiver will be installed in the HTT style telescope on the left (the north telescope) in early 2018. The second one will be installed shortly after on the right of this picture (the south telescope). The third receiver will replace the POLARBEAR receiver in the HTT telescope (the middle telescope). This picture was taken in 2016.

Table 3.1: Design comparision of the POLARBEAR and the Simons Array

Specification	POLARBEAR	Simons Array
Frequencies	150 GHz	95, 150, 220 and 270 GHz
Number of pixels	637	5,691
Number of bolometers	1,274	22,764
NET_{array}	23 μK$\sqrt{s}$ (median, first season)	2.5μK$\sqrt{s}$
Field of view	2.3 degrees	4.8 degrees
Beam Size	3.5 arcmin	5.2 arcmin at 95 GHz 3.5 arcmin at 150 GHz 2.7 arcmin at 220 GHz 2.1 arcmin at 220 GHz

gravitational wave and the characterizing cosmological parameters from the CMB lensing signal. The sky in our observation site also has a number of astromonical sources which are useful for calibrations and estimation of systematic uncertainties.

Similar to the POLARBEAR experiment, the Simons Array will scan the patch on the sky by adopting a Constant Elevation Scan (CES) method using azimuth scans at stepped elevation. These patches rise and set follow the sky rotation, providing a natural sky polarization modulation.

3.5 The POLARBEAR-2 Instrument Overview

As discussed earlier in Section 3.3, the POLARBEAR-2 receiver will be housed in a new HTT-style telescope. A CAD drawing of the POLARBEAR-2 receiver and the photograph of the POLARBEAR-2 receiver are shown in Figure 3.3.

The POLARBEAR-2 receivers are designed to have a similar outlook as the single-lens reflective camera consisted of two parts: 1) an optics tube which houses

all the optical elements include three re-imaging lenses, the metal mesh filter and the alumina IR filter, and 2) a receiver backend enclosure that houses the focal plane, readout, and muli-Kelvin fridge. Each of the receiver backend enclosures and the optical tubes will have the two stages pulse tube refrigerator (a commercial PT415 model[1]) to cool down the system. Both PT415 pulse tubes are designed to be titled by 21 degrees with respect to the optical tube to have the optimum performance at the 45 degree elevation. In addition, the POLARBEAR-2 focal plane will use a three-stages helium sorption fridge to provide cooling power to the sub-Kelvin stage. The measured temperature and holding time of the focal plane are 270 mK and 28 hours, respectively [51].

In the first POLARBEAR-2 receiver, the target noise equivalent temperature (NET) of each bolometer is 360 $\mu\mathrm{K}\sqrt{s}$ for both 95 and 150 GHz. Total NET of the combined array is 4.1 $\mu\mathrm{K}\sqrt{s}$. The POLARBEAR-2 receiver will be deployed with gain calibrator and polarization modulation. For the polarization modulation, we will use a sapphire half-wave plate (HWP) at the front of the vacuum windows in the first POLARBEAR-2 receiver. For the second and third POLARBEAR-2 receiver, we will put a sapphire HWP inside the cryostat. This modulator will allow us to reduce $1/f$ noise and mitigate the beam systematics. The gain calibrator we use is the chopped non-polarized thermal source at 1000 K at the backside of the secondary mirror.

[1]http:/www.cryomech.com

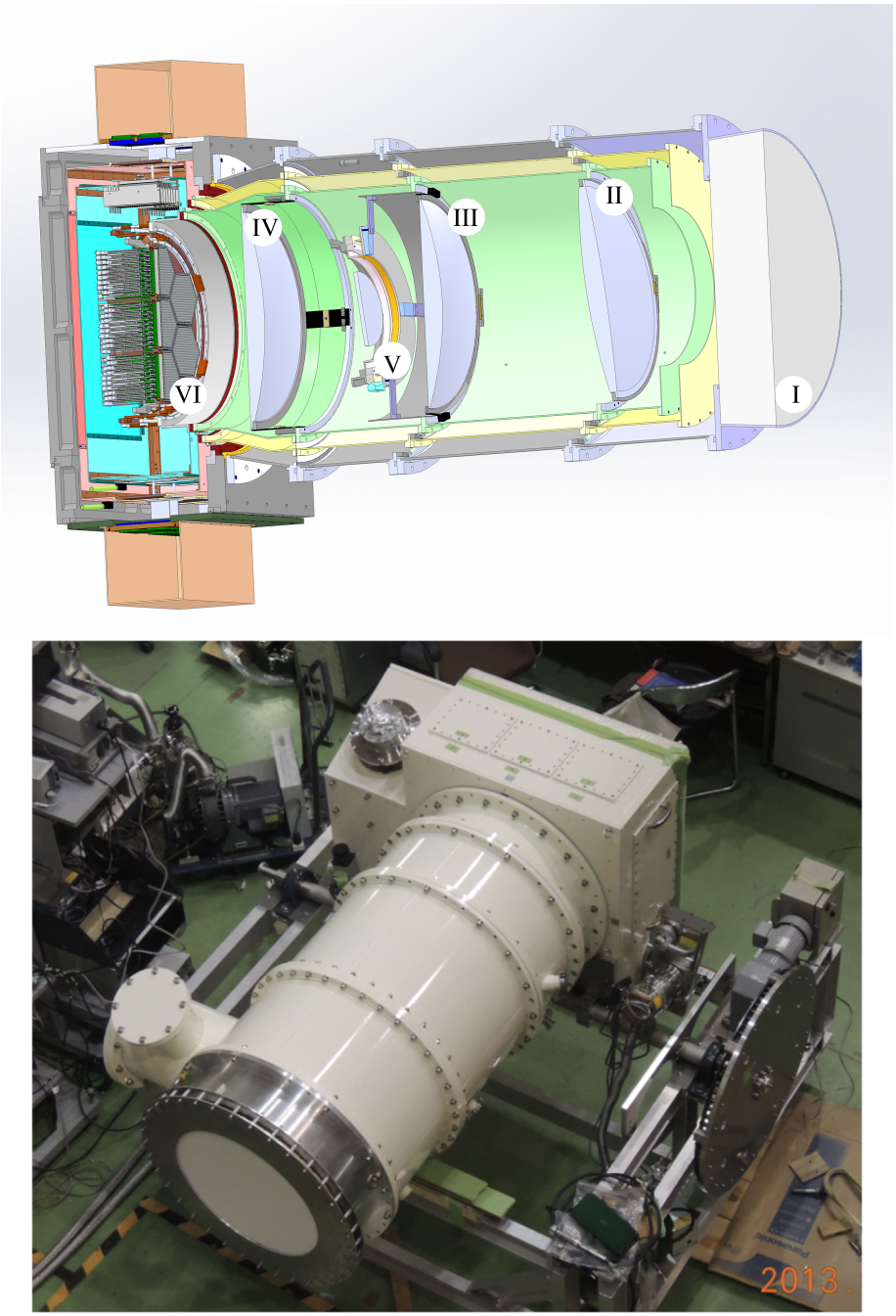

Figure 3.3: The POLARBEAR-2 receiver. **Top**; a cross-sectional drawing of POLARBEAR-2 receiver. The main components are, (I) Zotefoam Window (300K), (II) (III) and (IV) high purity alumina re-imaging lenses (4K), (V) Lyot's stop and (VI) focal plane (0.25 mK). **Bottom**; the photo of the POLARBEAR-2 receiver being tested at the The High Energy Accelerator Research Organization (KEK) lab.

3.6 The POLARBEAR-2 Optics

The POLARBEAR-2 optics consist of a combination of an off-axis Gregorian-Dragone telescope and the cold optics component inside the optics tube. The first element in the optic tube is the Zotefoam window[2] which acts as the vacuum window as shown in Figure 3.3. In the millimeter wavelength range, the refractive index of Zotefoam is close to one, which can be considered as vacuum. The diameter of the Zotefoams window and thickness is 800 mm and 200 mm, respectively. The next component is a set of IR filters at each thermal stage to reduce IR emission for the window. We use a set of the Radio-transparent Multi-Layer Insulator (RT-MLI) [52] filter at 168 K, an alumina filter at 55 K, and the metal mesh filter at the 4 K stage. Three alumina re-imaging lenses are coated with Skybond[3]+mullite on the flat surface and with epoxies: Stycast2850FT and Stycast1090 on the curved surface. The grooves are made on the epoxies side to reduce the thermal stress caused by laser cutting.

3.7 The POLARBEAR-2 Focal Plane

One of the key technologies of the Simons Array are its multichroic detectors capacity. Previously, CMB experiments were able to observe only one frequency per pixel. By expanding to the multichroic pixel, the focal plane will have double or multiple the number of the detectors per pixel. Similar to the POLARBEAR focal plane, the POLARBEAR-2 focal plane will use the lenslet-coupled antenna system

[2]http://www.zotefoams.com/

[3]Skybond is polyimide foam, made by IST corporation, http://www.istcorp.jp/en/about3.htm

which has a broadband capability..

Each POLARBEAR-2 focal plane comprises 1897 pixels packed in seven hexagonal sub-array module containing 271 pixels. The incoming CMB photons are optically coupled to the antenna in each pixel by an anti-reflection (AR) coated silicon lenslets which populated on a lenslets sub-array wafer [53]. The individual pixels in the detector sub-array wafer features the lithographed planar sinuous antennas that splits incoming photon to two orthogonal linear polarizations for each of two frequencies. The sinuous antenna is a log-periodic antenna and has a self-complementary structure which gives a stable input impedance over a broadband spectrum [54]. Photon power from the antenna is coupled to the superconducting microstrip transmission lines and feed through the on-chip band-defining stripline filter. After that, the signals are detected by superconducting TES bolometer [39, 55]. More details about testing and development of the AR-coated silicon lenslet-couple antenna system will be discussed in Chapter 4.

The first and second POLARBEAR-2 receivers in the Simons Array will both have multichroic detector arrays operating at 95 and 150 GHz while the third receiver will be operating at 220 and 270 GHz. Combining all three receivers, the Simons Array will have a total of 22,764 TES bolometers with an estimated sensitivity of 2.5 $\mu K_{cmb}\sqrt{s}$.

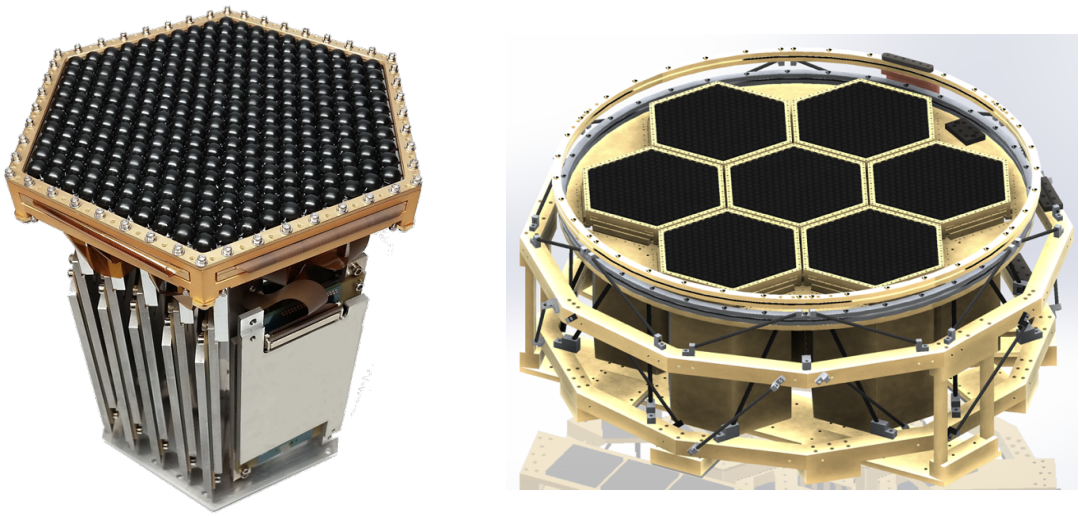

Figure 3.4: The POLARBEAR-2 focalplane. **Left**: A single hexagonal sub-array module. A single sub-array module composed of a lenslet wafer, a detector wafer and LC readout module. Each sub-array module is approximately 150 mm in diameter. **Right**: A CAD drawing of a full assembly focal plane tower consisted of all seven hexagonal sub-array modules.This figure is taken from [28].

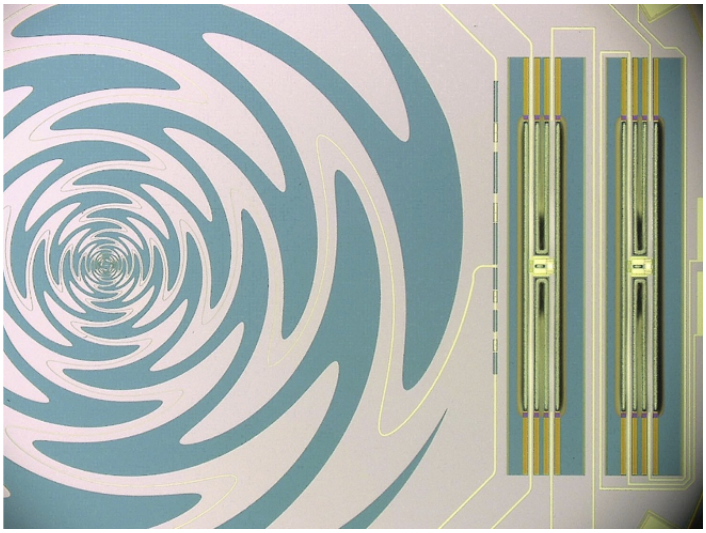

Figure 3.5: The POLARBEAR-2 detector pixel. The POLARBEAR-2 sinuous antenna feeds four TES bolometers (only two shown here) for two orthogonal linear polarizations and each of two frequencies. This figure is taken from [28].

3.8 The POLARBEAR-2 Multiplexing Readout

With 7,588 detectors in a single receiver which is six times the number of detectors in the POLARBEAR, it is impractical to readout with a multiplexing factor of 8 as the POLARBEAR due to the limitation in thermal loading from signal cables. Instead, the Simons Array uses a similar multiplexing scheme as the POLARBEAR (explained in Section 2.3.4) but increases the multiplexing factor to 40. Extending the architecture to 40 bolometers per SQUIDs requires an increase in the bandwidth of the SQUIDs electronics to more than 4 MHz [56,57]. The readout channels are defined by LC filters with 60 μH inductors and different capacitors made by NIST with the requirement of electrical crosstalk is less than 1%. The layout and frequencies spacing of LC channels are optimized to minimal crosstalk. The expected readout noise is designed to be less than 7 pA$\sqrt{Hz}$.

3.9 Current Status and Deployment Plan

The site development preparation for the Simons Array is ongoing, with two new telescopes installed in 2016. The full receiver with full seven sub-arrays assembly is under testing and characterization in the laboratory at KEK in Japan. The expected deployment date of the first POLARBEAR-2 receiver is in early 2018. The full three telescope the Simons Array is expected to be complete in 2019.

3.10 Acknowledgement

Figure 3.1, 3.4 and 3.5 are reprints of material as it appears in: N. Stebor, P. Ade, Y. Akiba, C. Aleman, K. Arnold, C. Baccigalupi, B. Barch, D. Barron, S. Beckman, A. Bender, D. Boettger, J. Borrill, S. Chapman, Y. Chinone, A. Cukierman, T. de Haan, M. Dobbs, A. Ducout, R. Dunner, T. Elleflot, J. Errard, G. Fabbian, S. Feeney, C. Feng, T. Fujino, G. Fuller, A. J. Gilbert, N. Goeckner-Wald, J. Groh, G. Hall, N. Halverson, T. Hamada, M. Hasegawa, K. Hattori, M. Hazumi, C. Hill, W. L. Holzapfel, Y. Hori, L. Howe, Y. Inoue, F. Irie, G. Jaehnig, A. Jaffe, O. Jeong, N. Katayama, J. P. Kaufman, K. Kazemzadeh, B. G. Keating, Z. Kermish, R. Keskitalo, T. Kisner, A. Kusaka, M. Le Jeune, A. T. Lee, D. Leon, E. V. Linder, L. Lowry, F. Matsuda, T. Matsumura, N. Miller, J. Montgomery, M. Navaroli, H. Nishino, H. Paar, J. Peloton, D. Poletti, G. Puglisi, C. R. Raum, G. M. Rebeiz, C. L. Reichardt, P. L. Richards, C. Ross, K. M. Rotermund, Y. Segawa, B. D. Sherwin, I. Shirley, P. Siritanasak, L. Steinmetz, R. Stompor, A. Suzuki, O. Tajima, S. Takada, S. Takatori, G. P. Teply, A. Tikhomirov, T. Tomaru, B. Westbrook, N. Whitehorn, A. Zahn, O. Zahn; The Simons Array CMB polarization experiment . Proc. SPIE 9914, Millimeter, Submillimeter, and Far-Infrared Detectors and Instrumentation for Astronomy VIII, 99141H (July 20, 2016); doi:10.1117/12.2233103. The dissertation author made essential contributions to many aspects of this work.

Chapter 4

The Multichoric Lenslet Array

4.1 Introduction

Planar antennas are widely used in CMB applications because they can be packed and integrated with planar detectors in two-dimensional arrays which do not require a lot of space. However, integrated antennas on thick dielectric substrates such as glass or silicon can experience power loss into substrate modes [37, 58]. This problem can be avoided by integrating antennas on a very thin dielectric substrate, typically less than 0.04λ [59]. In the POLARBEAR experiment, the antennas are fabricated on a dielectric substrate with thickness of less than 80 μm. This thickness range is too thin for fabricate planar antennas on silicon wafers. Another way to avoid this problem is by using a feed horn as a waveguide to the antenna. However, the feed horn has limited bandwidth. The solution that the POLARBEAR and the Simons Array use to solve these problems is by using a lenslet-couple antenna system.

Adding the dielectric lenslet on the antenna will create a unidirectional pattern into the lenslet's side. By placing a high dielectric material such as silicon on the another side of the antenna causes power to radiate more to the side which has a higher dielectric constant. The ratio of radiated power varies from $\epsilon^{1/2}$ to $\epsilon^{3/2}$ depending on the geometry of the antenna. From the POLARBEAR's dual polarized slot antenna, the ratio is $\epsilon^{3/2} : 1$ which approximates to 40:1. The other advantages of the lenslet-couple planar antenna system are the low cost of manufacture and applicability to mass production and lower losses at high frequency [60].

Nevertheless, power loss still occurs at the interface between vacuum and silicon lenslet at about 30% per surface [61]. According to the Fresnel equations, the reflections at these boundaries are highly polarized. These reflections can cause a loss in signal and create a systematic error which cause polarization leakage in a precise polarized CMB measurement. An application of anti-reflective (AR) coatings on the lenslet surface can minimize the reflection loss at the boundary surface.

In this chapter, we will start by reviewing the sinuous antenna which we use in POLARBEAR-2. Later, we will focus more on the detail of the POLARBEAR-2's lenslet array and its AR coating.

4.2 The Sinuous Antenna

Before we discuss the anti-reflection, let me briefly review the antenna design that is used in the POLARBEAR-2 and the Simons Array . Since the dual slot antenna design in the POLARBEAR has a bandwidth limitation, it is not suitable to be used

with a multichroic detector which requires broadband antennas. There are several planar antennas that are broadband such as, the bow-tie shape, the spiral antenna, the log-periodic tooth antenna and the sinuous antenna.

A sinuous antenna is a broadband log-periodic antenna which was invented and patented by DuHamel in 1987 [54]. The equation that describes sinusoidal curve of the pattern in a sinuous antenna in polar coordinate is,

$$\phi(r) = (-1)^p \alpha_p \sin\left[\pi \frac{\ln(r/R_p)}{\ln \tau_p}\right] \pm \delta_p \tag{4.1}$$

where (ϕ, r) is the polar coordiate; p is a cell number in integer (p=1,2,3,...), α_p is the angular amplitude of sinusoidal curve, R_p is inner radius of p^{th} cell, $\tau_p \geq 1$ is a logarithmic expansion factor and δ_p is angular width of each arm. A cell is a half-wavelength switchback of sinusoidal arm. And the inner radius of sinuous antenna expands as $R_{p+1} = \tau R_p$.

One drawback of a sinuous antenna is that it has polarization wobble; an oscillation of the polarization axis as a function of frequency. The sinuous antenna suffers to this effect less compares to other planar log-periodic antennas. It wobble around $\pm 5^\circ$ with $\tau = 1.4$ [40] resulting in a band-average cross-polarization leakage around 0.4% at 95 GHz and 0.5% at 150 GHz. In the POLARBEAR-2, we use a mirror image of the sinuous antenna to canceling the wobbling effects [62].

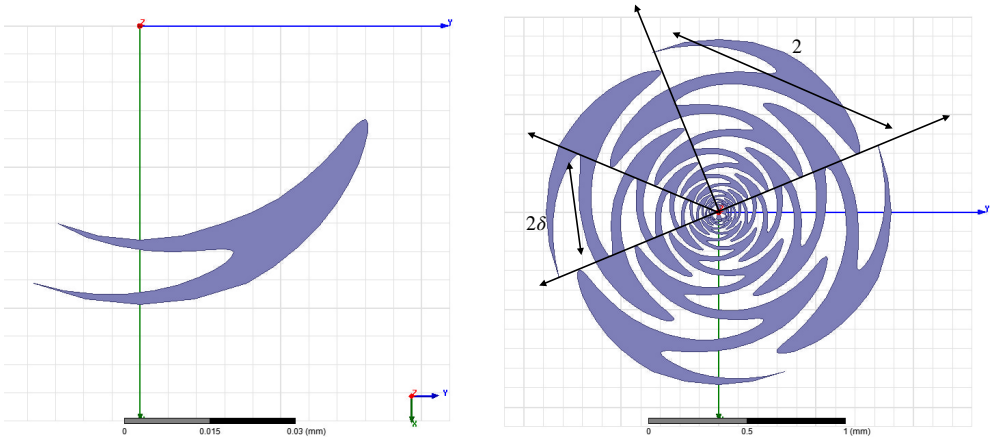

Figure 4.1: **Left**: the single cell seed structure of a sinuous antenna. **Right** A basic 4-arm sinuous antenna. This antenna has 16 cells with $\alpha = 45°$, $\delta = 22.5°$, $\tau = 1.3$ and R_1=24 μm

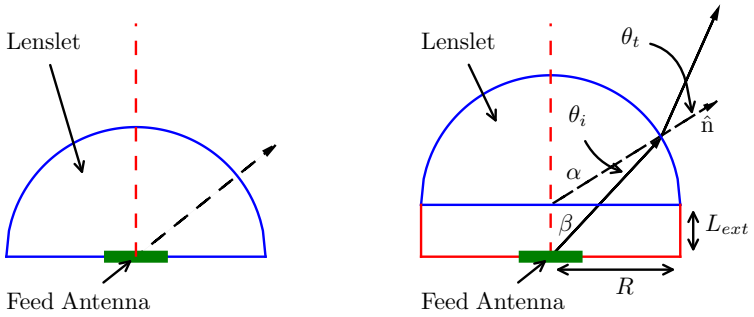

Figure 4.2: The lenslet-coupled antenna diagram. **Left**: the lenslet without the spacer. It has no focusing power to a feed antenna at its center. **Right**: from the light travels through the lenslet (blue semi-circle) and the extension length or the spacer (red rectangle) then focuses onto the feed antenna. The coating has been omitted for simplicity.

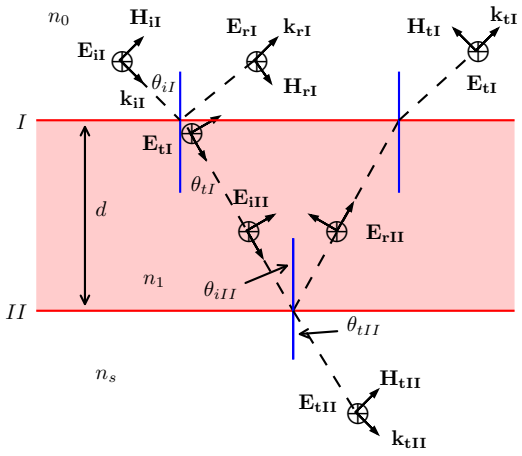

Figure 4.3: E and H field at surface boundary.

4.3 The Anti-Reflection Coatings

Anti-reflective (AR) coating can be used for eliminating unwanted reflection for the surface. To understand the theory of multilayer of AR coating, we start with the mathematic treatment of the electric field and the magnetic field of the electromagnetic wave (EM wave) at the boundary surface using the Fresnel equation.

Consider the linear polarized EM wave showed in Figure 4.3 incidents on a dielectric medium. At the boundary I, we can write the electric (**E**) and magnetic (**H**=**B**/μ) field as,

$$\begin{aligned} E_{\mathrm{I}} &= E_{i\mathrm{I}} + E_{r\mathrm{I}} = E_{t\mathrm{I}} + E_{r\mathrm{II}} \\ H_{\mathrm{I}} &= \sqrt{\frac{\epsilon_0}{\mu_0}}(E_{i\mathrm{I}} - E_{r\mathrm{I}})n_0 \cos\theta_{i\mathrm{I}} \\ &= \sqrt{\frac{\epsilon_0}{\mu_0}}(E_{i\mathrm{I}} - E_{r\mathrm{II}})n_0 \cos\theta_{i\mathrm{II}}. \end{aligned} \tag{4.2}$$

And at the boundary II,

$$\begin{aligned} E_{\mathrm{II}} &= E_{i\mathrm{II}} + E_{r\mathrm{II}} = E_{t\mathrm{II}} \\ H_{\mathrm{I}} &= \sqrt{\frac{\epsilon_0}{\mu_0}}(E_{i\mathrm{II}} - E_{r\mathrm{II}}) n_1 \cos\theta_{i\mathrm{II}} \\ &= \sqrt{\frac{\epsilon_0}{\mu_0}} E_{t\mathrm{II}} n_s \cos\theta_{t\mathrm{II}}. \end{aligned} \tag{4.3}$$

The phase of the EM wave that transverses the dielectric substrate shifts by $k_0(2n_1 d\cos\theta_{i\mathrm{II}})/2$, which will be rewritten as $k_0 h$,

$$\begin{aligned} E_{i\mathrm{II}} &= E_{tI} e^{-k_0 h} \\ E_{r\mathrm{II}} &= E_{rII} e^{+k_0 h}. \end{aligned} \tag{4.4}$$

Substituting (4.4) back to (4.2) and 4.3, we can rewrite **E** and **H** field in matrix notation as,

$$\begin{bmatrix} E_{\mathrm{I}} \\ H_{\mathrm{I}} \end{bmatrix} = \begin{bmatrix} \cos k_0 h & (i\sin k_0 h)/\Upsilon_1 \\ \Upsilon_1 i \sin k_0 h & \cos k_0 h \end{bmatrix} \begin{bmatrix} E_{\mathrm{II}} \\ H_{\mathrm{II}} \end{bmatrix} \tag{4.5}$$

or

$$\begin{bmatrix} E_{\mathrm{I}} \\ H_{\mathrm{I}} \end{bmatrix} = \mathcal{M}_{\mathrm{I}} \begin{bmatrix} E_{\mathrm{II}} \\ H_{\mathrm{II}} \end{bmatrix} \tag{4.6}$$

where

$$\Upsilon_1 \equiv \sqrt{\frac{\epsilon_0}{\mu_0}} n_1 \cos\theta_{i\mathrm{II}} \tag{4.7}$$

The characteristic matrix $\mathcal{M}$ is dependent on the boundary of the surface.

Hence in the general expression for multiple layers can be written as,

$$\begin{aligned}\begin{bmatrix} E_{\mathrm{I}} \\ H_{\mathrm{I}} \end{bmatrix} &= \mathcal{M}_{\mathrm{I}}\mathcal{M}_{\mathrm{II}}\mathcal{M}_{\mathrm{III}}\ldots\mathcal{M}_{\mathrm{p}} \begin{bmatrix} E_{(\mathrm{p}+1)} \\ H_{(\mathrm{p}+1)} \end{bmatrix} \\ &= \mathcal{M} \begin{bmatrix} E_{\mathrm{p}+1} \\ H_{\mathrm{p}+1} \end{bmatrix}\end{aligned} \tag{4.8}$$

Consider the normal incidence case,

$$\theta_{i\mathrm{I}} = \theta_{i\mathrm{II}} = \theta_{t\mathrm{II}} \equiv 0. \tag{4.9}$$

Reformulate (4.6) using (4.2) and (4.3), the reflection coefficient for a single layer can be written as,

$$r_1 = \frac{n_1(n_0 - n_s)\cos k_0 h + i(n_0 n_s - n_1^2)\sin k_0 h}{n_1(n_0 + n_s)\cos k_0 h + i(n_0 n_s + n_1^2)\sin k_0 h}. \tag{4.10}$$

Multiplying r_1 with its complex conjugate, we find the special case where the reflectance R_1 can be minimized when $k_0 h = \frac{1}{2}\pi$. In this case, the optical thickness h is equal to the odd muliple of quarter of wavelength or $d = \frac{1}{4n_1}\lambda_0$.

$$R_1 = \frac{(n_0 n_s - n_1^2)^2}{(n_0 n_s + n_1^2)^2} \tag{4.11}$$

which will equal to zero when,

$$n_1^2 = n_0 n_s. \tag{4.12}$$

Comparing to the case without the AR coating, the reflectance at the surface boundary is,

$$R = \frac{(n_s - 1)^2}{(n_s + 1)^2}. \tag{4.13}$$

In case of silicon substrate (dielectric constant, $\epsilon = 11.8$) the reflectance is about 30%. This show a crucial role that AR coating has especially when the optical elements are composed of high dielectric constant materials.

The flat geometry is good approximate at the zenith point of the lenslets where the light incident in the normal to the curved surface. With the optical path length increases as a function of the angle on the hemisphere, a thicker layer of coating is needed as we move further away from the boresight. The study by Roger O' Brient in 2010 shown that the deviation of the optimal coating thickness is varied by less than 25 μu from the nominal coating thickness in the flat geometry [63]. This deviation is close to the limit of machining tolerances. In POLARBEAR , we decided to neglect this effect in our AR coating.

4.3.1 Coating Material

Many factors need to be considered in choosing the material for AR coating for the POLARBEAR and the Simons Array . First, the coating must match the optimal index of reflection. It must also be feasible to fabricate to the right thickness and capable of being applied on curved surfaces. Second, due to the entire focal plane is needed to cool down to the sub-Kelvin stage, the AR coating must survive in cryogenic environments. Third, with the Simons Array is planned to be deployed with 1897 pixels per receiver, the material should be able to be fabricated for mass

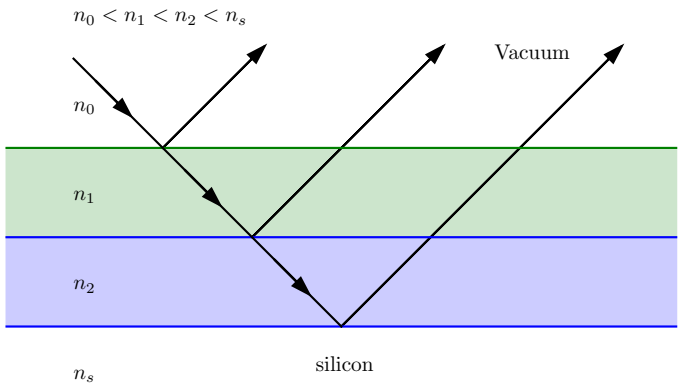

Figure 4.4: Drawing of douple-quarter coating, The reflection has been omitted for simplicity.

production in the order of kilo-pixels at an economical cost.

Thermoforming of polyetherimide (PEI) is chosen as the AR coating method for the POLARBEAR . The optical index of PEI is $n = 1.7$, measured at 1.2 Kelvin with thickness of 0.011" optimized for POLARBEAR's operating frequency of 150 GHz [64]. In the case of the POLARBEAR-2, we have to rethink the optimal fabrication process of the AR coating since the observing frequency was expanded from 150 GHz to 95 and 150 GHz. To obtain a broadband coating, two layers of dielectric materials are used. The perfect matching layers for the silicon in the POLARBEAR-2 are the dielectric constant of 2 and 5 with a quarter wavelength thickness at the center frequency of 120 GHz of 0.44 mm and 0.28 mm, respectively. The simulated transmittance from the two layers AR coating shown in Figure 4.5 is calculated from a characteristic matrix described in (4.8). The purple and the green boxes represent the observing frequencies of POLARBEAR-2.

With high curved surfaces like the lenslets and two layers coating to cover two

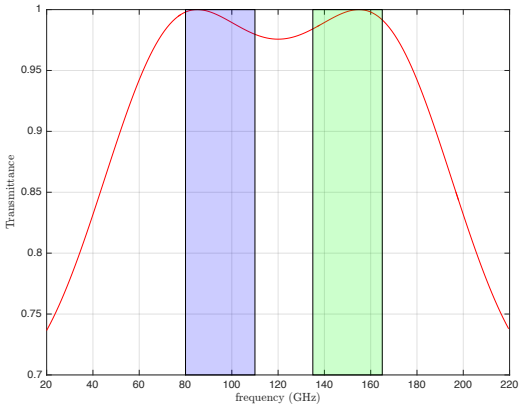

Figure 4.5: The simulated transmittance spectrum from two layers AR coating optimized for the POLARBEAR-2. The solid red line shows the transmittance spectrum. The purple box shows the expected observing band of the POLARBEAR-2 at 95 GHz. The green box is the observing band of the POLARBEAR-2 at 150 GHz

frequencies bands, casting method is used for apply the AR coating of the lenslet in our POLARBEAR-2. We found two epoxies with a dielectric constant matched specifications, Stycast1090 and Stycast2850FT[1]. In the millimeter wavelength range, Stycast1090 has a dielectric constant of 2.05 and Stycast2850FT has a dielectric constant of 4.95 [65]. With precisely machined mold, we can fabricate the proper thickness for AR-coating layers economically and at a large scale.

4.3.2 Transmission Spectrum Testing

We prepared the AR coating sample by coating it on both sides of a cylindrical 99.5% purity alumina sample which has a dielectric constant of 9.6, 51 mm in diameter, and 6.35 mm thick. We used the Michelson Fourier transform spectrometer

[1]Both epoxies are the commercial product from Henkel Corporation, One Henkel Way, Rocky Hill, CT 06067 USA.

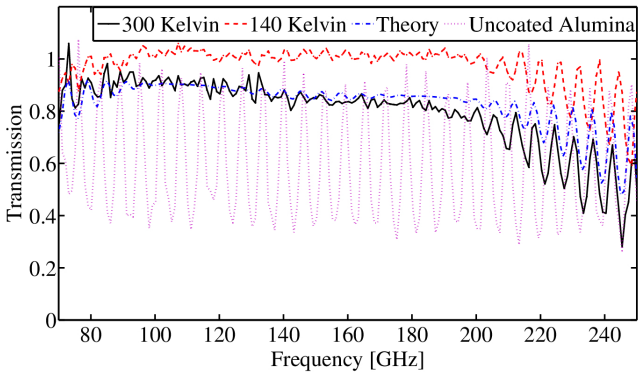

Figure 4.6: Transmittance spectrum of two-layers AR-coated alumina measured at 300 K (solid black) and at 140 K (dashed red). The theoretical curve at 300 K is shown in dash-dotted blue and measured transmittance of uncoated alumina is shown in dotted magenta. This figure is taken from [65]

(FTS) to perform the transmission spectrum test at room temperature and at 140 K. Shown in Figure 4.6 is the result from room-temperature which agrees well with the theoretical model. It also showed that the coated sample has high transmittance over a wide band compared to the uncoated sample which has high Fabry-Perot fringes due to high reflection. Moreover, the absorption loss of the cooled coated sample reduced from 15% to less than 1%. Typically the CMB experiments, includeing the POLARBEAR and the Simons Array, operate in the sub-Kelvin range.

4.4 Pixel Size

In order to retain compatibility with POLARBEAR, the pixel to pixel distance is kept same as the POLARBEAR . However, with a thicker AR coating, we have to shrink a pixel diameter from 6.35 mm to 5.345 mm. Research has shown that the minimum radius of a small lens should not exceed the wavelength in free space

(λ_0) [66]. At 95 GHz band, the lowest frequency is at 80 GHz, λ_0=3.747 mm. Compared with the POLARBEAR-2 pixel, including the AR coating, r=3.393 mm. Hence, the pixel size of the POLARBEAR-2 is at the minimum of observing at 95 GHz band.

4.5 The Extension Length

Elliptical lenses would be an ideal shape for the lenslet because of their ability to couple to the Gaussian beam with a planar wave. However, true elliptical lenses are difficult to machine in quantity. In a high dielectric constant material, the hemispherical lens with the extended spacer is a very close approximation to an elliptical lens shape [59].

The extension length plays a crucial role in the lenslet-coupled antenna system. Without the extension length, the lenslet will lose its focusing power because the incidence ray will always be perpendicular to the tangent plane of the hemisphere surface. Adding the spacer between the lenslet and antenna, will help change the angle of the ray with respect to the hemisphere boundary as shown in Figure 4.2.

The length of the spacer can affect to the coupling power of a Gaussian beam and its directivity. While research into the optimal extension length of the lenslet-coupled system was done by Edwards et al. [40], we have to re-calculate the optimal length for our experiment because the lenslets are coated with two layers of AR coating. Ray tracing analysis and ANSYS HFSS[2] simulation were used to optimize

[2]ANSYS HFSS is a commercial software for simulating 3-D full-wave EM fields, made by ANSYS, Inc.

the spacer's length.

4.5.1 Ray Tracing Analysis

The ray tracing analysis is a widely used technique for design of optical elements for microwave frequency applications [67,68]. As example of the ray tracing is shown in Figure 4.2. This method is used to optimize the spacer's length by calculating the integrated angle, the weighted average of the deviated angle of the ray from the vertical, where the weight is a Gaussian weighted with the width approximately equal to the Gaussian beam of the POLARBEAR-2. The result is shown in Figure 4.7. We found that the integrated angle is close to zero when the ratio of length of spacer to radius of lenslet (L/R) ≈ 0.46. The ray tracing for the L/R = 0.46 is shown in Figure 4.8. At the optimal length of the spacer, the optical rays from the center feed antenna are mostly parallel to the vertical.

4.5.2 HFSS Simulation

We validated the result from the ray tracing analysis with the HFSS simulation. A full model of the POLARBEAR-2 pixel was created and analyzed. Results in Figure 4.10 and 4.11, indicate that the spacer with the extension length L/R = 0.46 offered a highest directivity at 95 GHz and L/R = 0.44 at 150 GHz. These results are consistent with the result from the ray tracing method. The extension length L/R was chosen for POLARBEAR-2.

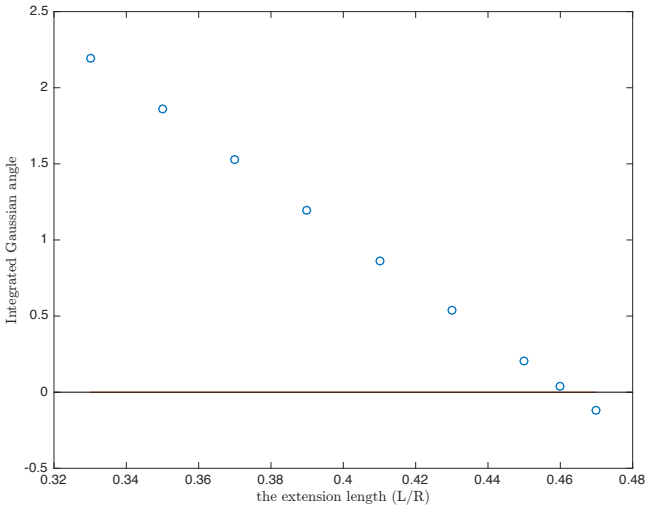

Figure 4.7: Plot of the integrated angle versus the extension length. The optimal length is around L/R=0.46 where the integrated angle is close to zero.

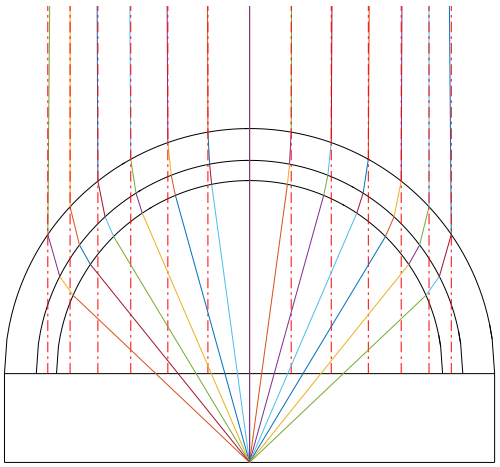

Figure 4.8: The ray tracing analysis result from the L/R = 0.46 model. Each solid line represents the ray trace from the center of the antenna. Most of the rays are parallel to the vertical line which results in the integrated angle closed to zero.

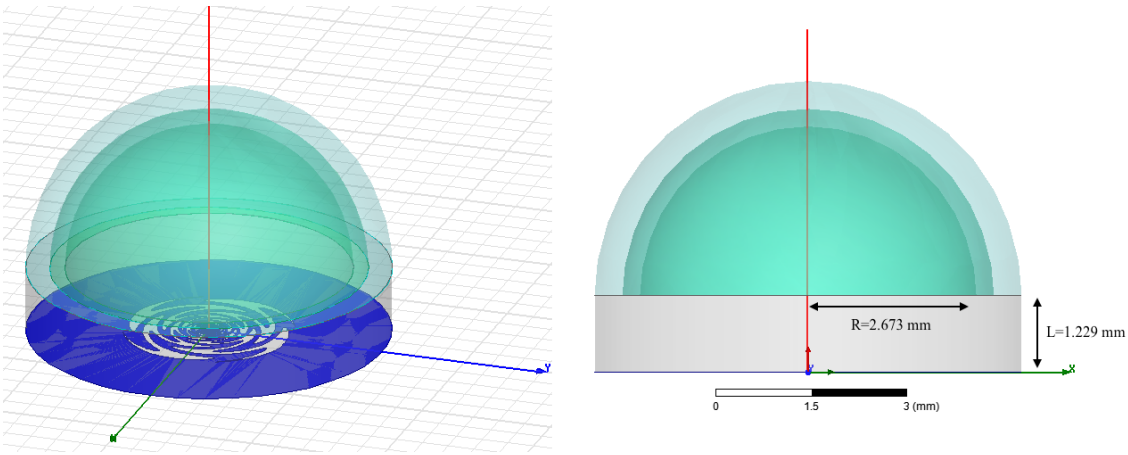

Figure 4.9: CAD drawing of HFSS simulation model. On the top, a silicon lenslet with a dielectric constant of 11.7 and diameter of 5.345 mm is coated with two layers of AR coating with a dielectric constant of two and five respectively. The cylinder extension under the lenslet represents the spacer. This simulation uses the spacer's length of 1.229 mm (L/R =0.46). The 16-cell sinuous antenna is under the spacer.

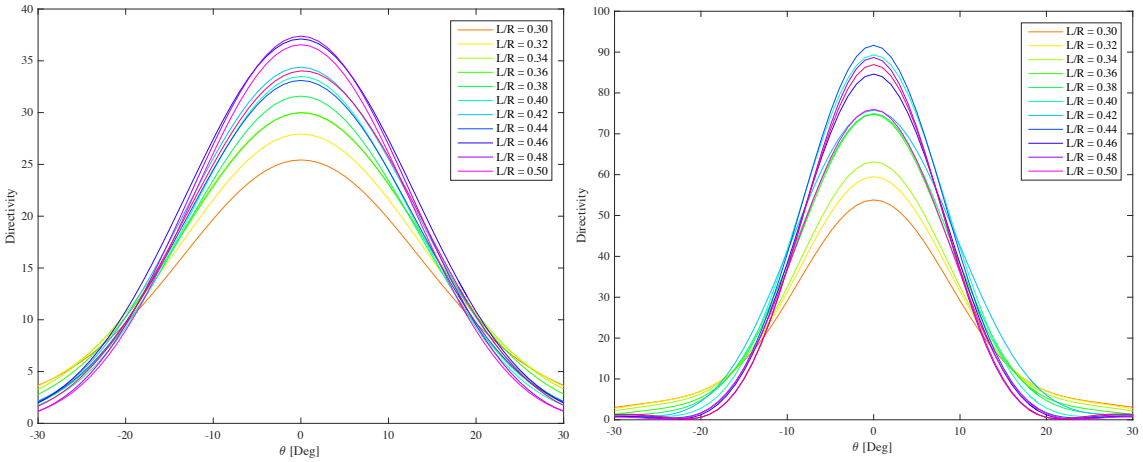

Figure 4.10: The directivity of E-plane radiation for various of L/R ratio of 95 GHz (left) and 150 GHz (right).

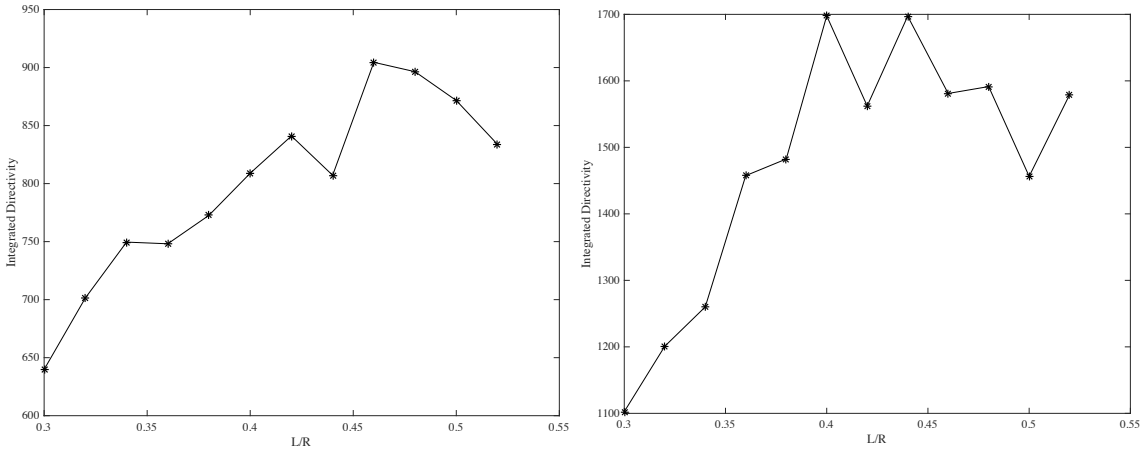

Figure 4.11: The integrated directivity plot versus L/R for 95 GHz (left) and 150 GHz (Right)

Table 4.1: Multichoric lenslet array parameters

Description	Value
Number of pixels in a wafer	271
Number of pixels in a focal plane	1,897
Lenslets's diameter	5.345 mm
The spacer's length	L/R=0.46, 1.229 mm
Pixel to pixel space	6.789 mm
The first layer coating thickness	0.279 mm
The second layer coating thickness	0.442 mm
Dielectric constant of Sytcast 2850FT	5
Dielectric constant of Sytcast 1090	2

Table 4.2: Summary of the lenslet's specification

Description	Value
Diameter	5.345 ± 0.010 mm
Height	2.673 ± 0.005 mm
Resistivity	> 1000 Ω·cm

4.6 Lenslet

The lenslets were purchased from Miyoshi Co. Ltd.[3]. The specification of the lenslet is showed in Table **??**. We randomly selected lenslets from each batch to measure their heights using a micrometer and their diameters using an optical comparator. The cylindrical silicon samples which were fabricated from the same bulk silicon with each batch of lenslets were cool down to 4 K to test the transmission spectrum using Fourier transform spectroscopy.

4.7 The Prototype Molds

One of the advantages of using epoxy-based casting method for fabricating an AR coating is that it allows us to precisely control the proper thickness of the AR-coating layers. The CNC-lathe was used to machine the prototype molds for each layer. Figure 4.12 shows one of the prototype molds that we used for fabricating AR coatings. To form a layer of thickness t_{layer} the hemispherical cavity is designed to have a radius of $R = R_{lenslet} + t_{layer}$. The lenslets sits on the seat on the cap side of the mold which is made from brass. The sleeve of the mold helps guide the

[3]http://park15.wakwak.com/ miyoshi/company.html

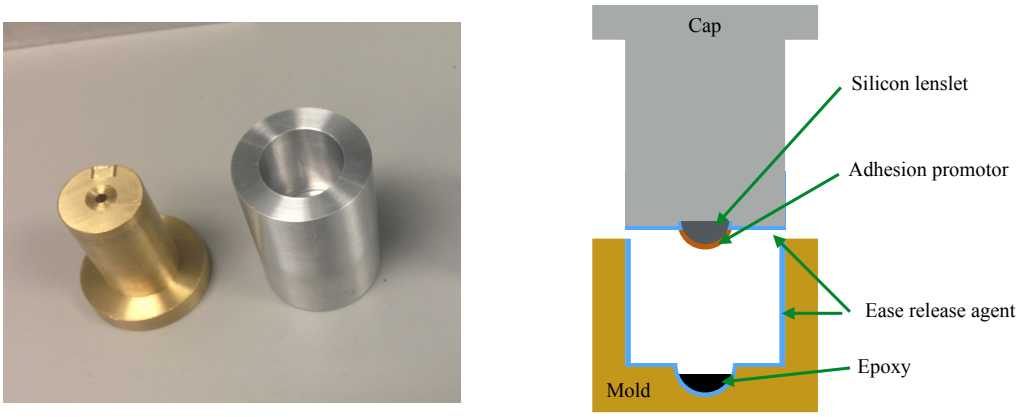

Figure 4.12: The prototype mold. **Left**: photograph of a prototype mold. **Right**: A diagram showing the operation of the prototype mold. First, the ease release agent is applied to prevent Stycast sticking to the mold. The lenslet is in the pocket in the cap and an adhesion promoter is applied. Stycast is then dispensed into the mold. Finally, the cap and the mold are assembled.

position of the lenslet to the hemisphere cavity on the aluminum mold part. Brass was used for the cap because its weight helps squeeze Stycast and keep the lenslet in the correct position. The prototype molds were made in the Campus Research Machine Shop in UC San Diego.

Inspection Process

With the casting method, any imperfection include any dent in the mold cavity will be reflected on the coating surface. As a result we have to ensure that the surface of the mold cavity is polished. Since the requirement of the tolerance of the AR coating is tight, we have to ensure the geometry of the AR coatings we produced are within the specification. Three parameters were used to determine the quality of the mold, the roughness of the coating surface, the radius of the coating and the

(A) ideal case **(B)** vertical mold offset **(C)** horizontal mold offset

Figure 4.13: A cartoon drawing of molding defects. **A**: ideal case, the coating and the lenslet are perfectly aligned. **B**: misalignment of the hemisphere and mold cavity in the vertical direction and **C** in the horizontal direction. These misalignments cause error in the layer thickness which can lead to a pointing off-set error.

alignment between the center of the coating and the center of the lenslet.

After we coated the lenslet from the prototype mold, it was inspected under the microscope. The images of the lenslets were taken at every 20 degree angles to 180 degree. We used the Matlab script to find the edge of the AR coating and fitted it to the circle. The vertical mold offset and the horizontal mold offset are evaluated from the shift of the coating's center and the lenslet's center. Figure 4.13 shows how to mold offset affect the thickness of the coated layer. Figure 4.14 shows the example photograph that we took during the mold inspection process, the thick red line shows the area where the script can detect the edge of the coating, the thin red line shows a fitted circle of the coating, the thick blue line shows the area where the script can detect the lenslet and the thin white line shows the fitted to circle of the lenslet.

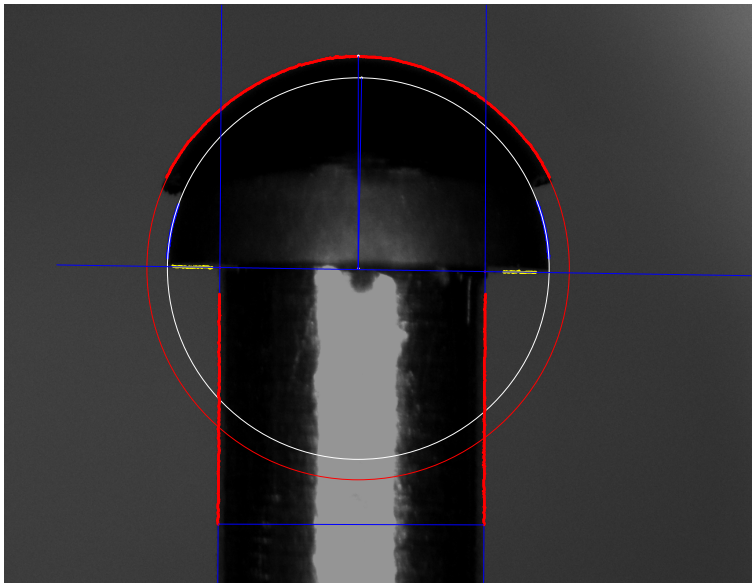

Figure 4.14: Photograph of the coated lenslet for mold inspection. The thick red line on the top of the coated lenslet shows the area that the script detect the edge of the coating in the photograph. The thin red circle line shows the fitted circle of the coating and the red dot at the center shows the center of the fitted circle. The thick blue line shows the region of the edge of the lenslet that the script detected. The white thin circle shows the fitted circle of the lenslet and the white dot at the center shows the center of the fitted circle. The thick yellow line shows the region of the lenslet's base and the blue horizontal line shows the fit of the thick yellow line to a straight line.

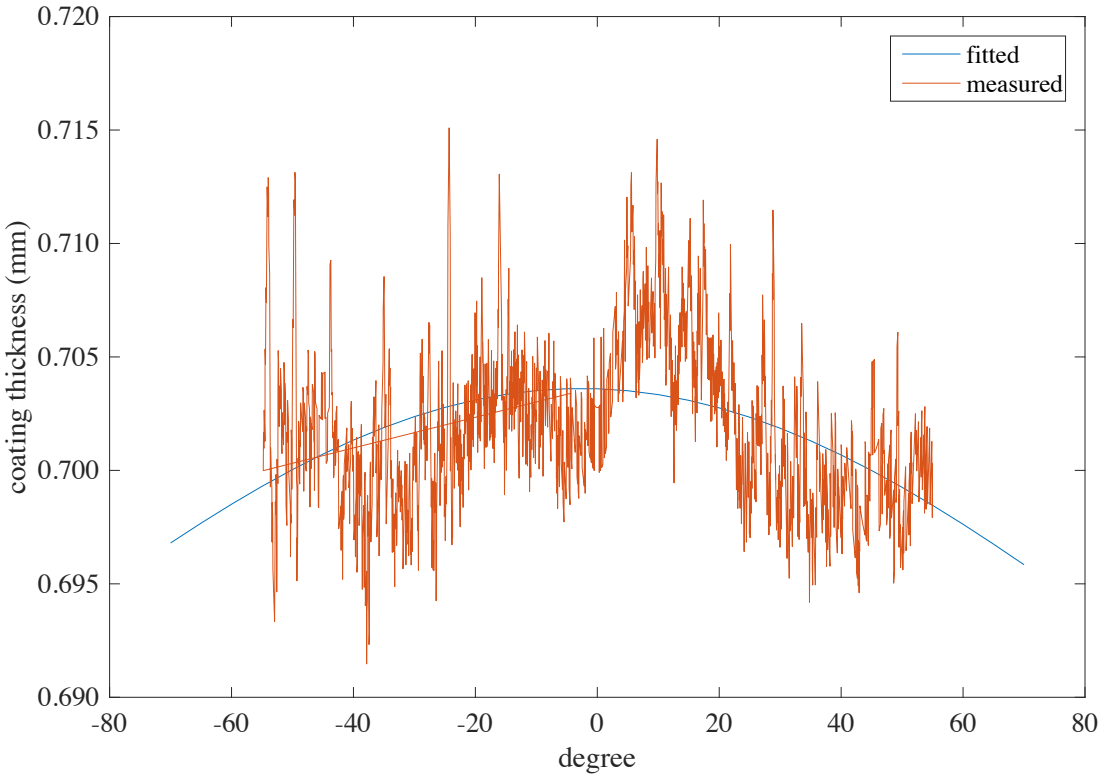

Figure 4.15: A plot of the measured coated thickness from the mold inspection process (red) compared with fitted model (blue).

4.8 Seating Wafer

The seating wafer plays two essential roles in the lenslet-coupled antenna system. First, it helps with the alignment of the lenslet and the sinuous antenna. Second, it acts as the spacer for a lenslet-coupled antenna. We designed the seating pocket to have radii oversized by 20 μm. This allows the various size lenslets to sit entirely inside the pocket seat. The tolerance of the pocket seat is less than $\lambda/100$ in free space and less than $\lambda/30$ in silicon. The systematic effect caused by the misalignment of lenslets to the center of the antenna should be minimized at this level.

Since the optimal length of a spacer is 1.229 mm and the thickness of the device wafer is 0.675 mm, the additional length requires from the seating wafer is 0.554 mm. To have a uniform spacer length, we used a silicon on insulator (SOI) wafer. The SOI wafer composed of three layers; a silicon device layer, silicon dioxide layer, and a silicon handdle layer. The thickness of each layer can be customized with high precision. We ordered 150 mm diameter SOI wafers from Ultrasil[4] with a device thickness of 555 $\pm$ 5 μm, the silicon oxide layer thickness of 2 μm and the handle wafer thickness of 120 $\pm$ 5 μm with both sides polished.

The seating wafers were fabricated in Nano3[5] facility at Calit2, UC San Diego. The photomasks used were ordered from Photo Sciences, Inc[6]. We used UV lithography to create a seating pattern on the SOI wafer. The negative photoresist was used to prevent dust in the seating pocket pattern which can cause local spot that

[4]Ultrasil Corporation, 3527 Breakwater Ave. Hayward, CA 94545 http://www.ultrasil.com/
[5]http://nano3.calit2.net
[6]https://dev.photo-sciences.com/

remain unetched in the pocket surface. These spots would create the gap between the lenslets and a seating wafer. NR5-8000 photoresist was chosen because it offers good uniformity of the film across 150 mm wafer. The photoresist is spun onto the wafer at 3000 RPM for 40 seconds, resulting in a thickness of approximately 7.5 μm. The wafers are proximity exposed in EVG620 mask aligner and developed in the resist developer RD6 for two minutes, rinsed and dried with the deionized water, then blown dry with the nitrogen gas. The wafers are then oxygen plasma etched at 250 Watts for two minutes to clean the residual photoresist from the surface of the seating pocket. We used an Advance Silicon Etch (ASE) technique to etch the silicon handle layer. ASE would allow us to do deep Silicon trench etching with highly selective ratio. The ASE process consists of alternative cycles of etching using a deep reactive ion etch (DRIE, also known as Bosch) where an RF source accelerates ion directionally the silicon surface with SF_6 and protective deposition with C_4F_8. The deposition cycle with C_4F_8 is used to protect the sidewalls from being etched by SF_6. We performed ASE process on Oxford Plasmalab 100 RIE/ICP machine. According to the manual, the selective ratio between silicon and silicon dioxide from this process is 100:1, which allows us to use a silicon dioxide layer to stop etching into the device side. To prevent over-etching, we used Dektak 150 surface profiler to do depth measurement and determined when we have to stop the dry etching process. After etching, the photoresist is removed using a photoresist removal Futurrex RR41 for five minutes. The wafer is then placed in ultrasonic bath for five minutes. After that, we removed the silicon dioxide using a wet etch process. The wet etchant used in this process is the buffered oxide etch (BOE) which comprises a 6:1 volume ratio

of 40% ammonium fluoride (NH4F) to 49% hydrofluoric acid (HF) in water. Since the wet etch process is an isotropic process, the etching rate and time are crucial to prevent over-etching. The color of the oxide layer can be used to estimate the thickness of the oxide layer. We use this color to determine the etch time. To verify the cleanliness of the wafer, the wet test is used. Since an silion dioxide is hydrophilic and a silicon is hydrophobic, the water drop test can be use to verify the cleanliness of the wafer. The detail of the fabrication process flow is shown in table 4.3.

The inspection of the seating wafer was performed using the Phillips XL30 ESEM Scanning Electron Microscope (SEM). We checked the sidewall profile and the gap between lenslet and pocket floor. The gap underneath the lenslet can create an optical cavity and cause tilted lenslets which lead to an elliptical beam shape. This process gave us feedback to modify the dry etching recipe to adjust the seating pocket profile. The micrographs of the seating wafer in Figure 4.17 shows that the gap underneath lenslet is less than 5 μm.

We used Toho Technology FLX-2320 Thin Film Stress Measurement System to determine the curvature change in the wafer after etching and after populated lenslets (we will discuss populated lenslets process later in Section 4.11). The average curvature of the seating wafer is less than 10 μm.

4.9 Simulation

A POLARBEAR-2 lenslet-coupled to a sinuous antenna was modeled and simulated in HFSS. In this analysis, we used a spacer with the length of L/R=0.46 as

Table 4.3: Fabrication process

	Process Description	Material/Equipment	Recipe/Parameters
1	Wafer parameters	150 mm SOI <100>	P-Type Handle Thickness 120 ± 1 μm Device thickness 555 ± 5 μm
2	Photoresist Spin Coating	Spinner-3	Spin Futurrex NR5-8000 3000 rpm: 40 s film thickness ≈ 7500 nm Soft bake: 150° C, 1min
3	Photolithography	Mask Aligner EVG-620	Manual Flood mode, Hard contact for 12 s Post bake: 100° C Develop in RD-6 2 mins
4	O2 plasma descum	Plasma Etch PE100	O2 Plasma 250 W 5 sccm for 2 mins
5	Silicon Etch	Oxford P-100	B2 Process, requires pre-condition the chamber Helium backing level 4.5 passivation time 5 s cycles depending on the machine condition, normally ≈ 230 cycles
6	Depth Verification	Dektak 150	the expected depth ≈ 120 μm
7	PR removal	Solvent/wet station	Futurrex RR41 for 5 mins and acetone in ultrasonic bath for 5 mins
8	O2 plasma descum	Plasma Etch PE100	O2 Plasma 250 W 5 sccm for 2 mins
9	Silicon oxide removal	Acid/ wet station	BOE solution for ≈ 20 mins
10	Bow measurement	Toho Technology FLX-2320	
11	Dicing wafer	Disco Automatic Dicing Saw 3220	
12	Sidewall inspection	SEM FEI Quata FEG 250	Inspect the sidewall of the seating pocket

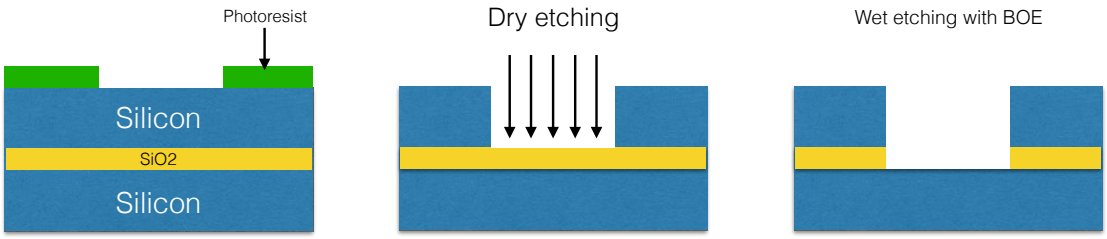

Figure 4.16: A cross-section of seating wafer fabrication process. **Left**: the photoresist mask on the SOI wafer. **Middle**: the dry etching process. The etching process stops when the etching trench reaches the silicon dioxide layer. **Right**: the wet etches process with BOE solution to clean up the silicon dioxide layer.

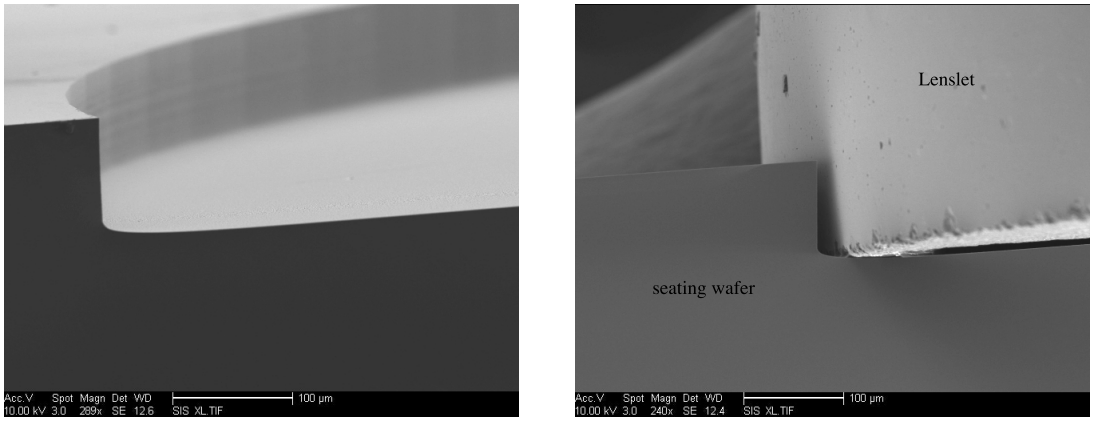

Figure 4.17: SEM Micrographs of the seating wafer. **Left**: shows the micrograph of the seating pocket. Right: shows the micrograph of lenslet sits inside the seating pocket, labels are shown in the figure. The gap between lenslet and the pocket surface is less than 5 μm.

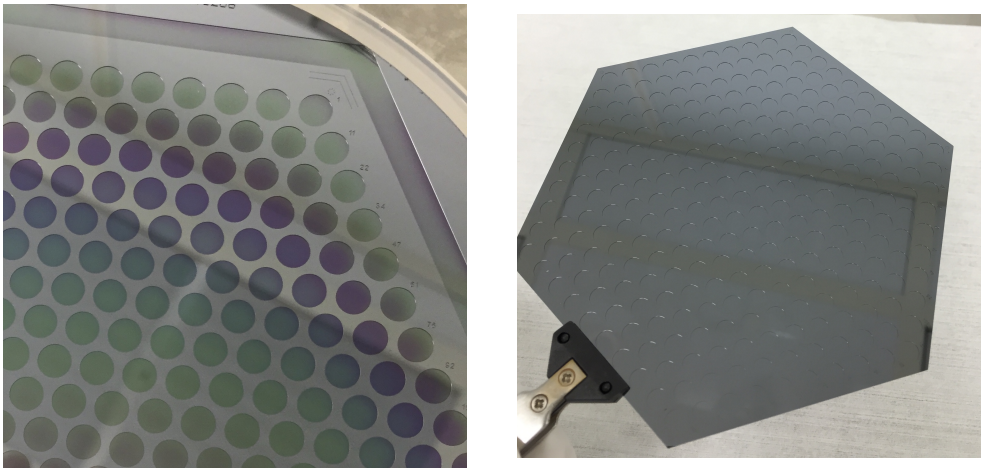

Figure 4.18: A seating wafer photograph. **Left**: A seating wafer before the oxide layer is removed. **Right**: A finished seating wafer.

mentioned earlier. The lenslet was not fully coated with AR-coating all the way down to the spacer as the previous simulation because of our mold design. The 1 mm gap between an AR coating and the spacer was created. We ran the HFSS simulation with a frequency sweep from 70 GHz to 120 GHz with 2 GHz spacing for the 95 GHz band and from 120 GHz to 170 GHz with 2 GHz spacing for the 150 GHz band. The beam profiles from each frequency were integrated using design POLARBEAR-2 frequency bands.

The polarization wobble effect is shown in Figure 4.20. This result is agreed well with a previous study from Edwards et al. [40]. We also studied the cross-polarization and co-polarization radiation pattern from the POLARBEAR-2 detector. The third Ludwig definition was used to defined cross-polarization [69]. The radiation patterns are shown in Figure 4.19.

To calculate the ellipticity, we fitted the integrated beam to 2D Gaussian

functions,

$$f(x,y) = A\exp\left(-\left(\frac{(x-x_0)^2}{2\sigma_x^2} + \frac{(y-y_0)^2}{2\sigma_y^2}\right)\right) \tag{4.14}$$

using a least-squares nonlinear curve-fitting method and the beam ellipticity from elliptical parameters. The beam ellipticity is defined as,

$$\epsilon = \frac{a-b}{a+b} \tag{4.15}$$

where a and b are the major axes and minor axes of the ellipse. We found that the individual beam profile for each frequency shows a high ellipticity and its major axis wobbles depending on the frequency. Once we averaged the beam across the frequency band, this effect is canceling out. The beam size is calculated from the full width at half maximum (FWHM) using the relationship between FWHM and σ as,

$$\mathrm{FWHM} = 2\sqrt{2\ln 2}\sigma. \tag{4.16}$$

4.10 Testing

We tested a prototype of PB-2 detector with AR coating lens in an IR Lab cryostat. For infrared filters, we used two layers of 0.3175 cm thickness expanded Teflon and a metal mesh low pass filter with 18 cm^{-1} cut-off mounted to the 77 K shield. Two metal mesh low pass filters with cutoffs at 14 cm^{-1} and 12 cm^{-1} were mounted to the 4 K shield. We placed 14 two-layer AR coated lenslet on the seating wafer. Then we used an invar clip to attach the detector wafer to the back side of the

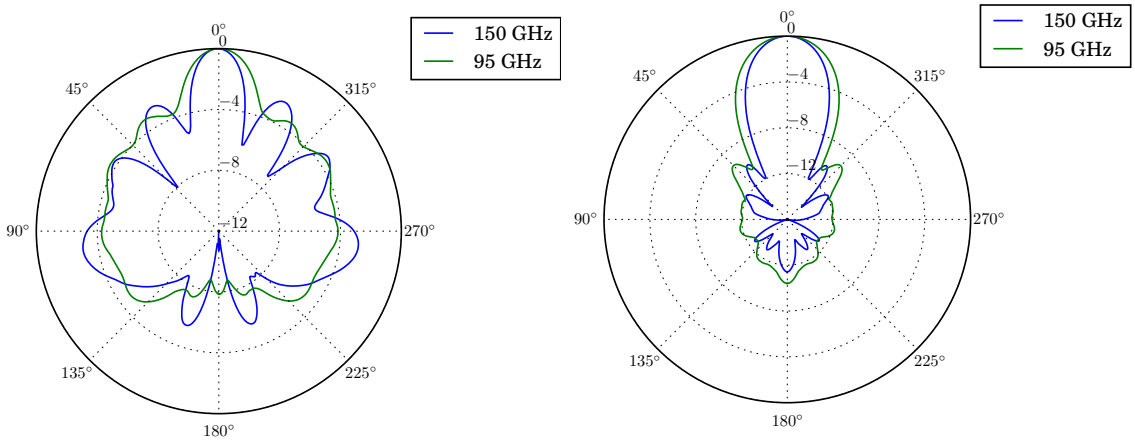

Figure 4.19: The electric field radiation pattern from 95 GHz and 150 GHz bands. **Left**: the cross-polarization pattern from 95 GHz band (green) and 150 GHz band (blue).**Right**: the co-polarization pattern from 95 GHz band (green) and 150 GHz band (blue). All units are in dB. We used Ludwig's third definition to define co-polarization and cross-polarization [69].

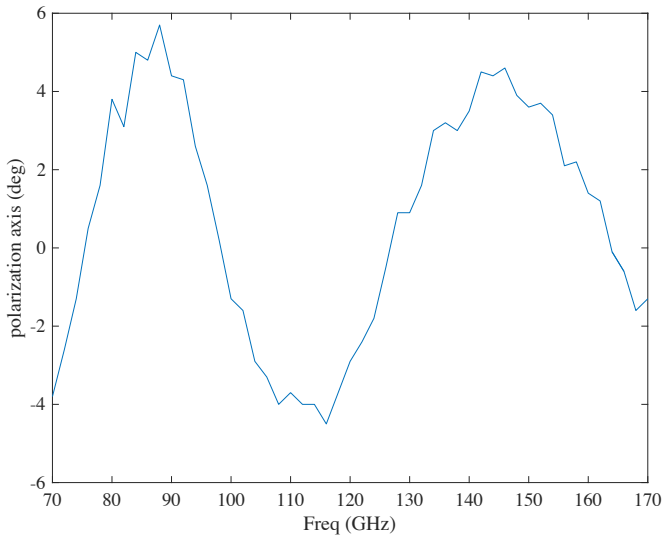

Figure 4.20: The polarization wobble effect simulation for the POLARBEAR-2 detector.

seating wafer. The detector wafer was cooled to 4 K using liquid Helium then cooled to 0.8 K using a ^{3}He absorption fridge. Commercial DC SQUIDs from Quantum Design Inc.[7] were used to read-out the output current from the bolometer. The photograph of the miliKelvin stage setup in IR lab dewar is shown in Figure 4.21.

4.10.1 Test Setup

We conducted a series of tests to characterize the performance of the AR coating lenslets with the POLARBEAR-2 sinuous antenna. To ensure that the coated lenslet perform as expected from the simulation and that it will survive through the cryogenic environment. Four tests were conducted; The Fourier transform spectrometer test, the beam map test, the polarization test and the efficiency test.

Fourier Transform Spectrometer (FTS)

The FTS test was performed to ensure that the AR coating does not degrade the frequency bands. The FTS used was the Michelson interferometer with chopped temperatures between 800 K and 300 K Eccosorb. The thermal source used was a MS-1000 micro ceramic heater from Sakaguchi Dennetsu. The beam splitter was a 0.010 inch sheet of mylar. We used the POLARBEAR UHMWPE collimating lens to focus the output from the FTS.

[7] https://www.qdusa.com/

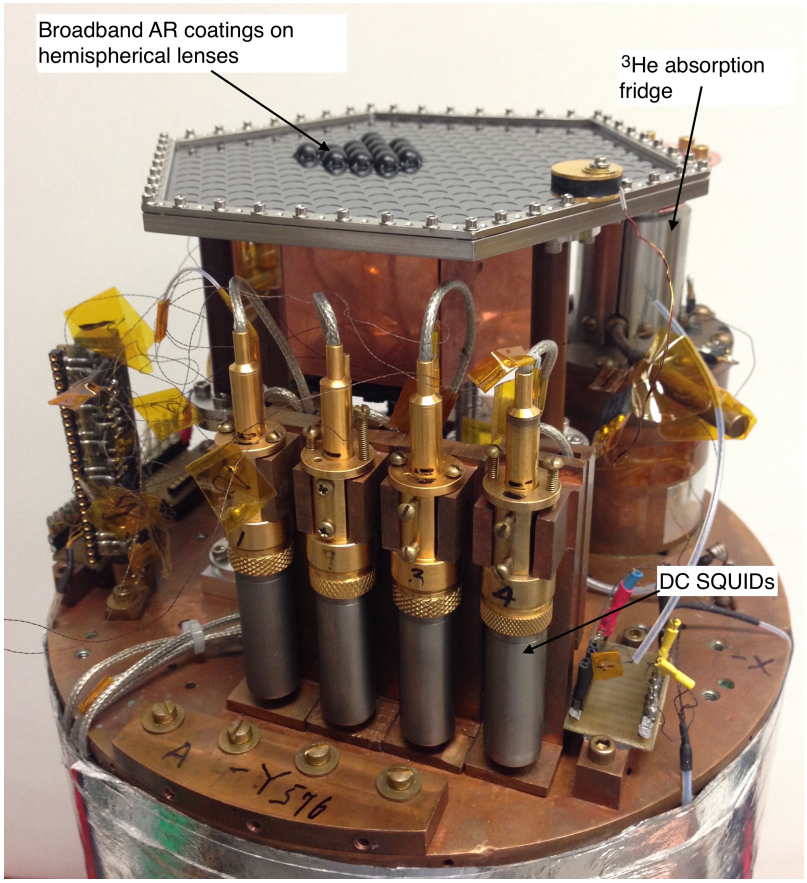

Figure 4.21: A photograph of the miliKelvin stage setup in IR lab dewar used for testing. We used 14 AR coated lenslets on the seating wafer. The copper can with Eccsorb was placed inside on the backside of the detector to terminate the backside lobe. The ^{3}He fridge on the left of the dewar was connected directly to wafer holder clip. The DC SQUID from Quantum Design Inc on front side of the dewar was used for readout of the current from TES bolometers.

Beam Mapping

The beam maps were produced by raster scanning 6.35 by 6.35 cm. with a step size of 0.3175 cm with a 1.27 cm diameter. The thermal source is modulated between room temperature Eccosorb[8] and source's temperature. The modulated thermal source is placed 25 cm away from the detector. The thermal sources that we used were a MS-1000 micro ceremic heater, liquid nitrogen and the 90 mm^2 T-SHTS/4 ceramic heater source from Elstein-Werk M. Steinmetz GmbH & Co[9].

Polarization

The wire grid polarizer was placed above the beam mapper discussed in Section 4.10.1. The wire grid was made of Tungsten wire with a diameter of 25 μm and had a spacing between wires of 100 μm. A stepper motor was used to increment the rotation angle of the wire grid.

Efficiency

The beam filling method was used to measure the efficiency of the detector. We filled the antenna beam with liquid nitrogen soaked-Eccosorb and room temperature Eccosorb then calculated the power that the detector receiver from liquid nitrogen and room temperature. In the ideal case for single mode antenna detector, the power difference from two different temperature sources is $k_B \Delta T \Delta \nu$ where k_B is Boltzmann constant, ΔT is the temperature difference between two sources which is 223 K. $\Delta \nu$ is the fractional bandwidth which was calculated from the intergrated

[8]http://www.eccosorb.com/
[9]http://www.elstein.com/

bandwidth of the peak normalized spectrum measured with the FTS. The efficiency of the detector includes a loss from dewar is,

$$\eta = \frac{\Delta P_{optical}}{k_B \Delta T \Delta \nu}. \tag{4.17}$$

4.10.2 Results

The results of the measurement shown here was from the prototype of the POLARBEAR-2 detector made with the IR-Lab cryostat. Improvements need to be made before the deployment of POLARBEAR-2.

Fourier Transform Spectrometer

These interferograms were apodized with a triangle window function before the Fourier transform. The spectra were then divided by the analytical beam splitter function to remove the effect from the beam splitter and normalized to calculate the fractional bandwidth ($\Delta\nu$) for the efficiency measurement. The result was shown in Figure 4.22 plots with the atmospheric window at PWV=1mm and an elevation of 60 degrees. This shows that the center of band frequencies are within our target and the AR coating do not degrade the performance of the detector.

Beam Map

First the beammapper was raster scanned with the ceramic heater source. During this test we found an irregular feature in the beam profile of the 95 GHz pixel that was caused from the non-uniform distribution of temperature in the MS-

1000 micro ceremic heater source. We solved the problem by using the liquid nitrogen as the thermal source. The beam map results are shown in Figure 4.23. The results were compared with simulation results as mentioned previously in Section 4.9. The beam maps were fitted to a 2D Gaussian function as same as the method that we used in the simulation result. The full width at half maximum of the measured beam maps agrees with HFSS simulations to within 7%. The ellipticities were calculated from

$$\epsilon = \frac{|\sigma_a - \sigma_b|}{\sigma_a + \sigma_b} \tag{4.18}$$

and are 2.07% at 95 GHz and 1.93% at 150 GHz.

Polarization Measurement

The polarization results are shown in Figure 4.24 and 4.25. All data were fitted to sine functions then the cross-pol and co-pol level were calculated. The results of cross-pol are shown in Table 4.4. From this test, the cross-pol level of 150 GHz pixel is around 2% of which 1% was contributed by the reflection of the wire grid and another 1% is from the polarization wobble discussed in Section 4.2. In the 95 GHz pixel, an unusual high cross-pol level was found around 5%. Later optical testing of a 95 GHz dark bolometer which is the bolometer that is not connected to an antenna were conducted. The response from the dark bolometer was found. This is the evidence that we can direct stimulate 95 GHz bolometer which can contribute to the high cross-pol level that we saw during the polarization testing.

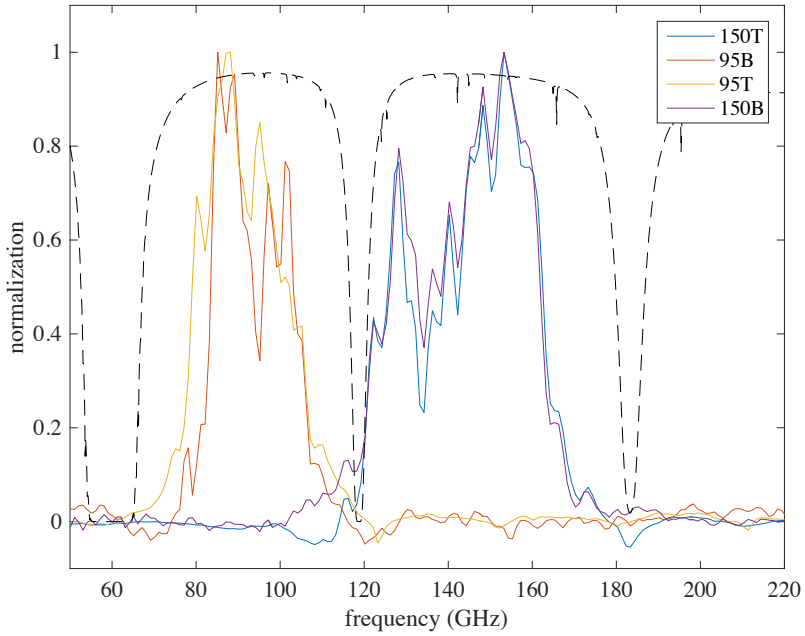

Figure 4.22: The spectra from 95 GHz and 150 GHz pixels, T and B denote theTop and Bottom bolometer. The dashed black line is the atmospheric windows from PWV=1mm and an elevation of 60 degree. This shows that the AR coating did not degrade the performance of the POLARBEAR-2 detector.

Efficiency Testing

The fractional bandwidth from FTS measurement was calculated. For 95GHz $\Delta\nu = 2.2 \times 10^{10}$ GHz and 150 GHz is 2.81×10^{10} GHz. The different optical power of the detectors from two different thermal sources are 24.11 pW for 95 GHz pixel and 28.55 pW for 150 GHz. The efficiency of the detector including loss from the cryostat calculated from (4.17), are 35.6% for 95 GHz and 33% for 150 GHz.

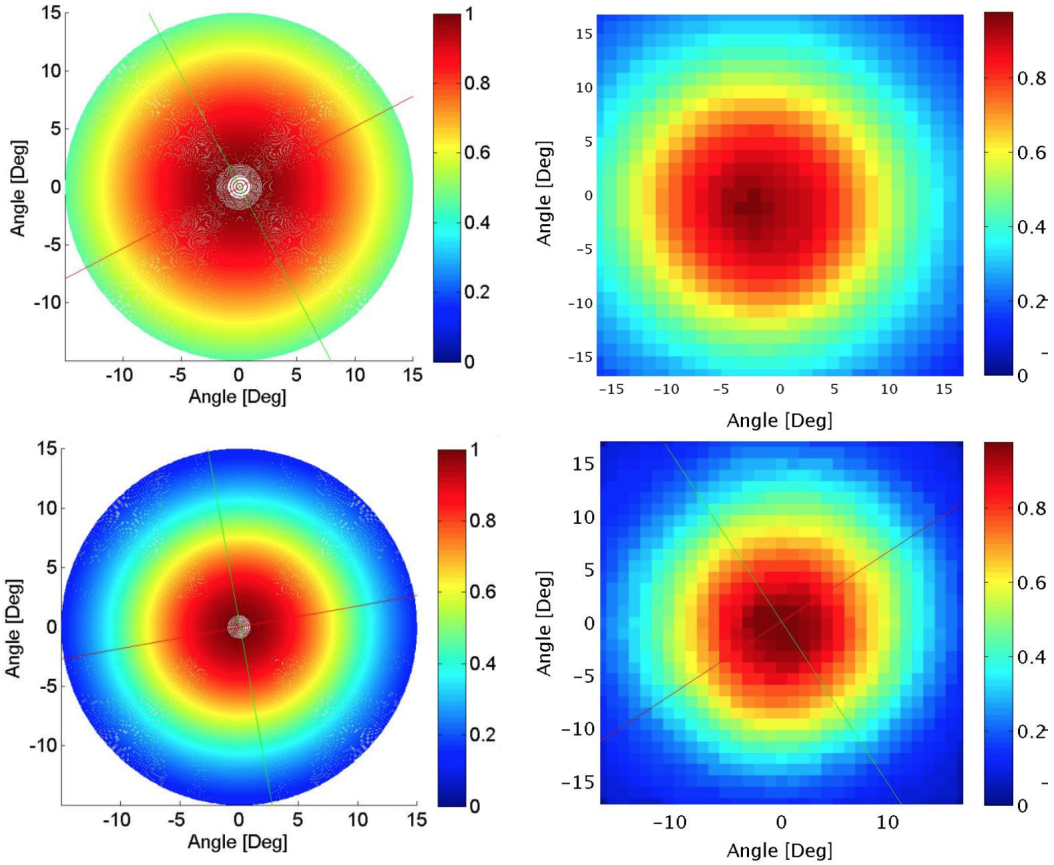

Figure 4.23: Beam maps results compared between HFSS and measurement. **Top Left** 95 GHz band beam map result from HFSS simulation. **Top Right** 95 GHz band beam map measured. **Bottom Left** 150 GHz band beam map result from HFSS simulation. **Bottom Right** 150 GHz band beam map measured. The FWHM of measured beam maps agree with HFSS simulations to within 7%.

Table 4.4: The summary of the test results

Description	95 GHz	150 GHz
Ellipticity (%)	1.5	1.93
Fractional bandwidth $\Delta\nu$ (GHz)	2.2×10^{10}	2.81×10^{10}
Efficiency (%)	35.6	32
Cross-pol (%)	5.1	2.3

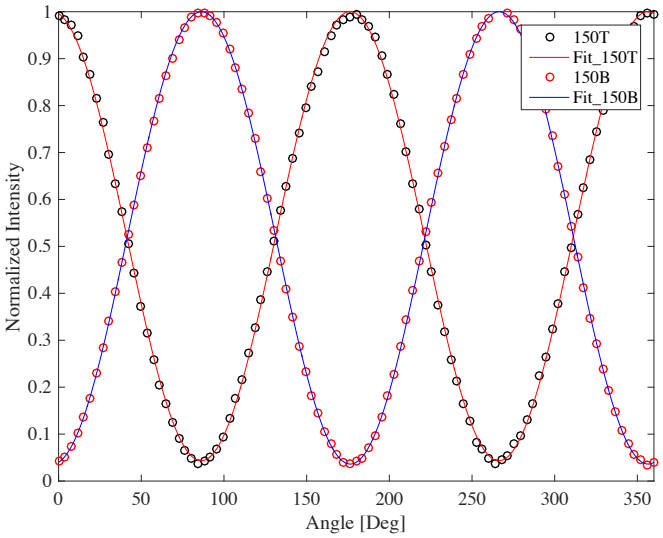

Figure 4.24: The polarization response of 150 GHz pixels.

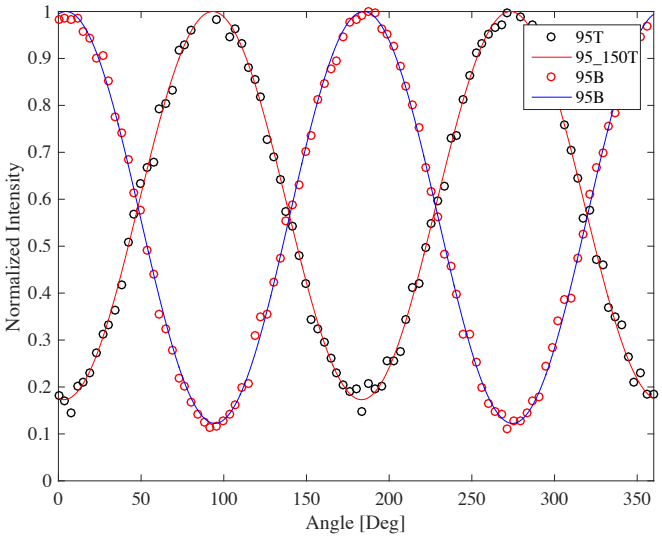

Figure 4.25: The polarization response of 150 GHz pixels.

4.11 Mass-Production

After the AR-coating prototype is proven to meet the POLARBEAR-2 performance criteria, we have to develop a mass-produced method to fabricate AR-coating lenslets for the entire POLARBEAR-2 focal plane. The first two POLARBEAR-2 receivers are identical which means at least 3,800 pixels have to be made. The single-mode type like is not suitable for creating coatings for kilo-order pixels. To do this the array mold was designed in which has the ability to coat multiple lenslets. To control the geometrical shape of the hemisphere cavity inside the mold, we switched to use a custom ball-end mill instead of CNC-lathe as in the prototype mold. All of the molds were machined at the Marine Physical Laboratory Research and Development Shop at Scripps Institution of Oceanography[10]. Four pins are used at each corner of the mold to be a guide when the cap and the mold are assembled. These pins are also designed to provide a tight fit, to make sure that lenslets will be perfectly aligned with the hemisphere cavity in the mold. The grooves are created next to the hemisphere cavity to relief excess Stycast from the hemisphere cavity. To ensure that there was no gap between the mold and cap, we used two screws to tighten down. This system with four guided pins will help control the translation error that can occur to meet our requirements. Each mold can fabricate up to nine AR-coatings per layer, reducing the time that we have to spend for cleaning up and preparation mold. A picture of the array mold is shown in Figure 4.26. Once the first layer of coating has been applied to the lenslet, the procedure is repeated with the mold designed for the second layer. After the coating process is completed,

[10]https://scripps.ucsd.edu/mpl/rd-machine-shop

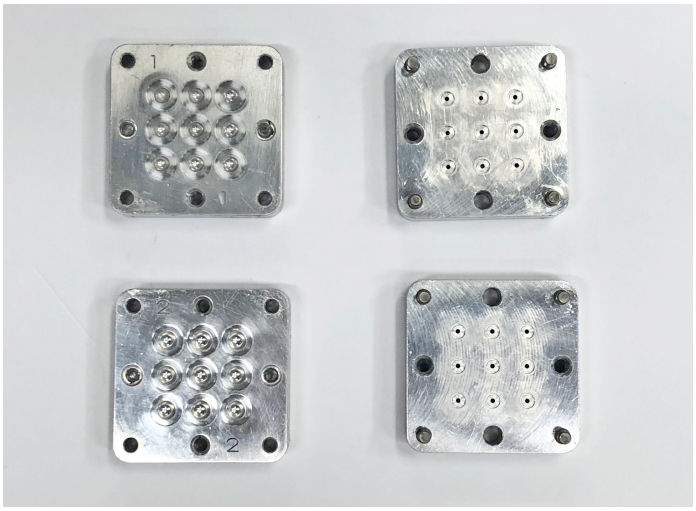

Figure 4.26: The array molds for mass-production

the coated lenslet will be populated on the seating wafer in the clean room. The procedure is summarized in Table **??**.

4.11.1 Populated AR coated lenslets process

The coated lenslets are seated in the pocket in a seating wafer. The lenslets are mounted in position using a drop of Stycast 2850FT on six edges of the coated lenslets. The bottom surface of the lenslets has to be cleared of any particulates. The gap between the surface of lenslets and the surface of the seating wafer pocket is less than 5 μm showed in Figure 4.17. The lenslets array is populated one rows at a time. In order to avoid a disturb lenslet's position while the epoxy is cured. The first row placed in the center of the wafer. A drop of Stycast 2850FT around the perimeter of the lenslets is used to attach AR coated lenslets to the wafer. The epoxy

Table 4.5: Fabrication AR coating flow table

	Process Description	Detail
1	Cleaning the molds	Using acetonitrile and methanol
2	Spraying the molds with ease release	Using Ease release200 to prevent Stycast adhering to the mold surface
3	Seating the lenslets on the cap	
4	Applying the adhestion promoter	Using Chemlok AP-134 Primer, Drying at 88 ^{o}C for 10 minutes
5	Deposit Stycast into mold cavity	Using fluid dispenser Performus VII
6	Assemblying the mold	
7	Curing process	curing temperature is 35 ^{o}C for 12 hours
8	Cleaning Measuring lenslets	Using acetonitrile and methanol for cleaning and using micrometer for measuring coated lenslets

drops are applied by the Performus VII fluid dispensing machine from Nordson[11]. The lenslets seating procedure is shown in Figure 4.27. A fully populated array is shown in Figure 4.28.

4.11.2 Assembly Wafer Module

We assemble a device wafer and lenslet wafer using a holder clip made from Invar, a nickel-iron single-phase alloy consisting of 36% of nickel and 64% of iron. Invar is known for its low coefficient of thermal expansion (CTE) as shown in Figure 4.35. Because of its uniquely low CTE, it used with silicon. Since the accuracy of alignment is necessary for the POLARBEAR-2, we created the alignment marks on

[11]http://www.nordson.com/en/divisions/efd/products/fluid-dispensing-systems/performus-series-dispensers

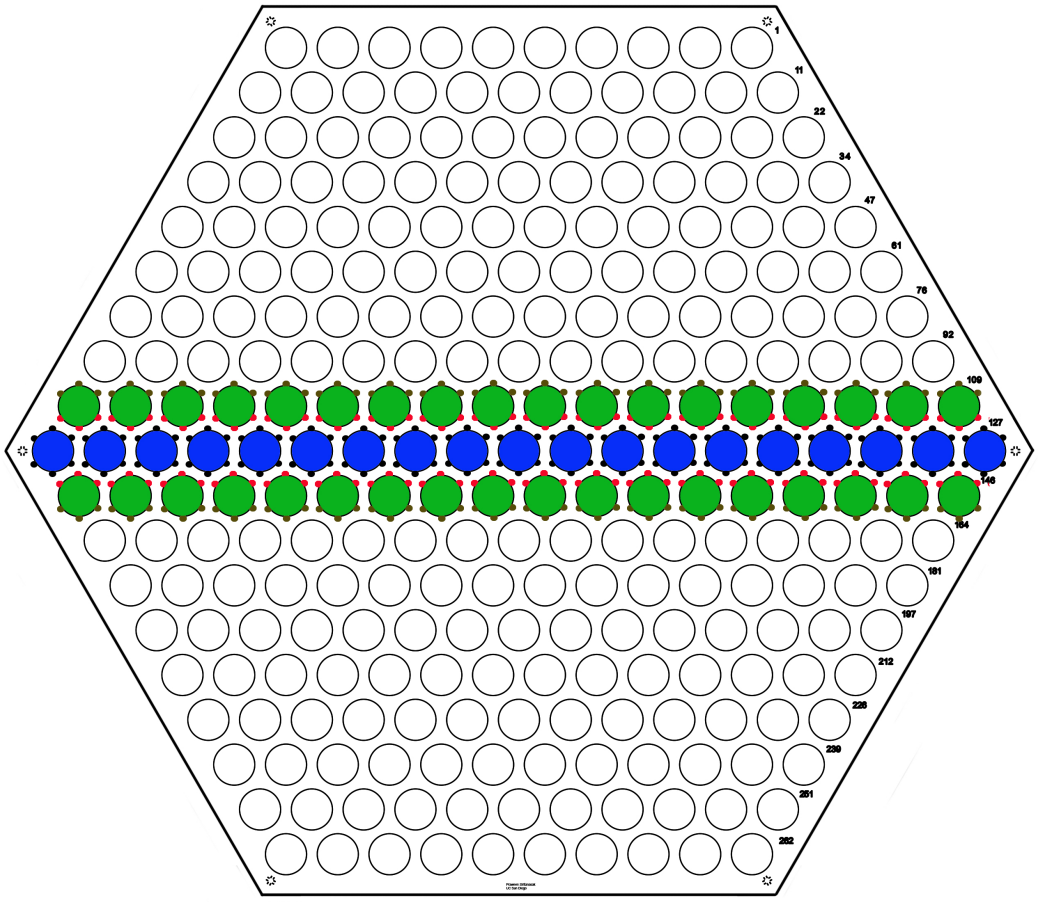

Figure 4.27: The procedure for populating AR coated lenslets on a seating wafer starts from the center row (blue). Stycast is deposited in six dots (black dots) around the coated lenslets glued to the seating wafer. After the Stycast drops attached to the center row were cured, we placed the coated lenslets on the next rows (green). The Stycast drops were then dispensed started from the outside (brown dots) to prevent coated lenslets from slipping during populated process. After coated lenslets were secured in the position, Stycast drops were appliped on the inner side (red dots).

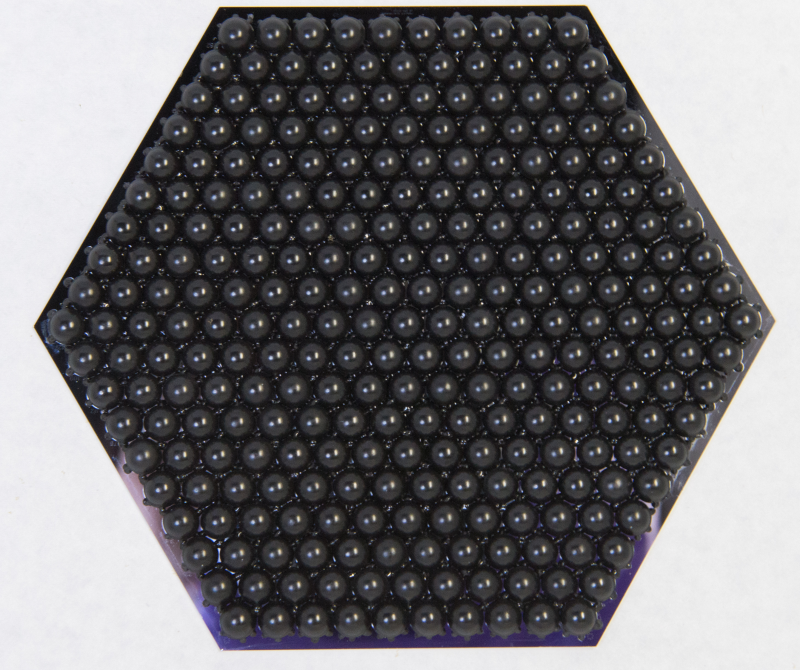

Figure 4.28: A photograph of the full populated lenslets on the seating wafer.

both wafers to help us aligned between two wafers as shown in Figure 4.29**C**. The halogen lamp is used to radiate Infrared (IR) light through the wafer. The IR light can penetrate through silicon but not a niobium ground plane layer in device wafer. The niobium layer was etched to create the alignment marks. Figure 4.29**B** showed a photograph from an IR camera above the lenslet wafer. The faint line in the picture is the alignment mark in the device wafer side overlay with the clear sharp rectangles from the lenslet wafer. These alignment marks allows us to align a lenslet wafer and a device wafer within 10 μm accuracy.

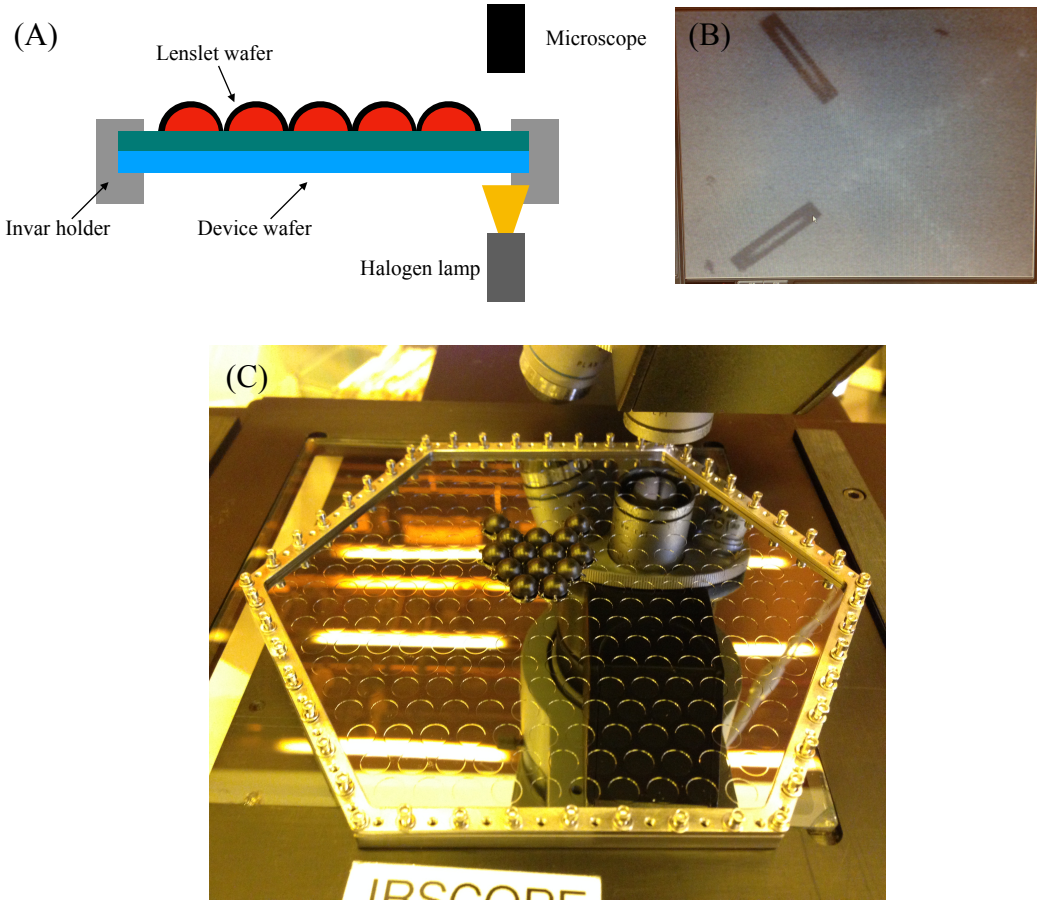

Figure 4.29: The setup for alignment between device wafer and lenslet wafer. **A**: the drawing of the setup, the lenslet wafer and the device wafer were attached together using the invar clips. The halogen lamp was used to generate Infrared light which can penetrate silicon wafers. **B**: IR photographs after the alignment two wafers. Two sharp rectangles are the alignment marks on the lenslet wafer and the blurry lines are the alignment marks on the device wafer. **C**: the photograph of the setup in the Nanolab, at UC Berkeley.

4.12 Beam Systematic Simulation

We used HFSS simulation to study the differenct scenarios of the AR coating that effects the detector beam. These studies include the misalignment of the AR coating to lenslet, the misalignment of the lenslet to the detector and the metal in proximity to a detector.

4.12.1 The Problem of Metal in Proximity to Detector

This problem was found during the witness pixel testing on the prototype POLARBEAR-2 detector where there was distortion in the beam map results. Later we found that a problem was caused by the invar clip that was used in the assembly of the lenslet wafer and the device wafer. This problem is unavoidable because the invar alloy is a necessary component in the POLARBEAR-2 focal plane. Hence, we have to study how close the invar can be to a detector.

The model of the partial invar clip with an AR coated lenslet was created in HFSS simulation as shown in Figure 4.30. The neighboring AR coated lenslets were not included in the model due to limit on the computational resource. For the 95 GHz pixel, we swept frequencies from 70 to 120 GHz with 5 GHz spacing, and 120 to 170 GHz with 5 GHz spacing for the 150 GHz pixel. The results from each frequency were then integrated to create the integrated beam maps.

Figure 4.31 shows that the invar corner clip has no effect on polarization wobble in the sinuous antenna. In the integrated beammaps showed in Figure 4.32, the beam maps of the model with the invar clip showed a higher ellipticity when

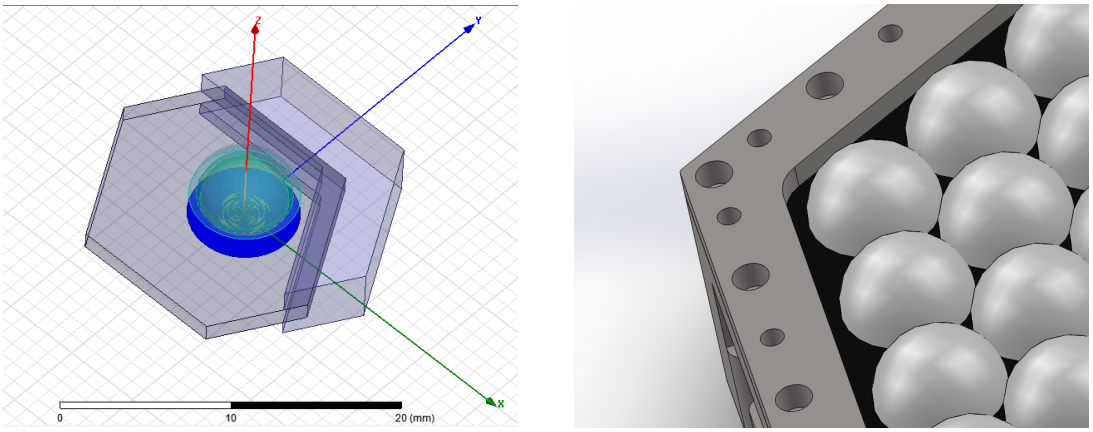

Figure 4.30: Metal in proximity a detector problem model setup. **Left**: HFSS model setup. **Right**: CAD model of the early version of the invar clip.

comparing to the model without the invar clip. The differential beammaps which was produced by subtracting the integrated beammaps from different polarization showed the dipole effect as expected. With this result, we can manage this systematic effect by a model with the differential pointing and ellipticity. This result also leads us to change the invar design to minimize the effect of invar clip to the detector.

4.12.2 Lenslets-antenna misalignment

With lenslet coupled antennas technology, there is a possibility that lenslets will not be aligned with their antennas. This misalignment can occur in each pixel, or with the entire wafer. The a case of slippage of each individual pixel, can randomly occur in any direction. The slippage of the whole wafer can be caused by how well we clamped each wafer or by thermal contraction between the wafer holder and the wafer. This scenario will be more likely to create systematic pointing error.

A HFSS model was used to simulate the effect on beam parameters due to

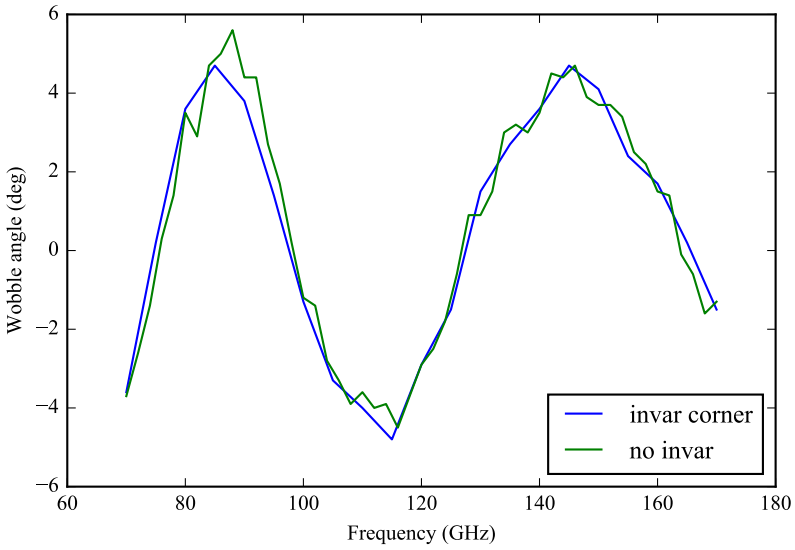

Figure 4.31: The effects of the invar corner clip proximity to polarization wobble. The polarization wobble is consistent with a model without the invar clip.

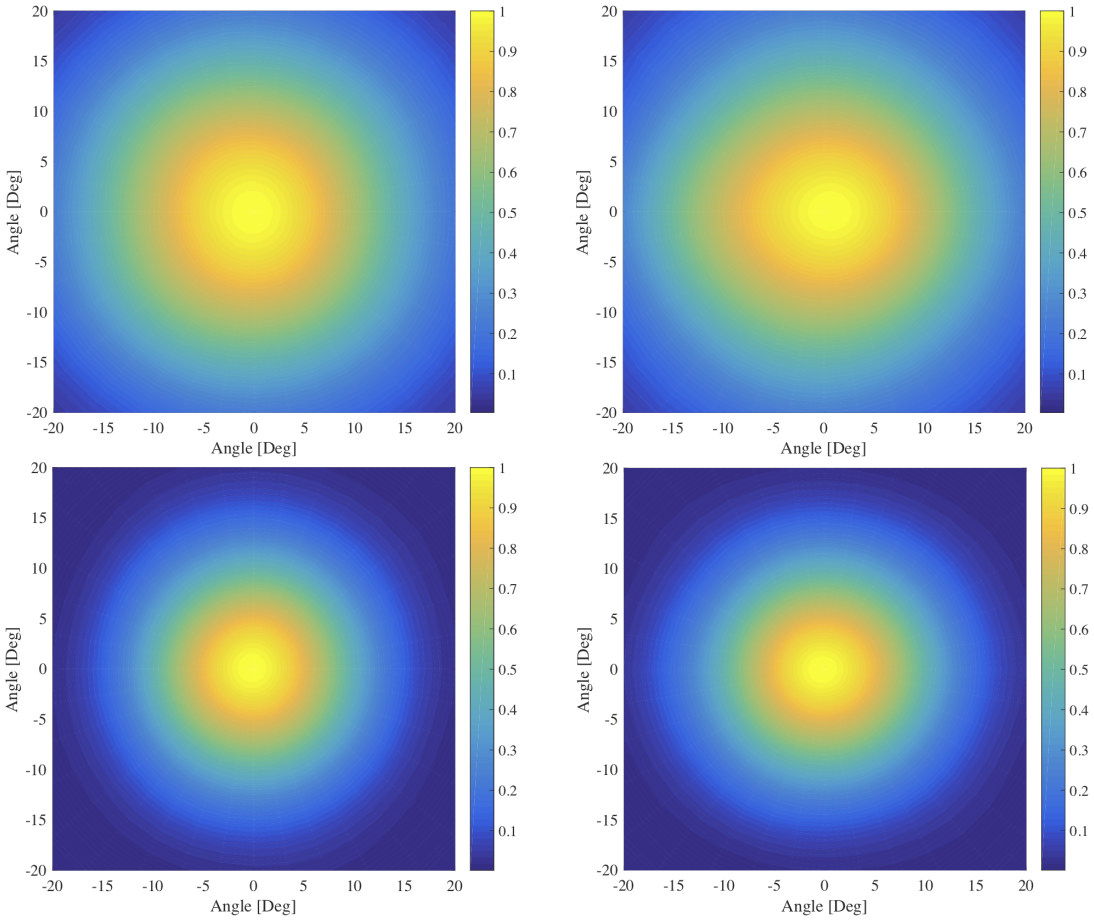

Figure 4.32: The 2D Beammap results from the HFSS simulation of the invar corner nearby the pixel. **Top row**; beam maps result from 95 GHz pixel. **Bottom row**; beam maps result from 150 GHz.

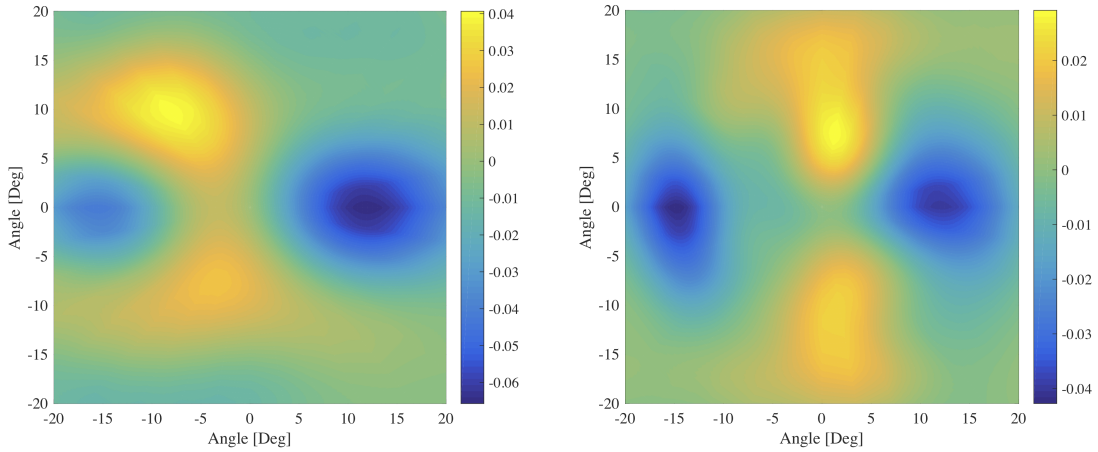

Figure 4.33: The differential beam maps from the invar corner clip simulation from 95 GHz pixel (left) and 150 GHz pixel (right). The beam map results were created using data from Figure 4.32.

misalignment of lenslet coupled antenna. After that, we used a ray tracing program Zemax[12] to estimate how much this contributed to the overall pointing error on the sky. The result of the simulation is shown in Figure 4.34. As expected, the pointing offset increases linearly with on the lenslet-antenna offset. This result will help us in the future to understand systematic uncertainties effect when the Simons Array starts observations.

4.13 Cryogenic Adhesion Property

Because the POLARBEAR-2 focal plane is cooled down to sub-Kelvin temperature, its AR coating also needs to be able to survive in the cryogenic environment. The primary cause of this failure comes from the thermal stress in the coating material.

[12]https://www.zemax.com/

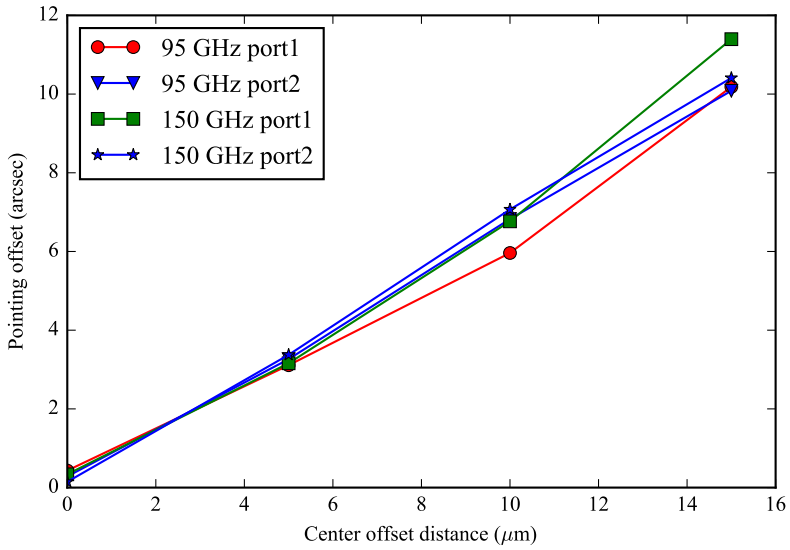

Figure 4.34: The pointing offset error from misalignment between antenna and AR coated lenslet.

4.13.1 Thermal Stress

Thermal stress is caused by the difference in the thermal expansion coefficient of materials. The thermal contraction is a one of the primary concern for choosing the material for coating the lenslet. Assuming negligible effect of pressure, the thermal contraction can be expressed as,

$$\frac{dL}{dT} = \alpha L \tag{4.19}$$

where dL/dT is the rate of change of that linear dimension per unit change in temperature, L is the length and α is the coefficient of thermal expansion (CTE). In this case, the boundary surface between silicon lenslets (α_s) and the coating (α_c),which

has the same L_0, will be shrink at the same rate.

$$\Delta L = L_0 \Delta T(\alpha_a - \alpha_c). \tag{4.20}$$

and the stress can be calculated from

$$\sigma = Y \Delta T(\alpha_a - \alpha_c), \tag{4.21}$$

where σ is the stress on the lenslets and Y is the Young's modulus.

Figure 4.35 showed a large mismatch between the CTE of silicon and Stycast 2850 FT at the temperature below 150 K which led to the thermal stress in lenslets. This could cause delamination of the coating on the lenslets. Lau et al. have demonstrated that the adhesion promoter Chemlok® AP-134 Primer[13] can prevent delamination when cooling to cryogenic temperatures [61]. We implemented this in the coating process and found the improvement in the number of the AR coating lenslets that survived in a cryogenic environment. However, it cannot guarantee that none of AR coating lenslets will fail. As a result, we adopted a screening method to help us find the potential failed coating lenslets.

The liquid Helium is used for the screening of the AR coating lenslets. Figure 4.36 showed the screening test setup. The AR coating lenslets have been packed inside aluminum trays to ensure all lenslets are uniformly cooled down to below 10 K. We used G10 to create insulation between the mainstage in the cryostat and the aluminum tray and copper wire as a heat link connection. This helps us to avoid a

[13]https://www.lord.com/products-and-solutions/chemlok-ap-134-primer

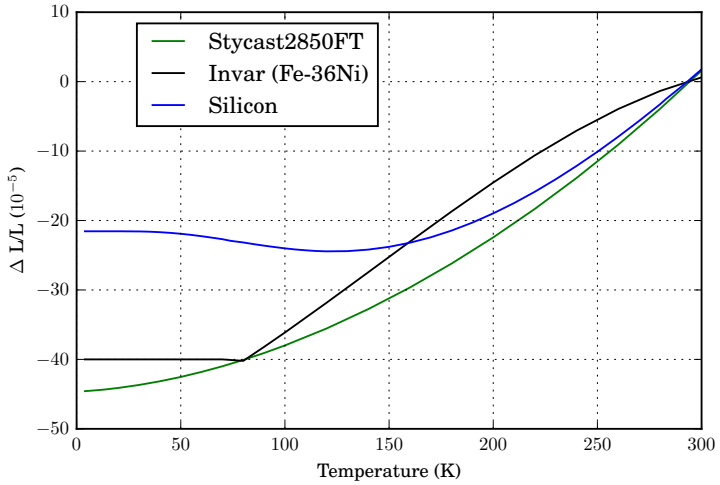

Figure 4.35: Linear thermal expansivity of Stycast2850 FT and Invar(Fe-36Ni), data are taken from [70–72]

rapid change in temperature which can cause the thermal shock in the AR coating lenslets. All of the AR coating lenslets have been cycled three times to less than 10 K. Then the lenslets that survived were selected to populate the seating wafer.

4.14 Another coating technology

This section, we will review other AR coating technology which CMB experiments used.

4.14.1 Plastic Sheet Coating

The plastic sheet coating method is used because it is commercially available such as PEI in the POLARBEAR or Skybond in alumina lens in the POLARBEAR-2.

Figure 4.36: AR coating lenslets screening setup.

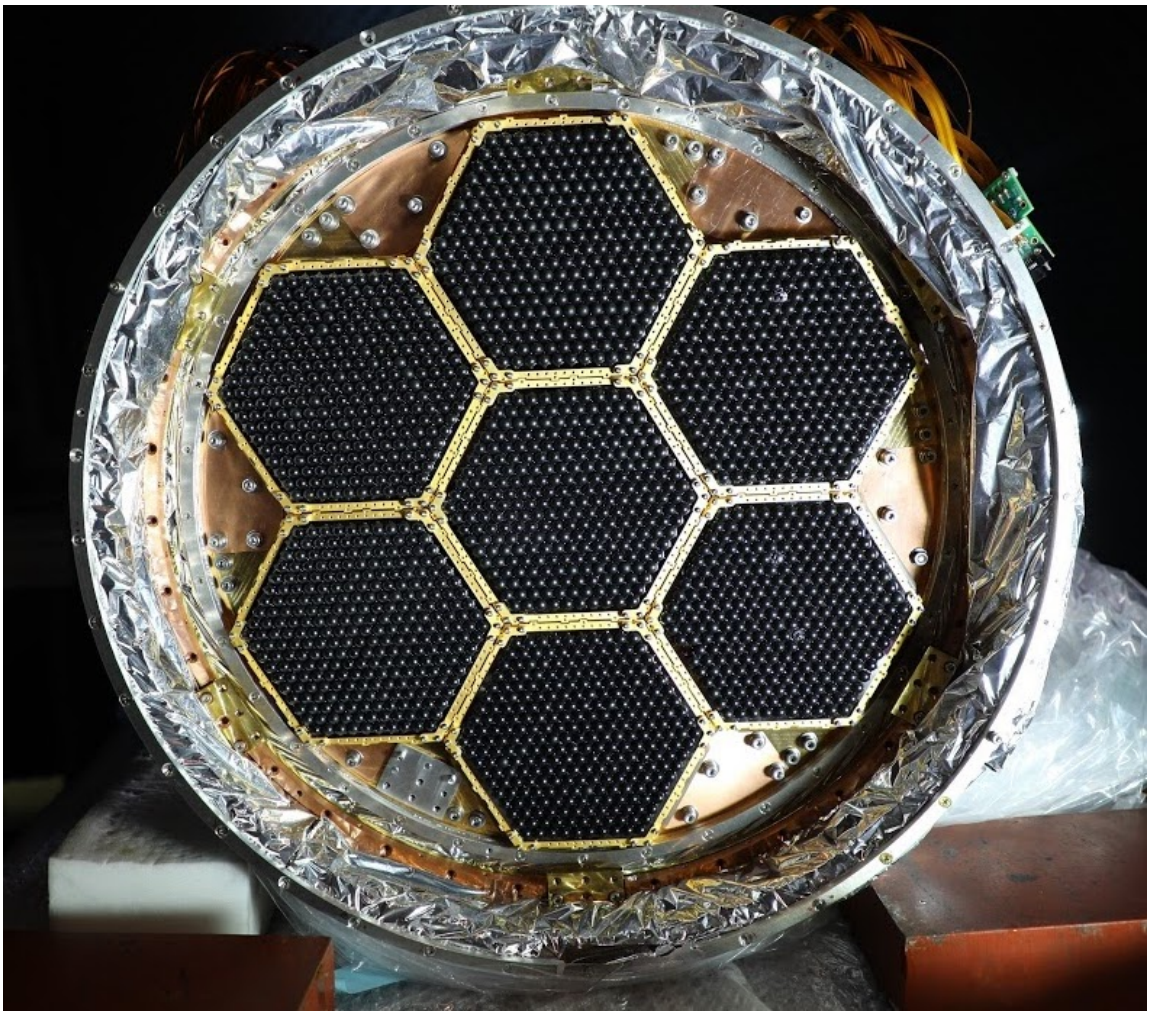

Figure 4.37: A photograph of the full assembly arrays for an integrated focal plane testing. The picture shows all seven sub-array modules integrated with the focal plane tower. The testing is underway in KEK, Japan (status of Feb 2018).

Table 4.6: A table of the properties of Stycast2850FT and Stycast1090

Description	Stycast2850FT	Stycast1090
Specific Gravity	2.3	0.88
Viscosity (mixed)	5,600 cP	29,000 cP
Hardness	94	82
Tensile Strength	60MPa	32MPa
Compressive Modulus	80 MPa	25MPa
Thermal Conductivity	1.44 $Wm^{-1}\ ^{\circ}C^{-1}$	0.167 $Wm^{-1}\ ^{\circ}C^{-1}$
Electrical Resistivity(Volume)	5×10^{12} Wm	10×10^{12} Wm

Applying the plastic sheet on the lenses surface require a uniform adhesive layer. This becomes a challenging especially for a highly curved lens like a lenslet. The common method for applying the coating on high curvature surface is thermoforming the plastic sheet into lens shape then uses the epoxy such as Stycast1266 to glue the plastic sheet to a lens surface. The thermal contraction between lens material and plastic sheets also the main issue since the plastic sheets usually have a high CTE than silicon or alumina. The solution that mitigates this problem is dicing a stress relief groove into the plastic layer.

4.14.2 Thermal Spray Coating

Thermal spray coating method is a coating technique that uses a plasma jet to melt the base material and spray on to the surface. The material is then cooled down immediately to create a coating layer without using any glue. The base material is a low loss-tangent mixture of alumina and silica. The dielectric constant of the coating material can be controlled by changing the mixing ratio of the hollow alumina microspheres which vary the porosity of the material. Since the alumina-

silica coating has a low CTE that matches with alumina, it can mitigate the cryogenic delamination problem [73]. This method has been used in the reimaging lens in the POLARBEAR-2 receiver. For the highly curved lens like lenslet, this method has been proven in the concept and plans to be use for the third POLARBEAR-2 receiver in the Simons Array.

4.14.3 Metameterial Coating

The metamaterial coating method is a technique of cutting subwavelength size structures into a surface of the refractive optical element. This method can mitigate the cryogenic delamination because it cut directly into the surface of an optical element. There are several ways to create the metamaterial coating, diced silicon lens, deep dry etched silicon, machined plastic lens and laser ablated surface.

Diced Silicon Lens

This method is using a dicing saw blade to create a groove on the silicon lens surface. The multi-layer coating can be fabricated by stepping cut deeper and thinner grove into the lens. This technique has been demonstrated by ACTPOL and the advACT [74]. This method is limited by the size of the single crystal silicon available. It is also difficult to dice a highly curved surface lens.

Deep Dry Etched Silicon

This is an alternative solution for a diced silicon lens. Comparing to the diced silicon lens method, the deep dry etched silicon can be done in a less time.

This method uses the DRIE to etch silicon wafer. It has only been demonstrated only on a flat 100 mm diameter silicon wafer [75]. The challenge for this method is how to apply on the curved surface since it can etch only on silicon wafers.

Machined Plastic

This method uses a conventional CNC milling machine to create a grid of sub-wavelength holes cut in the surface of plastic lenses. These holes are tunes for the required frequency band and refractive index. This technology has been demonstrated with SPT-3G windows. The advantage of this method is the convenience however, it can be applied only to material that CNC milling can machine.

Laser Ablated Surface

For the material such as alumina or sapphire that is difficult to dice, dry etch or machine, the laser ablation can be used for fabricating metamaterial AR coatings. This technology has been demonstrated by Matsumura et al [76]. They used a 515 nm laser to produce the pyramid-shaped structure with a pitch of 320 μm and a total height of near 800 μm. This method is still in the early stage of development and has been performed only on the flat surface. Laser ablating over the whole surface area is also a time-consuming process.

4.14.4 Metamaterial Lenslet Arrays

This is an alternative method for a broadband lenslet-couple antenna system. The metamaterials are fabricated using a stack of silicon wafers, each patterned with

Figure 4.38: A cartoon drawing of the cross section of the metamaterial. **Left**: the cross section of the metamaterial from the step dicing. **Right**: the cross section of the pyramid-shaped metamaterial.

a periodic array of subwavelength features to create a lenslet. This method can be used for this is a gradient index (GRIN) lenslet. GRIN lenslets are produced by varying etched holes in the silicon wafer radially to create lenslets patterns. These etched holes pattern will act as the AR coating similar to a deep etched silicon method which we previously discussed. This method has been introduced with a single-layer etched GRIN as a candidate lenslet array for the MAKO instruments [77]. There is also has a study using GRIN array for terahertz application from 0.3-1.6 THz [78]. This technology is still in the early stage of development, a lot more the studies need to be done before it can be deployed in the future experiments such as the beam profile and the polarization systematic.

4.15 Acknowledgement

Figure 4.6 is a reprint of material as it appears in: Darin Rosen, Aritoki Suzuki, Brian Keating, William Krantz, Adrian T. Lee, Erin Quealy, Paul L. Richards, Praween Siritanasak, and William Walker, "Epoxy-based broadband antireflection coating for millimeter-wave optics," Appl. Opt. 52, 8102-8105 (2013). The dissertation author made essential contributions to many aspects of this work.

Figure 4.21 and 4.23 are reprints of material as it appears in: P. Siritanasak, C. Aleman, K. Arnold, A. Cukierman, M. Hazumi, K. Kazemzadeh, B. Keating, T. Matsumura, A. T. Lee, C. Lee, E. Quealy, D. Rosen, N. Stebor, and A. Suzuki, "The broadband anti-reflection coated extended hemispherical silicon lenses for polarbear-2 experiment," Journal of Low Temperature Physics, vol. 184, pp. 553-558, Aug 2016. The dissertation author was the primary author of this paper.

Chapter 5

The Future of CMB Experiments

5.1 Introduction

One of the biggest challenge in the cosmology is to find evidence for the inflation theory. Countless experiments have been designed to detect the faint primordial B-mode polarization signal, only to end up placed the upper limits. With rapid improvement to the the sensitivity of the experiments in the recent years, the B-mode polarization at small angular scales was discovered.

In contrast with the lensing B-mode signal, the primordial B-mode from the inflation is still unknown. The recent BICEP2 result of B-mode signal at large angular scale turns out to be a contaminated signal from foreground dust. This drives the next generation CMB experiments to extend their observing frequencies to multiple bands in order to understand and measure the foreground contamination.

In this chapter, we will discuss the current status of the CMB B-mode mea-

surement in 2017, review upcoming experiments and the future beyond the next generation of CMB experiment.

5.2 Current status

As discussed in Chapter 1, there are many experiments that studies the CMB. After COBE satellite, there are a number of experiments ranges from satellite-based, balloon-borne and ground-based that aim to study the CMB such as WMAP, Planck, MAXIMA, BLAST, BICEP, the Atacama Cosmology Telescope (ACT), the South Pole Telescope (SPT), and the POLARBEAR. Currently, only B-modes from lensing have been observed [32,34,35,79]. Figure 5.1 shows the current CMB B-mode power spectrum result including the upper limits published by the experiments before 2014. This serves as a cornerstone for the sensitivity of the measurement. The primordial CMB B-Mode is still undetected. The current best upper limit on the primordial signal and the tensor-to-scalar ratio r is set by the BICEP2 and Keck array experiment at $r < 0.09$ at the 95% confidence level [80]. The limitation comes from the emission of galactic dust in the millimeter wavelength. This shows the importance of accurate foreground modeling in order to subtract the contamination from the CMB data.

5.3 Future Outlook

Next generation of CMB experiment will measure the CMB polarization and study the foreground contamination at multiple frequencies. AdvACT [30],

CLASS [81], SPT3G [29], BICEP3 [82] and the Simons Array [28] are examples of the experiments that will use this method. These experiments will have improvement in detector count and array sensitivity compared to there predecessors. There will also be improvement in bandwidth using multichroic pixels. These experiments are expected to pursue the detection of primordial B-mode polarization and constrain cosmological parameters such as r and a sum of the neutrinos masses and to better the understanding of the physics of the universe.

5.3.1 The Simons Observatory

The Simons Observatory is a collaboration between the U.S. Department of Energy's Lawrence Berkeley National Laboratory, UC Berkeley, Princeton University, the University of California at San Diego and the University of Pennsylvania and many more. The Simons Foundation has given $38.4 million to establish new telescopes in the Atacama desert in Chile alongside the current experiment including the Simons Array and the Atacama Cosmology Telescope (ACT). It will accelerate the research of the further technology for developing a next-generation receiver to pursue a detection of primordial B-mode. The experiment is currently in the early design stage. The project will pave a way for future ground-based experiment CMB Stage-4 experiment.

5.3.2 The CMB-S4 experiment

The "Stage-4" ground-based cosmic microwave background (CMB) experiment, CMB-S4, is the proposed collaboration from the ground-based experiments

with a goal of pushing the sensitivity limit from the ground. CMB-S4 consists of telescopes operating from the south pole and the Atacama desert. It is targeted to have detector count of $\sim$ 500,000 and sensitivity of $\sigma(r) = 0.0005$, $\sigma(\sum_\nu m_\nu) = 15$ meV, and $\sigma(N_{eff})$=0.027. This will provide big leap forward for our understanding the nature of the universe. CMB-S4 is slated to start after 2020 [83].

5.3.3 LiteBIRD

While sensitivity of ground-based experiments can be improved by increasing the number of detectors, they are still limited by the atmospheric windows and the lack of the ability to observe the entire sky. These limitations do not exist in space. LiteBIRD is an international satellite proposal lead by JAXA to aim for probe the inflationary paradigm from CMB polarization. LiteBIRD plans to observe the CMB over the full sky at the second Lagrange point for three years. Their focal plane will consist of detectors with operating from 40 to 402 GHz, divided to 15 different bands. Its detector sensitivity is expected to reach $\sigma(r) = 0.001$. The current target launch is 2024-2025 [84].

5.4 Acknowledgement

Figure 5.1 was provided by Yuji Chinone.

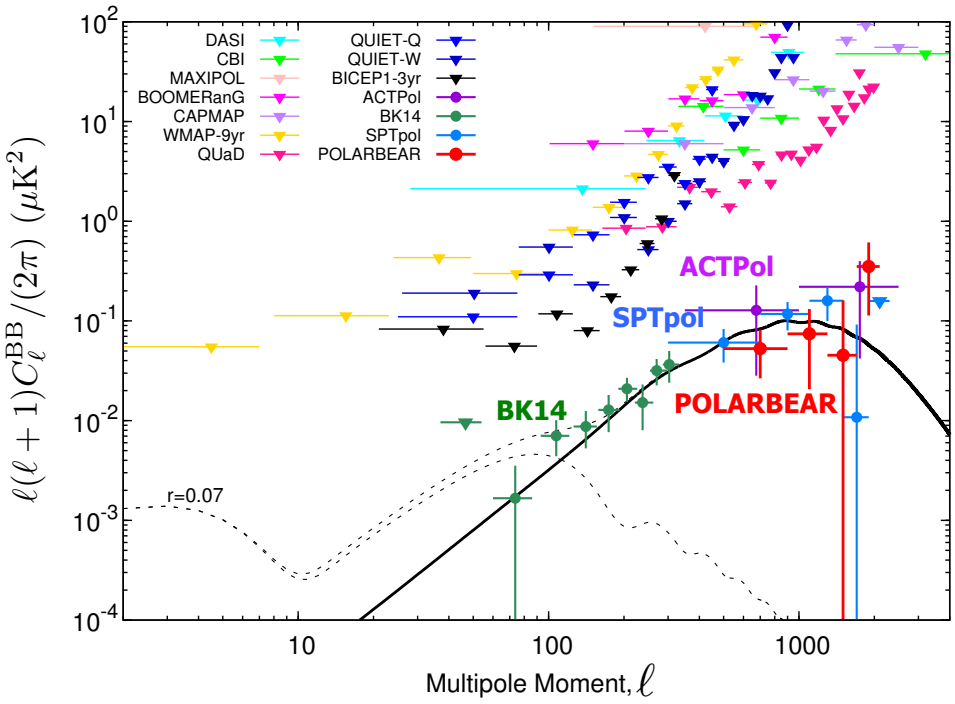

Figure 5.1: Current CMB B-Mode power spectrum results. This plot shows the published measurement result of the C_ℓ^{BB} spectrum as of Oct 2017. The result from BICEP2 and Keck array [85] is shown in green, SPTpol [34] is shown in blue, ACTpol [86] in purple and the POLARBEAR [45] in red. The experiments result before 2014 are plotted as the upper limits. This plot is provided by Yuji Chinone.

Table 5.1: The parameter of Λ CDM cosmology from PlanckXIII 2015

Parameter	Fit	Description
$\Omega_b h^2$	0.02230 ± 0.00014	Baryon density parameter
$\Omega_c h^2$	0.1188 ± 0.0010	Dark matter density parameter
$100\theta_{MC}$	1.04093 ± 0.00030	A measure of the sound horizon at last scattering
τ	0.066 ± 0.012	Reionization optical depth
H_0	67.74 ± 0.46	Hubble constant
n_s	0.9667 ± 0.0040	Scalar spectral index
Ω_m	0.3089 ± 0.0062	Matter density parameter
Ω_Λ	0.6911 ± 0.0062	Dark energy density parameter
σ_8	0.8159 ± 0.0086	Fluctuation amplitude at 8 h^{-1} Mpc
t_0	$13.799 \pm 0.021 \times 10^9$ years	Age of the universe
w	$-1.019^{+0.075}_{-0.080}$	Equation of state of dark energy
r	< 0.09	Tensor to scalar ratio

Bibliography

[1] J. Dowson, *A classical dictionary of Hindu mythology and religion, geography, history, and literature.* London : TrÃijbner, 1879.

[2] P. Curd, "Anaxagoras," in *The Stanford Encyclopedia of Philosophy* (E. N. Zalta, ed.), Metaphysics Research Lab, Stanford University, winter 2015 ed., 2015.

[3] A. A. Penzias and R. W. Wilson, "A Measurement of excess antenna temperature at 4080-Mc/s," *Astrophys. J.*, vol. 142, pp. 419–421, 1965.

[4] B. Ryden, *Introduction to Cosmology.* Cambridge University Press, 2016.

[5] G. Lemaître, "Un Univers homogène de masse constante et de rayon croissant rendant compte de la vitesse radiale des nébuleuses extra-galactiques," *Annales de la Société Scientifique de Bruxelles*, vol. 47, pp. 49–59, 1927.

[6] Planck Collaboration, Ade, P. A. R., Aghanim, N., Arnaud, M., Ashdown, M., Aumont, J., Baccigalupi, C., Banday, A. J., Barreiro, R. B., Bartlett, J. G., Bartolo, N., Battaner, E., Battye, R., Benabed, K., Benoît, A., Benoit-Lévy, A., Bernard, J.-P., Bersanelli, M., Bielewicz, P., Bock, J. J., Bonaldi, A., Bonavera, L., Bond, J. R., Borrill, J., Bouchet, F. R., Boulanger, F., Bucher, M., Burigana, C., Butler, R. C., Calabrese, E., Cardoso, J.-F., Catalano, A., Challinor, A., Chamballu, A., Chary, R.-R., Chiang, H. C., Chluba, J., Christensen, P. R., Church, S., Clements, D. L., Colombi, S., Colombo, L. P. L., Combet, C., Coulais, A., Crill, B. P., Curto, A., Cuttaia, F., Danese, L., Davies, R. D., Davis, R. J., de Bernardis, P., de Rosa, A., de Zotti, G., Delabrouille, J., Désert, F.-X., Di Valentino, E., Dickinson, C., Diego, J. M., Dolag, K., Dole, H., Donzelli, S., Doré, O., Douspis, M., Ducout, A., Dunkley, J., Dupac, X., Efstathiou, G., Elsner, F., EnSSlin, T. A., Eriksen, H. K., Farhang, M., Fergusson, J., Finelli, F., Forni, O., Frailis, M., Fraisse, A. A., Franceschi, E., Frejsel, A., Galeotta,

S., Galli, S., Ganga, K., Gauthier, C., Gerbino, M., Ghosh, T., Giard, M., Giraud-Héraud, Y., Giusarma, E., Gjerløw, E., González-Nuevo, J., Górski, K. M., Gratton, S., Gregorio, A., Gruppuso, A., Gudmundsson, J. E., Hamann, J., Hansen, F. K., Hanson, D., Harrison, D. L., Helou, G., Henrot-Versillé, S., Hernández-Monteagudo, C., Herranz, D., Hildebrandt, S. R., Hivon, E., Hobson, M., Holmes, W. A., Hornstrup, A., Hovest, W., Huang, Z., Huffenberger, K. M., Hurier, G., Jaffe, A. H., Jaffe, T. R., Jones, W. C., Juvela, M., Keihänen, E., Keskitalo, R., Kisner, T. S., Kneissl, R., Knoche, J., Knox, L., Kunz, M., Kurki-Suonio, H., Lagache, G., Lähteenmäki, A., Lamarre, J.-M., Lasenby, A., Lattanzi, M., Lawrence, C. R., Leahy, J. P., Leonardi, R., Lesgourgues, J., Levrier, F., Lewis, A., Liguori, M., Lilje, P. B., Linden-Vørnle, M., López-Caniego, M., Lubin, P. M., Macías-Pérez, J. F., Maggio, G., Maino, D., Mandolesi, N., Mangilli, A., Marchini, A., Maris, M., Martin, P. G., Martinelli, M., Martínez-González, E., Masi, S., Matarrese, S., McGehee, P., Meinhold, P. R., Melchiorri, A., Melin, J.-B., Mendes, L., Mennella, A., Migliaccio, M., Millea, M., Mitra, S., Miville-Deschênes, M.-A., Moneti, A., Montier, L., Morgante, G., Mortlock, D., Moss, A., Munshi, D., Murphy, J. A., Naselsky, P., Nati, F., Natoli, P., Netterfield, C. B., Nørgaard-Nielsen, H. U., Noviello, F., Novikov, D., Novikov, I., Oxborrow, C. A., Paci, F., Pagano, L., Pajot, F., Paladini, R., Paoletti, D., Partridge, B., Pasian, F., Patanchon, G., Pearson, T. J., Perdereau, O., Perotto, L., Perrotta, F., Pettorino, V., Piacentini, F., Piat, M., Pierpaoli, E., Pietrobon, D., Plaszczynski, S., Pointecouteau, E., Polenta, G., Popa, L., Pratt, G. W., Prézeau, G., Prunet, S., Puget, J.-L., Rachen, J. P., Reach, W. T., Rebolo, R., Reinecke, M., Remazeilles, M., Renault, C., Renzi, A., Ristorcelli, I., Rocha, G., Rosset, C., Rossetti, M., Roudier, G., Rouillé d?Orfeuil, B., Rowan-Robinson, M., Rubiño-Martín, J. A., Rusholme, B., Said, N., Salvatelli, V., Salvati, L., Sandri, M., Santos, D., Savelainen, M., Savini, G., Scott, D., Seiffert, M. D., Serra, P., Shellard, E. P. S., Spencer, L. D., Spinelli, M., Stolyarov, V., Stompor, R., Sudiwala, R., Sunyaev, R., Sutton, D., Suur-Uski, A.-S., Sygnet, J.-F., Tauber, J. A., Terenzi, L., Toffolatti, L., Tomasi, M., Tristram, M., Trombetti, T., Tucci, M., Tuovinen, J., Türler, M., Umana, G., Valenziano, L., Valiviita, J., Van Tent, F., Vielva, P., Villa, F., Wade, L. A., Wandelt, B. D., Wehus, I. K., White, M., White, S. D. M., Wilkinson, A., Yvon, D., Zacchei, A., and Zonca, A., "Planck 2015 results - xiii. cosmological parameters," *A&A*, vol. 594, p. A13, 2016.

[7] A. H. Guth, "Inflationary universe: A possible solution to the horizon and flatness problems," *Phys. Rev. D*, vol. 23, pp. 347–356, Jan 1981.

[8] A. Linde, "A new inflationary universe scenario: A possible solution of the horizon, flatness, homogeneity, isotropy and primordial monopole problems," *Physics Letters B*, vol. 108, no. 6, pp. 389 – 393, 1982.

[9] A. Albrecht and P. J. Steinhardt, "Cosmology for grand unified theories with radiatively induced symmetry breaking," *Phys. Rev. Lett.*, vol. 48, pp. 1220–1223, Apr 1982.

[10] G. Gamow, "The origin of elements and the separation of galaxies," *Phys. Rev.*, vol. 74, pp. 505–506, Aug 1948.

[11] R. A. Alpher and R. C. Herman, "On the relative abundance of the elements," *Phys. Rev.*, vol. 74, pp. 1737–1742, Dec 1948.

[12] J. C. Mather, E. S. Cheng, D. A. Cottingham, R. E. Eplee, Jr., D. J. Fixsen, T. Hewagama, R. B. Isaacman, K. A. Jensen, S. S. Meyer, P. D. Noerdlinger, S. M. Read, L. P. Rosen, R. A. Shafer, E. L. Wright, C. L. Bennett, N. W. Boggess, M. G. Hauser, T. Kelsall, S. H. Moseley, Jr., R. F. Silverberg, G. F. Smoot, R. Weiss, and D. T. Wilkinson, "Measurement of the cosmic microwave background spectrum by the COBE FIRAS instrument," *The Astrophysical Journal*, vol. 420, pp. 439–444, Jan. 1994.

[13] Planck Collaboration, Aghanim, N., Arnaud, M., Ashdown, M., Aumont, J., Baccigalupi, C., Banday, A. J., Barreiro, R. B., Bartlett, J. G., Bartolo, N., Battaner, E., Benabed, K., BenoÃőt, A., Benoit-LÃľvy, A., Bernard, J.-P., Bersanelli, M., Bielewicz, P., Bock, J. J., Bonaldi, A., Bonavera, L., Bond, J. R., Borrill, J., Bouchet, F. R., Boulanger, F., Bucher, M., Burigana, C., Butler, R. C., Calabrese, E., Cardoso, J.-F., Catalano, A., Challinor, A., Chiang, H. C., Christensen, P. R., Clements, D. L., Colombo, L. P. L., Combet, C., Coulais, A., Crill, B. P., Curto, A., Cuttaia, F., Danese, L., Davies, R. D., Davis, R. J., de Bernardis, P., de Rosa, A., de Zotti, G., Delabrouille, J., DÃľsert, F.-X., Di Valentino, E., Dickinson, C., Diego, J. M., Dolag, K., Dole, H., Donzelli, S., DorÃľ, O., Douspis, M., Ducout, A., Dunkley, J., Dupac, X., Efstathiou, G., Elsner, F., EnÃ§lin, T. A., Eriksen, H. K., Fergusson, J., Finelli, F., Forni, O., Frailis, M., Fraisse, A. A., Franceschi, E., Frejsel, A., Galeotta, S., Galli, S., Ganga, K., Gauthier, C., Gerbino, M., Giard, M., GjerlÃÿw, E., GonzÃąlez-Nuevo, J., GÃşrski, K. M., Gratton, S., Gregorio, A., Gruppuso, A., Gudmundsson, J. E., Hamann, J., Hansen, F. K., Harrison, D. L., Helou, G., Henrot-VersillÃľ, S., HernÃąndez-Monteagudo, C., Herranz, D., Hildebrandt, S. R., Hivon, E., Holmes, W. A., Hornstrup, A., Huffenberger, K. M., Hurier, G.,

Jaffe, A. H., Jones, W. C., Juvela, M., KeihÃď nen, E., Keskitalo, R., Kiiveri, K., Knoche, J., Knox, L., Kunz, M., Kurki-Suonio, H., Lagache, G., LÃď hteenmÃď ki, A., Lamarre, J.-M., Lasenby, A., Lattanzi, M., Lawrence, C. R., Le Jeune, M., Leonardi, R., Lesgourgues, J., Levrier, F., Lewis, A., Liguori, M., Lilje, P. B., Lilley, M., Linden-VÃÿrnle, M., Lindholm, V., LÃşpez-Caniego, M., MacÃŋas-PÃľrez, J. F., Maffei, B., Maggio, G., Maino, D., Mandolesi, N., Mangilli, A., Maris, M., Martin, P. G., MartÃŋnez-GonzÃąlez, E., Masi, S., Matarrese, S., Meinhold, P. R., Melchiorri, A., Migliaccio, M., Millea, M., Mitra, S., Miville-DeschÃłnes, M.-A., Moneti, A., Montier, L., Morgante, G., Mortlock, D., Mottet, S., Munshi, D., Murphy, J. A., Narimani, A., Naselsky, P., Nati, F., Natoli, P., Noviello, F., Novikov, D., Novikov, I., Oxborrow, C. A., Paci, F., Pagano, L., Pajot, F., Paoletti, D., Partridge, B., Pasian, F., Patanchon, G., Pearson, T. J., Perdereau, O., Perotto, L., Pettorino, V., Piacentini, F., Piat, M., Pierpaoli, E., Pietrobon, D., Plaszczynski, S., Pointecouteau, E., Polenta, G., Ponthieu, N., Pratt, G. W., Prunet, S., Puget, J.-L., Rachen, J. P., Reinecke, M., Remazeilles, M., Renault, C., Renzi, A., Ristorcelli, I., Rocha, G., Rossetti, M., Roudier, G., RouillÃľ dâĂŹOrfeuil, B., RubiÃśo-MartÃŋn, J. A., Rusholme, B., Salvati, L., Sandri, M., Santos, D., Savelainen, M., Savini, G., Scott, D., Serra, P., Spencer, L. D., Spinelli, M., Stolyarov, V., Stompor, R., Sunyaev, R., Sutton, D., Suur-Uski, A.-S., Sygnet, J.-F., Tauber, J. A., Terenzi, L., Toffolatti, L., Tomasi, M., Tristram, M., Trombetti, T., Tucci, M., Tuovinen, J., Umana, G., Valenziano, L., Valiviita, J., Van Tent, F., Vielva, P., Villa, F., Wade, L. A., Wandelt, B. D., Wehus, I. K., Yvon, D., Zacchei, A., and Zonca, A., "Planck 2015 results - xi. cmb power spectra, likelihoods, and robustness of parameters," *A&A*, vol. 594, p. A11, 2016.

[14] M. Kamionkowski, A. Kosowsky, and A. Stebbins, "A Probe of primordial gravity waves and vorticity," *Phys. Rev. Lett.*, vol. 78, pp. 2058–2061, 1997.

[15] U. b. u. Seljak and M. Zaldarriaga, "Signature of gravity waves in the polarization of the microwave background," *Phys. Rev. Lett.*, vol. 78, pp. 2054–2057, Mar 1997.

[16] M. Zaldarriaga and U. c. v. Seljak, "Gravitational lensing effect on cosmic microwave background polarization," *Phys. Rev. D*, vol. 58, p. 023003, Jun 1998.

[17] W. Hu and T. Okamoto, "Mass reconstruction with cosmic microwave background polarization," *The Astrophysical Journal*, vol. 574, no. 2, p. 566, 2002.

[18] A. Lewis, A. Challinor, and A. Lasenby, "Efficient computation of cosmic microwave background anisotropies in closed friedmann-robertson-walker models," *The Astrophysical Journal*, vol. 538, no. 2, p. 473, 2000.

[19] L. Cayon, E. Martinez-Gonzalez, and J. L. Sanz, "Gravitational lensing and the cosmic microwave background," *The Astrophysical Journal*, vol. 403, pp. 471–475, Feb. 1993.

[20] U. Seljak, "Gravitational Lensing Effect on Cosmic Microwave Background Anisotropies: A Power Spectrum Approach," *The Astrophysical Journal*, vol. 463, p. 1, May 1996.

[21] L. Knox and Y.-S. Song, "Limit on the detectability of the energy scale of inflation," *Phys. Rev. Lett.*, vol. 89, p. 011303, Jun 2002.

[22] S. Hanany and P. Rosenkranz, "Polarization of the atmosphere as a foreground for cosmic microwave background polarization experiments," *New Astronomy Reviews*, vol. 47, no. 11, pp. 1159 – 1165, 2003. Proceedings of the Workshop on The Cosmic Microwave Background Radiation and its Polarization.

[23] S. Spinelli, G. Fabbian, A. Tartari, M. Zannoni, and M. Gervasi, "A template of atmospheric o2 circularly polarized emission for cosmic microwave background experiments," *Monthly Notices of the Royal Astronomical Society*, vol. 414, no. 4, pp. 3272–3280, 2011.

[24] J. R. Pardo, J. Cernicharo, and E. Serabyn, "Atmospheric transmission at microwaves (atm): an improved model for millimeter/submillimeter applications," *IEEE Transactions on Antennas and Propagation*, vol. 49, pp. 1683–1694, Dec 2001.

[25] D. Samtleben, S. Staggs, and B. Winstein, "The cosmic microwave background for pedestrians: A review for particle and nuclear physicists," *Annual Review of Nuclear and Particle Science*, vol. 57, no. 1, pp. 245–283, 2007.

[26] P. A. R. Ade, N. Aghanim, Z. Ahmed, R. W. Aikin, K. D. Alexander, M. Arnaud, J. Aumont, C. Baccigalupi, A. J. Banday, D. Barkats, R. B. Barreiro, J. G. Bartlett, N. Bartolo, E. Battaner, K. Benabed, A. Benoît, A. Benoit-Lévy, S. J. Benton, J.-P. Bernard, M. Bersanelli, P. Bielewicz, C. A. Bischoff, J. J. Bock, A. Bonaldi, L. Bonavera, J. R. Bond, J. Borrill, F. R. Bouchet, F. Boulanger, J. A. Brevik, M. Bucher, I. Buder, E. Bullock, C. Burigana, R. C. Butler, V. Buza, E. Calabrese, J.-F. Cardoso, A. Catalano, A. Challinor,

R.-R. Chary, H. C. Chiang, P. R. Christensen, L. P. L. Colombo, C. Combet, J. Connors, F. Couchot, A. Coulais, B. P. Crill, A. Curto, F. Cuttaia, L. Danese, R. D. Davies, R. J. Davis, P. de Bernardis, A. de Rosa, G. de Zotti, J. Delabrouille, J.-M. Delouis, F.-X. Désert, C. Dickinson, J. M. Diego, H. Dole, S. Donzelli, O. Doré, M. Douspis, C. D. Dowell, L. Duband, A. Ducout, J. Dunkley, X. Dupac, C. Dvorkin, G. Efstathiou, F. Elsner, T. A. Enßlin, H. K. Eriksen, E. Falgarone, J. P. Filippini, F. Finelli, S. Fliescher, O. Forni, M. Frailis, A. A. Fraisse, E. Franceschi, A. Frejsel, S. Galeotta, S. Galli, K. Ganga, T. Ghosh, M. Giard, E. Gjerløw, S. R. Golwala, J. González-Nuevo, K. M. Górski, S. Gratton, A. Gregorio, A. Gruppuso, J. E. Gudmundsson, M. Halpern, F. K. Hansen, D. Hanson, D. L. Harrison, M. Hasselfield, G. Helou, S. Henrot-Versillé, D. Herranz, S. R. Hildebrandt, G. C. Hilton, E. Hivon, M. Hobson, W. A. Holmes, W. Hovest, V. V. Hristov, K. M. Huffenberger, H. Hui, G. Hurier, K. D. Irwin, A. H. Jaffe, T. R. Jaffe, J. Jewell, W. C. Jones, M. Juvela, A. Karakci, K. S. Karkare, J. P. Kaufman, B. G. Keating, S. Kefeli, E. Keihänen, S. A. Kernasovskiy, R. Keskitalo, T. S. Kisner, R. Kneissl, J. Knoche, L. Knox, J. M. Kovac, N. Krachmalnicoff, M. Kunz, C. L. Kuo, H. Kurki-Suonio, G. Lagache, A. Lähteenmäki, J.-M. Lamarre, A. Lasenby, M. Lattanzi, C. R. Lawrence, E. M. Leitch, R. Leonardi, F. Levrier, A. Lewis, M. Liguori, P. B. Lilje, M. Linden-Vørnle, M. López-Caniego, P. M. Lubin, M. Lueker, J. F. Macías-Pérez, B. Maffei, D. Maino, N. Mandolesi, A. Mangilli, M. Maris, P. G. Martin, E. Martínez-González, S. Masi, P. Mason, S. Matarrese, K. G. Megerian, P. R. Meinhold, A. Melchiorri, L. Mendes, A. Mennella, M. Migliaccio, S. Mitra, M.-A. Miville-Deschênes, A. Moneti, L. Montier, G. Morgante, D. Mortlock, A. Moss, D. Munshi, J. A. Murphy, P. Naselsky, F. Nati, P. Natoli, C. B. Netterfield, H. T. Nguyen, H. U. Nørgaard-Nielsen, F. Noviello, D. Novikov, I. Novikov, R. O'Brient, R. W. Ogburn, A. Orlando, L. Pagano, F. Pajot, R. Paladini, D. Paoletti, B. Partridge, F. Pasian, G. Patanchon, T. J. Pearson, O. Perdereau, L. Perotto, V. Pettorino, F. Piacentini, M. Piat, D. Pietrobon, S. Plaszczynski, E. Pointecouteau, G. Polenta, N. Ponthieu, G. W. Pratt, S. Prunet, C. Pryke, J.-L. Puget, J. P. Rachen, W. T. Reach, R. Rebolo, M. Reinecke, M. Remazeilles, C. Renault, A. Renzi, S. Richter, I. Ristorcelli, G. Rocha, M. Rossetti, G. Roudier, M. Rowan-Robinson, J. A. Rubiño Martín, B. Rusholme, M. Sandri, D. Santos, M. Savelainen, G. Savini, R. Schwarz, D. Scott, M. D. Seiffert, C. D. Sheehy, L. D. Spencer, Z. K. Staniszewski, V. Stolyarov, R. Sudiwala, R. Sunyaev, D. Sutton, A.-S. Suur-Uski, J.-F. Sygnet, J. A. Tauber, G. P. Teply, L. Terenzi, K. L. Thompson, L. Toffolatti, J. E. Tolan, M. Tomasi, M. Tristram, M. Tucci, A. D. Turner, L. Valenziano, J. Valiviita, B. Van Tent, L. Vibert,

P. Vielva, A. G. Vieregg, F. Villa, L. A. Wade, B. D. Wandelt, R. Watson, A. C. Weber, I. K. Wehus, M. White, S. D. M. White, J. Willmert, C. L. Wong, K. W. Yoon, D. Yvon, A. Zacchei, and A. Zonca, "Joint analysis of bicep2/keck array and planck data," *Phys. Rev. Lett.*, vol. 114, p. 101301, Mar 2015.

[27] Planck Collaboration, Adam, R., Ade, P. A. R., Aghanim, N., Arnaud, M., Aumont, J., Baccigalupi, C., Banday, A. J., Barreiro, R. B., Bartlett, J. G., Bartolo, N., Battaner, E., Benabed, K., Benoit-Lévy, A., Bernard, J.-P., Bersanelli, M., Bielewicz, P., Bonaldi, A., Bonavera, L., Bond, J. R., Borrill, J., Bouchet, F. R., Boulanger, F., Bracco, A., Bucher, M., Burigana, C., Butler, R. C., Calabrese, E., Cardoso, J.-F., Catalano, A., Challinor, A., Chamballu, A., Chary, R.-R., Chiang, H. C., Christensen, P. R., Clements, D. L., Colombi, S., Colombo, L. P. L., Combet, C., Couchot, F., Coulais, A., Crill, B. P., Curto, A., Cuttaia, F., Danese, L., Davies, R. D., Davis, R. J., de Bernardis, P., de Zotti, G., Delabrouille, J., Delouis, J.-M., Désert, F.-X., Dickinson, C., Diego, J. M., Dolag, K., Dole, H., Donzelli, S., Doré, O., Douspis, M., Ducout, A., Dunkley, J., Dupac, X., Efstathiou, G., Elsner, F., EnSSlin, T. A., Eriksen, H. K., Falgarone, E., Finelli, F., Forni, O., Frailis, M., Fraisse, A. A., Franceschi, E., Frejsel, A., Galeotta, S., Galli, S., Ganga, K., Ghosh, T., Giard, M., Giraud-Héraud, Y., Gjerløw, E., González-Nuevo, J., Górski, K. M., Gratton, S., Gregorio, A., Gruppuso, A., Guillet, V., Hansen, F. K., Hanson, D., Harrison, D. L., Helou, G., Henrot-Versillé, S., Hernández-Monteagudo, C., Herranz, D., Hivon, E., Hobson, M., Holmes, W. A., Huffenberger, K. M., Hurier, G., Jaffe, A. H., Jaffe, T. R., Jewell, J., Jones, W. C., Juvela, M., Keihänen, E., Keskitalo, R., Kisner, T. S., Kneissl, R., Knoche, J., Knox, L., Krachmalnicoff, N., Kunz, M., Kurki-Suonio, H., Lagache, G., Lamarre, J.-M., Lasenby, A., Lattanzi, M., Lawrence, C. R., Leahy, J. P., Leonardi, R., Lesgourgues, J., Levrier, F., Liguori, M., Lilje, P. B., Linden-Vørnle, M., López-Caniego, M., Lubin, P. M., Macías-Pérez, J. F., Maffei, B., Maino, D., Mandolesi, N., Mangilli, A., Maris, M., Martin, P. G., Martínez-González, E., Masi, S., Matarrese, S., Mazzotta, P., Meinhold, P. R., Melchiorri, A., Mendes, L., Mennella, A., Migliaccio, M., Mitra, S., Miville-Deschênes, M.-A., Moneti, A., Montier, L., Morgante, G., Mortlock, D., Moss, A., Munshi, D., Murphy, J. A., Naselsky, P., Nati, F., Natoli, P., Netterfield, C. B., Nørgaard-Nielsen, H. U., Noviello, F., Novikov, D., Novikov, I., Pagano, L., Pajot, F., Paladini, R., Paoletti, D., Partridge, B., Pasian, F., Patanchon, G., Pearson, T. J., Perdereau, O., Perotto, L., Perrotta, F., Pettorino, V., Piacentini, F., Piat, M., Pierpaoli, E., Pietrobon, D., Plaszczynski, S., Pointecouteau, E., Polenta, G., Ponthieu, N., Popa, L., Pratt, G. W., Prunet, S., Puget, J.-L.,

Rachen, J. P., Reach, W. T., Rebolo, R., Remazeilles, M., Renault, C., Renzi, A., Ricciardi, S., Ristorcelli, I., Rocha, G., Rosset, C., Rossetti, M., Roudier, G., Rouillé d?Orfeuil, B., Rubiño-Martín, J. A., Rusholme, B., Sandri, M., Santos, D., Savelainen, M., Savini, G., Scott, D., Soler, J. D., Spencer, L. D., Stolyarov, V., Stompor, R., Sudiwala, R., Sunyaev, R., Sutton, D., Suur-Uski, A.-S., Sygnet, J.-F., Tauber, J. A., Terenzi, L., Toffolatti, L., Tomasi, M., Tristram, M., Tucci, M., Tuovinen, J., Valenziano, L., Valiviita, J., Van Tent, B., Vibert, L., Vielva, P., Villa, F., Wade, L. A., Wandelt, B. D., Watson, R., Wehus, I. K., White, M., White, S. D. M., Yvon, D., Zacchei, A., and Zonca, A., "Planck intermediate results - xxx. the angular power spectrum of polarized dust emission at intermediate and high galactic latitudes," *A&A*, vol. 586, p. A133, 2016.

[28] N. Stebor, P. Ade, Y. Akiba, C. Aleman, K. Arnold, C. Baccigalupi, B. Barch, D. Barron, S. Beckman, A. Bender, D. Boettger, J. Borrill, S. Chapman, Y. Chinone, A. Cukierman, T. de Haan, M. Dobbs, A. Ducout, R. Dunner, T. Elleflot, J. Errard, G. Fabbian, S. Feeney, C. Feng, T. Fujino, G. Fuller, A. J. Gilbert, N. Goeckner-Wald, J. Groh, G. Hall, N. Halverson, T. Hamada, M. Hasegawa, K. Hattori, M. Hazumi, C. Hill, W. L. Holzapfel, Y. Hori, L. Howe, Y. Inoue, F. Irie, G. Jaehnig, A. Jaffe, O. Jeong, N. Katayama, J. P. Kaufman, K. Kazemzadeh, B. G. Keating, Z. Kermish, R. Keskitalo, T. Kisner, A. Kusaka, M. Le Jeune, A. T. Lee, D. Leon, E. V. Linder, L. Lowry, F. Matsuda, T. Matsumura, N. Miller, J. Montgomery, M. Navaroli, H. Nishino, H. Paar, J. Peloton, D. Poletti, G. Puglisi, C. R. Raum, G. M. Rebeiz, C. L. Reichardt, P. L. Richards, C. Ross, K. M. Rotermund, Y. Segawa, B. D. Sherwin, I. Shirley, P. Siritanasak, L. Steinmetz, R. Stompor, A. Suzuki, O. Tajima, S. Takada, S. Takatori, G. P. Teply, A. Tikhomirov, T. Tomaru, B. Westbrook, N. Whitehorn, A. Zahn, and O. Zahn, "The simons array cmb polarization experiment," 2016.

[29] B. A. Benson, P. A. R. Ade, Z. Ahmed, S. W. Allen, K. Arnold, J. E. Austermann, A. N. Bender, L. E. Bleem, J. E. Carlstrom, C. L. Chang, H. M. Cho, J. F. Cliche, T. M. Crawford, A. Cukierman, T. de Haan, M. A. Dobbs, D. Dutcher, W. Everett, A. Gilbert, N. W. Halverson, D. Hanson, N. L. Harrington, K. Hattori, J. W. Henning, G. C. Hilton, G. P. Holder, W. L. Holzapfel, K. D. Irwin, R. Keisler, L. Knox, D. Kubik, C. L. Kuo, A. T. Lee, E. M. Leitch, D. Li, M. McDonald, S. S. Meyer, J. Montgomery, M. Myers, T. Natoli, H. Nguyen, V. Novosad, S. Padin, Z. Pan, J. Pearson, C. Reichardt, J. E. Ruhl, B. R. Saliwanchik, G. Simard, G. Smecher, J. T. Sayre, E. Shirokoff, A. A. Stark,

K. Story, A. Suzuki, K. L. Thompson, C. Tucker, K. Vanderlinde, J. D. Vieira, A. Vikhlinin, G. Wang, V. Yefremenko, and K. W. Yoon, "Spt-3g: a next-generation cosmic microwave background polarization experiment on the south pole telescope," 2014.

[30] S. W. Henderson, R. Allison, J. Austermann, T. Baildon, N. Battaglia, J. A. Beall, D. Becker, F. De Bernardis, J. R. Bond, E. Calabrese, S. K. Choi, K. P. Coughlin, K. T. Crowley, R. Datta, M. J. Devlin, S. M. Duff, J. Dunkley, R. Dünner, A. van Engelen, P. A. Gallardo, E. Grace, M. Hasselfield, F. Hills, G. C. Hilton, A. D. Hincks, R. Hlo?ek, S. P. Ho, J. Hubmayr, K. Huffenberger, J. P. Hughes, K. D. Irwin, B. J. Koopman, A. B. Kosowsky, D. Li, J. McMahon, C. Munson, F. Nati, L. Newburgh, M. D. Niemack, P. Niraula, L. A. Page, C. G. Pappas, M. Salatino, A. Schillaci, B. L. Schmitt, N. Sehgal, B. D. Sherwin, J. L. Sievers, S. M. Simon, D. N. Spergel, S. T. Staggs, J. R. Stevens, R. Thornton, J. Van Lanen, E. M. Vavagiakis, J. T. Ward, and E. J. Wollack, "Advanced actpol cryogenic detector arrays and readout," *Journal of Low Temperature Physics*, vol. 184, pp. 772–779, Aug 2016.

[31] Z. D. Kermish, P. Ade, A. Anthony, K. Arnold, D. Barron, D. Boettger, J. Borrill, S. Chapman, Y. Chinone, M. A. Dobbs, J. Errard, G. Fabbian, D. Flanigan, G. Fuller, A. Ghribi, W. Grainger, N. Halverson, M. Hasegawa, K. Hattori, M. Hazumi, W. L. Holzapfel, J. Howard, P. Hyland, A. Jaffe, B. Keating, T. Kisner, A. T. Lee, M. Le Jeune, E. Linder, M. Lungu, F. Matsuda, T. Matsumura, X. Meng, N. J. Miller, H. Morii, S. Moyerman, M. J. Myers, H. Nishino, H. Paar, E. Quealy, C. L. Reichardt, P. L. Richards, C. Ross, A. Shimizu, M. Shimon, C. Shimmin, M. Sholl, P. Siritanasak, H. Spieler, N. Stebor, B. Steinbach, R. Stompor, A. Suzuki, T. Tomaru, C. Tucker, and O. Zahn, "The polarbear experiment," 2012.

[32] D. Hanson, S. Hoover, A. Crites, P. A. R. Ade, K. A. Aird, J. E. Austermann, J. A. Beall, A. N. Bender, B. A. Benson, L. E. Bleem, J. J. Bock, J. E. Carlstrom, C. L. Chang, H. C. Chiang, H.-M. Cho, A. Conley, T. M. Crawford, T. de Haan, M. A. Dobbs, W. Everett, J. Gallicchio, J. Gao, E. M. George, N. W. Halverson, N. Harrington, J. W. Henning, G. C. Hilton, G. P. Holder, W. L. Holzapfel, J. D. Hrubes, N. Huang, J. Hubmayr, K. D. Irwin, R. Keisler, L. Knox, A. T. Lee, E. Leitch, D. Li, C. Liang, D. Luong-Van, G. Marsden, J. J. McMahon, J. Mehl, S. S. Meyer, L. Mocanu, T. E. Montroy, T. Natoli, J. P. Nibarger, V. Novosad, S. Padin, C. Pryke, C. L. Reichardt, J. E. Ruhl, B. R. Saliwanchik, J. T. Sayre, K. K. Schaffer, B. Schulz, G. Smecher, A. A. Stark, K. T. Story, C. Tucker,

K. Vanderlinde, J. D. Vieira, M. P. Viero, G. Wang, V. Yefremenko, O. Zahn, and M. Zemcov, "Detection of b-mode polarization in the cosmic microwave background with data from the south pole telescope," *Phys. Rev. Lett.*, vol. 111, p. 141301, Sep 2013.

[33] Planck Collaboration, Ade, P. A. R., Aghanim, N., Arnaud, M., Ashdown, M., Aumont, J., Baccigalupi, C., Banday, A. J., Barreiro, R. B., Bartlett, J. G., Bartolo, N., Basak, S., Battaner, E., Benabed, K., Benoît, A., Benoit-Lévy, A., Bernard, J.-P., Bersanelli, M., Bielewicz, P., Bock, J. J., Bonaldi, A., Bonavera, L., Bond, J. R., Borrill, J., Bouchet, F. R., Boulanger, F., Bucher, M., Burigana, C., Butler, R. C., Calabrese, E., Cardoso, J.-F., Catalano, A., Challinor, A., Chamballu, A., Chiang, H. C., Christensen, P. R., Church, S., Clements, D. L., Colombi, S., Colombo, L. P. L., Combet, C., Couchot, F., Coulais, A., Crill, B. P., Curto, A., Cuttaia, F., Danese, L., Davies, R. D., Davis, R. J., de Bernardis, P., de Rosa, A., de Zotti, G., Delabrouille, J., Désert, F.-X., Diego, J. M., Dole, H., Donzelli, S., Doré, O., Douspis, M., Ducout, A., Dunkley, J., Dupac, X., Efstathiou, G., Elsner, F., EnSSlin, T. A., Eriksen, H. K., Fergusson, J., Finelli, F., Forni, O., Frailis, M., Fraisse, A. A., Franceschi, E., Frejsel, A., Galeotta, S., Galli, S., Ganga, K., Giard, M., Giraud-Héraud, Y., Gjerløw, E., González-Nuevo, J., Górski, K. M., Gratton, S., Gregorio, A., Gruppuso, A., Gudmundsson, J. E., Hansen, F. K., Hanson, D., Harrison, D. L., Henrot-Versillé, S., Hernández-Monteagudo, C., Herranz, D., Hildebrandt, S. R., Hivon, E., Hobson, M., Holmes, W. A., Hornstrup, A., Hovest, W., Huffenberger, K. M., Hurier, G., Jaffe, A. H., Jaffe, T. R., Jones, W. C., Juvela, M., Keihänen, E., Keskitalo, R., Kisner, T. S., Kneissl, R., Knoche, J., Kunz, M., Kurki-Suonio, H., Lagache, G., Lähteenmäki, A., Lamarre, J.-M., Lasenby, A., Lattanzi, M., Lawrence, C. R., Leonardi, R., Lesgourgues, J., Levrier, F., Lewis, A., Liguori, M., Lilje, P. B., Linden-Vørnle, M., López-Caniego, M., Lubin, P. M., Macías-Pérez, J. F., Maggio, G., Maino, D., Mandolesi, N., Mangilli, A., Maris, M., Martin, P. G., Martínez-González, E., Masi, S., Matarrese, S., McGehee, P., Meinhold, P. R., Melchiorri, A., Mendes, L., Mennella, A., Migliaccio, M., Mitra, S., Miville-Deschênes, M.-A., Moneti, A., Montier, L., Morgante, G., Mortlock, D., Moss, A., Munshi, D., Murphy, J. A., Naselsky, P., Nati, F., Natoli, P., Netterfield, C. B., Nørgaard-Nielsen, H. U., Noviello, F., Novikov, D., Novikov, I., Oxborrow, C. A., Paci, F., Pagano, L., Pajot, F., Paoletti, D., Pasian, F., Patanchon, G., Perdereau, O., Perotto, L., Perrotta, F., Pettorino, V., Piacentini, F., Piat, M., Pierpaoli, E., Pietrobon, D., Plaszczynski, S., Pointecouteau, E., Polenta, G., Popa, L., Pratt, G. W., Prézeau, G., Prunet, S., Puget, J.-L.,

Rachen, J. P., Reach, W. T., Rebolo, R., Reinecke, M., Remazeilles, M., Renault, C., Renzi, A., Ristorcelli, I., Rocha, G., Rosset, C., Rossetti, M., Roudier, G., Rowan-Robinson, M., Rubiño-Martín, J. A., Rusholme, B., Sandri, M., Santos, D., Savelainen, M., Savini, G., Scott, D., Seiffert, M. D., Shellard, E. P. S., Spencer, L. D., Stolyarov, V., Stompor, R., Sudiwala, R., Sunyaev, R., Sutton, D., Suur-Uski, A.-S., Sygnet, J.-F., Tauber, J. A., Terenzi, L., Toffolatti, L., Tomasi, M., Tristram, M., Tucci, M., Tuovinen, J., Valenziano, L., Valiviita, J., Van Tent, B., Vielva, P., Villa, F., Wade, L. A., Wandelt, B. D., Wehus, I. K., White, M., Yvon, D., Zacchei, A., and Zonca, A., "Planck 2015 results - xv. gravitational lensing," *A&A*, vol. 594, p. A15, 2016.

[34] R. Keisler, S. Hoover, N. Harrington, J. W. Henning, P. A. R. Ade, K. A. Aird, J. E. Austermann, J. A. Beall, A. N. Bender, B. A. Benson, L. E. Bleem, J. E. Carlstrom, C. L. Chang, H. C. Chiang, H.-M. Cho, R. Citron, T. M. Crawford, A. T. Crites, T. de Haan, M. A. Dobbs, W. Everett, J. Gallicchio, J. Gao, E. M. George, A. Gilbert, N. W. Halverson, D. Hanson, G. C. Hilton, G. P. Holder, W. L. Holzapfel, Z. Hou, J. D. Hrubes, N. Huang, J. Hubmayr, K. D. Irwin, L. Knox, A. T. Lee, E. M. Leitch, D. Li, D. Luong-Van, D. P. Marrone, J. J. McMahon, J. Mehl, S. S. Meyer, L. Mocanu, T. Natoli, J. P. Nibarger, V. Novosad, S. Padin, C. Pryke, C. L. Reichardt, J. E. Ruhl, B. R. Saliwanchik, J. T. Sayre, K. K. Schaffer, E. Shirokoff, G. Smecher, A. A. Stark, K. T. Story, C. Tucker, K. Vanderlinde, J. D. Vieira, G. Wang, N. Whitehorn, V. Yefremenko, and O. Zahn, "Measurements of sub-degree b-mode polarization in the cosmic microwave background from 100 square degrees of sptpol data," *The Astrophysical Journal*, vol. 807, no. 2, p. 151, 2015.

[35] T. P. C. P. A. R. Ade, Y. Akiba, A. E. Anthony, K. Arnold, M. Atlas, D. Barron, D. Boettger, J. Borrill, S. Chapman, Y. Chinone, M. Dobbs, T. Elleflot, J. Errard, G. Fabbian, C. Feng, D. Flanigan, A. Gilbert, W. Grainger, N. W. Halverson, M. Hasegawa, K. Hattori, M. Hazumi, W. L. Holzapfel, Y. Hori, J. Howard, P. Hyland, Y. Inoue, G. C. Jaehnig, A. H. Jaffe, B. Keating, Z. Kermish, R. Keskitalo, T. Kisner, M. L. Jeune, A. T. Lee, E. M. Leitch, E. Linder, M. Lungu, F. Matsuda, T. Matsumura, X. Meng, N. J. Miller, H. Morii, S. Moyerman, M. J. Myers, M. Navaroli, H. Nishino, A. Orlando, H. Paar, J. Peloton, D. Poletti, E. Quealy, G. Rebeiz, C. L. Reichardt, P. L. Richards, C. Ross, I. Schanning, D. E. Schenck, B. D. Sherwin, A. Shimizu, C. Shimmin, M. Shimon, P. Siritanasak, G. Smecher, H. Spieler, N. Stebor, B. Steinbach, R. Stompor, A. Suzuki, S. Takakura, T. Tomaru, B. Wilson, A. Yadav, and O. Zahn, "A measurement of the cosmic microwave background b-mode polar-

ization power spectrum at sub-degree scales with polarbear," *The Astrophysical Journal*, vol. 794, no. 2, p. 171, 2014.

[36] K. Arnold, P. A. R. Ade, A. E. Anthony, D. Barron, D. Boettger, J. Borrill, S. Chapman, Y. Chinone, M. A. Dobbs, J. Errard, G. Fabbian, D. Flanigan, G. Fuller, A. Ghribi, W. Grainger, N. Halverson, M. Hasegawa, K. Hattori, M. Hazumi, W. L. Holzapfel, J. Howard, P. Hyland, A. Jaffe, B. Keating, Z. Kermish, T. Kisner, M. Le Jeune, A. T. Lee, E. Linder, M. Lungu, F. Matsuda, T. Matsumura, N. J. Miller, X. Meng, H. Morii, S. Moyerman, M. J. Myers, H. Nishino, H. Paar, E. Quealy, C. Reichardt, P. L. Richards, C. Ross, A. Shimizu, C. Shimmin, M. Shimon, M. Sholl, P. Siritanasak, H. Speiler, N. Stebor, B. Steinbach, R. Stompor, A. Suzuki, T. Tomaru, C. Tucker, and O. Zahn, "The bolometric focal plane array of the polarbear cmb experiment," 2012.

[37] G. M. Rebeiz, "Millimeter-wave and terahertz integrated circuit antennas," *Proceedings of the IEEE*, vol. 80, pp. 1748–1770, Nov 1992.

[38] D. Rutledge, D. Neikirk, and D. Kasilingam, *INTEGRATED-CIRCUIT ANTENNAS.*, vol. 10. Academic Press, 1983.

[39] A. Suzuki, K. Arnold, J. Edwards, G. Engargiola, A. Ghribi, W. Holzapfel, A. T. Lee, X. F. Meng, M. J. Myers, R. O'Brient, E. Quealy, G. Rebeiz, P. Richards, D. Rosen, and P. Siritanasak, "Multichroic dual-polarization bolometric detectors for studies of the cosmic microwave background," 2012.

[40] J. M. Edwards, R. O'Brient, A. T. Lee, and G. M. Rebeiz, "Dual-polarized sinuous antennas on extended hemispherical silicon lenses," *IEEE Transactions on Antennas and Propagation*, vol. 60, pp. 4082–4091, Sept 2012.

[41] G. Chattopadhyay and J. Zmuidzinas, "A dual-polarized slot antenna for millimeter waves," *IEEE Transactions on Antennas and Propagation*, vol. 46, pp. 736–737, May 1998.

[42] M. A. Dobbs, M. Lueker, K. A. Aird, A. N. Bender, B. A. Benson, L. E. Bleem, J. E. Carlstrom, C. L. Chang, H.-M. Cho, J. Clarke, T. M. Crawford, A. T. Crites, D. I. Flanigan, T. de Haan, E. M. George, N. W. Halverson, W. L. Holzapfel, J. D. Hrubes, B. R. Johnson, J. Joseph, R. Keisler, J. Kennedy, Z. Kermish, T. M. Lanting, A. T. Lee, E. M. Leitch, D. Luong-Van, J. J. McMahon, J. Mehl, S. S. Meyer, T. E. Montroy, S. Padin, T. Plagge, C. Pryke, P. L. Richards, J. E. Ruhl, K. K. Schaffer, D. Schwan, E. Shirokoff, H. G. Spieler, Z. Staniszewski, A. A. Stark, K. Vanderlinde, J. D. Vieira, C. Vu, B. Westbrook,

and R. Williamson, "Frequency multiplexed superconducting quantum interference device readout of large bolometer arrays for cosmic microwave background measurements," *Review of Scientific Instruments*, vol. 83, no. 7, p. 073113, 2012.

[43] P. A. R. Ade, Y. Akiba, A. E. Anthony, K. Arnold, M. Atlas, D. Barron, D. Boettger, J. Borrill, S. Chapman, Y. Chinone, M. Dobbs, T. Elleflot, J. Errard, G. Fabbian, C. Feng, D. Flanigan, A. Gilbert, W. Grainger, N. W. Halverson, M. Hasegawa, K. Hattori, M. Hazumi, W. L. Holzapfel, Y. Hori, J. Howard, P. Hyland, Y. Inoue, G. C. Jaehnig, A. Jaffe, B. Keating, Z. Kermish, R. Keskitalo, T. Kisner, M. Le Jeune, A. T. Lee, E. Linder, E. M. Leitch, M. Lungu, F. Matsuda, T. Matsumura, X. Meng, N. J. Miller, H. Morii, S. Moyerman, M. J. Myers, M. Navaroli, H. Nishino, H. Paar, J. Peloton, E. Quealy, G. Rebeiz, C. L. Reichardt, P. L. Richards, C. Ross, I. Schanning, D. E. Schenck, B. Sherwin, A. Shimizu, C. Shimmin, M. Shimon, P. Siritanasak, G. Smecher, H. Spieler, N. Stebor, B. Steinbach, R. Stompor, A. Suzuki, S. Takakura, T. Tomaru, B. Wilson, A. Yadav, and O. Zahn, "Measurement of the cosmic microwave background polarization lensing power spectrum with the polarbear experiment," *Phys. Rev. Lett.*, vol. 113, p. 021301, Jul 2014.

[44] P. A. R. Ade, Y. Akiba, A. E. Anthony, K. Arnold, M. Atlas, D. Barron, D. Boettger, J. Borrill, C. Borys, S. Chapman, Y. Chinone, M. Dobbs, T. Elleflot, J. Errard, G. Fabbian, C. Feng, D. Flanigan, A. Gilbert, W. Grainger, N. W. Halverson, M. Hasegawa, K. Hattori, M. Hazumi, W. L. Holzapfel, Y. Hori, J. Howard, P. Hyland, Y. Inoue, G. C. Jaehnig, A. Jaffe, B. Keating, Z. Kermish, R. Keskitalo, T. Kisner, M. Le Jeune, A. T. Lee, E. M. Leitch, E. Linder, M. Lungu, F. Matsuda, T. Matsumura, X. Meng, N. J. Miller, H. Morii, S. Moyerman, M. J. Myers, M. Navaroli, H. Nishino, H. Paar, J. Peloton, D. Poletti, E. Quealy, G. Rebeiz, C. L. Reichardt, P. L. Richards, C. Ross, K. Rotermund, I. Schanning, D. E. Schenck, B. D. Sherwin, A. Shimizu, C. Shimmin, M. Shimon, P. Siritanasak, G. Smecher, H. Spieler, N. Stebor, B. Steinbach, R. Stompor, A. Suzuki, S. Takakura, A. Tikhomirov, T. Tomaru, B. Wilson, A. Yadav, and O. Zahn, "Evidence for gravitational lensing of the cosmic microwave background polarization from cross-correlation with the cosmic infrared background," *Phys. Rev. Lett.*, vol. 112, p. 131302, Apr 2014.

[45] T. P. Collaboration, P. A. R. Ade, M. Aguilar, Y. Akiba, K. Arnold, C. Baccigalupi, D. Barron, D. Beck, F. Bianchini, D. Boettger, J. Borrill, S. Chapman, Y. Chinone, K. Crowley, A. Cukierman, R. Dünner, M. Dobbs, A. Ducout, T. Elleflot, J. Errard, G. Fabbian, S. M. Feeney, C. Feng, T. Fujino, N. Galitzki,

A. Gilbert, N. Goeckner-Wald, J. C. Groh, G. Hall, N. Halverson, T. Hamada, M. Hasegawa, M. Hazumi, C. A. Hill, L. Howe, Y. Inoue, G. Jaehnig, A. H. Jaffe, O. Jeong, D. Kaneko, N. Katayama, B. Keating, R. Keskitalo, T. Kisner, N. Krachmalnicoff, A. Kusaka, M. L. Jeune, A. T. Lee, E. M. Leitch, D. Leon, E. Linder, L. Lowry, F. Matsuda, T. Matsumura, Y. Minami, J. Montgomery, M. Navaroli, H. Nishino, H. Paar, J. Peloton, A. T. P. Pham, D. Poletti, G. Puglisi, C. L. Reichardt, P. L. Richards, C. Ross, Y. Segawa, B. D. Sherwin, M. Silva-Feaver, P. Siritanasak, N. Stebor, R. Stompor, A. Suzuki, O. Tajima, S. Takakura, S. Takatori, D. Tanabe, G. P. Teply, T. Tomaru, C. Tucker, N. Whitehorn, and A. Zahn, "A measurement of the cosmic microwave background b -mode polarization power spectrum at subdegree scales from two years of polarbear data," *The Astrophysical Journal*, vol. 848, no. 2, p. 121, 2017.

[46] Planck Collaboration, Ade, P. A. R., Aghanim, N., Alves, M. I. R., Armitage-Caplan, C., Arnaud, M., Ashdown, M., Atrio-Barandela, F., Aumont, J., Aussel, H., Baccigalupi, C., Banday, A. J., Barreiro, R. B., Barrena, R., Bartelmann, M., Bartlett, J. G., Bartolo, N., Basak, S., Battaner, E., Battye, R., Benabed, K., Benoît, A., Benoit-Lévy, A., Bernard, J.-P., Bersanelli, M., Bertincourt, B., Bethermin, M., Bielewicz, P., Bikmaev, I., Blanchard, A., Bobin, J., Bock, J. J., Böhringer, H., Bonaldi, A., Bonavera, L., Bond, J. R., Borrill, J., Bouchet, F. R., Boulanger, F., Bourdin, H., Bowyer, J. W., Bridges, M., Brown, M. L., Bucher, M., Burenin, R., Burigana, C., Butler, R. C., Calabrese, E., Cappellini, B., Cardoso, J.-F., Carr, R., Carvalho, P., Casale, M., Castex, G., Catalano, A., Challinor, A., Chamballu, A., Chary, R.-R., Chen, X., Chiang, H. C., Chiang, L.-Y, Chon, G., Christensen, P. R., Churazov, E., Church, S., Clemens, M., Clements, D. L., Colombi, S., Colombo, L. P. L., Combet, C., Comis, B., Couchot, F., Coulais, A., Crill, B. P., Cruz, M., Curto, A., Cuttaia, F., Da Silva, A., Dahle, H., Danese, L., Davies, R. D., Davis, R. J., de Bernardis, P., de Rosa, A., de Zotti, G., Déchelette, T., Delabrouille, J., Delouis, J.-M., Démoclès, J., Désert, F.-X., Dick, J., Dickinson, C., Diego, J. M., Dolag, K., Dole, H., Donzelli, S., Doré, O., Douspis, M., Ducout, A., Dunkley, J., Dupac, X., Efstathiou, G., Elsner, F., EnSSlin, T. A., Eriksen, H. K., Fabre, O., Falgarone, E., Falvella, M. C., Fantaye, Y., Fergusson, J., Filliard, C., Finelli, F., Flores-Cacho, I., Foley, S., Forni, O., Fosalba, P., Frailis, M., Fraisse, A. A., Franceschi, E., Freschi, M., Fromenteau, S., Frommert, M., Gaier, T. C., Galeotta, S., Gallegos, J., Galli, S., Gandolfo, B., Ganga, K., Gauthier, C., Génova-Santos, R. T., Ghosh, T., Giard, M., Giardino, G., Gilfanov, M., Girard, D., Giraud-Héraud, Y., Gjerløw, E., González-Nuevo, J., Górski, K. M., Gratton, S., Gregorio, A.,

Gruppuso, A., Gudmundsson, J. E., Haissinski, J., Hamann, J., Hansen, F. K., Hansen, M., Hanson, D., Harrison, D. L., Heavens, A., Helou, G., Hempel, A., Henrot-Versillé, S., Hernández-Monteagudo, C., Herranz, D., Hildebrandt, S. R., Hivon, E., Ho, S., Hobson, M., Holmes, W. A., Hornstrup, A., Hou, Z., Hovest, W., Huey, G., Huffenberger, K. M., Hurier, G., Ili?, S., Jaffe, A. H., Jaffe, T. R., Jasche, J., Jewell, J., Jones, W. C., Juvela, M., Kalberla, P., Kangaslahti, P., Keihänen, E., Kerp, J., Keskitalo, R., Khamitov, I., Kiiveri, K., Kim, J., Kisner, T. S., Kneissl, R., Knoche, J., Knox, L., Kunz, M., Kurki-Suonio, H., Lacasa, F., Lagache, G., Lähteenmäki, A., Lamarre, J.-M., Langer, M., Lasenby, A., Lattanzi, M., Laureijs, R. J., Lavabre, A., Lawrence, C. R., Le Jeune, M., Leach, S., Leahy, J. P., Leonardi, R., León-Tavares, J., Leroy, C., Lesgourgues, J., Lewis, A., Li, C., Liddle, A., Liguori, M., Lilje, P. B., Linden-Vørnle, M., Lindholm, V., López-Caniego, M., Lowe, S., Lubin, P. M., Macías-Pérez, J. F., MacTavish, C. J., Maffei, B., Maggio, G., Maino, D., Mandolesi, N., Mangilli, A., Marcos-Caballero, A., Marinucci, D., Maris, M., Marleau, F., Marshall, D. J., Martin, P. G., Martínez-González, E., Masi, S., Massardi, M., Matarrese, S., Matsumura, T., Matthai, F., Maurin, L., Mazzotta, P., McDonald, A., McEwen, J. D., McGehee, P., Mei, S., Meinhold, P. R., Melchiorri, A., Melin, J.-B., Mendes, L., Menegoni, E., Mennella, A., Migliaccio, M., Mikkelsen, K., Millea, M., Miniscalco, R., Mitra, S., Miville-Deschênes, M.-A., Molinari, D., Moneti, A., Montier, L., Morgante, G., Morisset, N., Mortlock, D., Moss, A., Munshi, D., Murphy, J. A., Naselsky, P., Nati, F., Natoli, P., Negrello, M., Nesvadba, N. P. H., Netterfield, C. B., Nørgaard-Nielsen, H. U., North, C., Noviello, F., Novikov, D., Novikov, I., O?Dwyer, I. J., Orieux, F., Osborne, S., O?Sullivan, C., Oxborrow, C. A., Paci, F., Pagano, L., Pajot, F., Paladini, R., Pandolfi, S., Paoletti, D., Partridge, B., Pasian, F., Patanchon, G., Paykari, P., Pearson, D., Pearson, T. J., Peel, M., Peiris, H. V., Perdereau, O., Perotto, L., Perrotta, F., Pettorino, V., Piacentini, F., Piat, M., Pierpaoli, E., Pietrobon, D., Plaszczynski, S., Platania, P., Pogosyan, D., Pointecouteau, E., Polenta, G., Ponthieu, N., Popa, L., Poutanen, T., Pratt, G. W., Prézeau, G., Prunet, S., Puget, J.-L., Pullen, A. R., Rachen, J. P., Racine, B., Rahlin, A., Räth, C., Reach, W. T., Rebolo, R., Reinecke, M., Remazeilles, M., Renault, C., Renzi, A., Riazuelo, A., Ricciardi, S., Riller, T., Ringeval, C., Ristorcelli, I., Robbers, G., Rocha, G., Roman, M., Rosset, C., Rossetti, M., Roudier, G., Rowan-Robinson, M., Rubiño-Martín, J. A., Ruiz-Granados, B., Rusholme, B., Salerno, E., Sandri, M., Sanselme, L., Santos, D., Savelainen, M., Savini, G., Schaefer, B. M., Schiavon, F., Scott, D., Seiffert, M. D., Serra, P., Shellard, E. P. S., Smith, K., Smoot, G. F., Souradeep, T., Spencer, L. D., Starck, J.-L.,

Stolyarov, V., Stompor, R., Sudiwala, R., Sunyaev, R., Sureau, F., Sutter, P., Sutton, D., Suur-Uski, A.-S., Sygnet, J.-F., Tauber, J. A., Tavagnacco, D., Taylor, D., Terenzi, L., Texier, D., Toffolatti, L., Tomasi, M., Torre, J.-P., Tristram, M., Tucci, M., Tuovinen, J., Türler, M., Tuttlebee, M., Umana, G., Valenziano, L., Valiviita, J., Van Tent, B., Varis, J., Vibert, L., Viel, M., Vielva, P., Villa, F., Vittorio, N., Wade, L. A., Wandelt, B. D., Watson, C., Watson, R., Wehus, I. K., Welikala, N., Weller, J., White, M., White, S. D. M., Wilkinson, A., Winkel, B., Xia, J.-Q., Yvon, D., Zacchei, A., Zibin, J. P., and Zonca, A., "Planck 2013 results. i. overview of products and scientific results," *A&A*, vol. 571, p. A1, 2014.

[47] Planck Collaboration:, Ade, P. A. R., Alves, M. I. R., Aniano, G., Armitage-Caplan, C., Arnaud, M., Atrio-Barandela, F., Aumont, J., Baccigalupi, C., Banday, A. J., Barreiro, R. B., Battaner, E., Benabed, K., Benoit-Lévy, A., Bernard, J.-P., Bersanelli, M., Bielewicz, P., Bock, J. J., Bond, J. R., Borrill, J., Bouchet, F. R., Boulanger, F., Burigana, C., Cardoso, J.-F., Catalano, A., Chamballu, A., Chiang, H. C., Colombo, L. P. L., Combet, C., Couchot, F., Coulais, A., Crill, B. P., Curto, A., Cuttaia, F., Danese, L., Davies, R. D., Davis, R. J., de Bernardis, P., de Zotti, G., Delabrouille, J., Désert, F.-X., Dickinson, C., Diego, J. M., Donzelli, S., Doré, O., Douspis, M., Dunkley, J., Dupac, X., EnSSlin, T. A., Eriksen, H. K., Falgarone, E., Finelli, F., Forni, O., Frailis, M., Fraisse, A. A., Franceschi, E., Galeotta, S., Ganga, K., Ghosh, T., Giard, M., González-Nuevo, J., Górski, K. M., Gregorio, A., Gruppuso, A., Guillet, V., Hansen, F. K., Harrison, D. L., Helou, G., Hernández-Monteagudo, C., Hildebrandt, S. R., Hivon, E., Hobson, M., Holmes, W. A., Hornstrup, A., Jaffe, A. H., Jaffe, T. R., Jones, W. C., Keihänen, E., Keskitalo, R., Kisner, T. S., Kneissl, R., Knoche, J., Kunz, M., Kurki-Suonio, H., Lagache, G., Lamarre, J.-M., Lasenby, A., Lawrence, C. R., Leahy, J. P., Leonardi, R., Levrier, F., Liguori, M., Lilje, P. B., Linden-Vørnle, M., López-Caniego, M., Lubin, P. M., Macías-Pérez, J. F., Maffei, B., Magalhães, A. M., Maino, D., Mandolesi, N., Maris, M., Marshall, D. J., Martin, P. G., Martínez-González, E., Masi, S., Matarrese, S., Mazzotta, P., Melchiorri, A., Mendes, L., Mennella, A., Migliaccio, M., Miville-Deschênes, M.-A., Moneti, A., Montier, L., Morgante, G., Mortlock, D., Munshi, D., Murphy, J. A., Naselsky, P., Nati, F., Natoli, P., Netterfield, C. B., Noviello, F., Novikov, D., Novikov, I., Oppermann, N., Oxborrow, C. A., Pagano, L., Pajot, F., Paoletti, D., Pasian, F., Perdereau, O., Perotto, L., Perrotta, F., Piacentini, F., Pietrobon, D., Plaszczynski, S., Pointecouteau, E., Polenta, G., Popa, L., Pratt, G. W., Rachen, J. P., Reach, W. T., Reinecke,

M., Remazeilles, M., Renault, C., Ricciardi, S., Riller, T., Ristorcelli, I., Rocha, G., Rosset, C., Roudier, G., Rubiño-Martín, J. A., Rusholme, B., Salerno, E., Sandri, M., Savini, G., Scott, D., Spencer, L. D., Stolyarov, V., Stompor, R., Sudiwala, R., Sutton, D., Suur-Uski, A.-S., Sygnet, J.-F., Tauber, J. A., Terenzi, L., Toffolatti, L., Tomasi, M., Tristram, M., Tucci, M., Valenziano, L., Valiviita, J., Van Tent, B., Vielva, P., Villa, F., Wandelt, B. D., Zacchei, A., and Zonca, A., "Planck intermediate results. xxii. frequency dependence of thermal emission from galactic dust in intensity and polarization," *A&A*, vol. 576, p. A107, 2015.

[48] Planck Collaboration, Adam, R., Ade, P. A. R., Aghanim, N., Arnaud, M., Aumont, J., Baccigalupi, C., Banday, A. J., Barreiro, R. B., Bartlett, J. G., Bartolo, N., Battaner, E., Benabed, K., Benoit-Lévy, A., Bernard, J.-P., Bersanelli, M., Bielewicz, P., Bonaldi, A., Bonavera, L., Bond, J. R., Borrill, J., Bouchet, F. R., Boulanger, F., Bracco, A., Bucher, M., Burigana, C., Butler, R. C., Calabrese, E., Cardoso, J.-F., Catalano, A., Challinor, A., Chamballu, A., Chary, R.-R., Chiang, H. C., Christensen, P. R., Clements, D. L., Colombi, S., Colombo, L. P. L., Combet, C., Couchot, F., Coulais, A., Crill, B. P., Curto, A., Cuttaia, F., Danese, L., Davies, R. D., Davis, R. J., de Bernardis, P., de Zotti, G., Delabrouille, J., Delouis, J.-M., Désert, F.-X., Dickinson, C., Diego, J. M., Dolag, K., Dole, H., Donzelli, S., Doré, O., Douspis, M., Ducout, A., Dunkley, J., Dupac, X., Efstathiou, G., Elsner, F., EnSSlin, T. A., Eriksen, H. K., Falgarone, E., Finelli, F., Forni, O., Frailis, M., Fraisse, A. A., Franceschi, E., Frejsel, A., Galeotta, S., Galli, S., Ganga, K., Ghosh, T., Giard, M., Giraud-Héraud, Y., Gjerløw, E., González-Nuevo, J., Górski, K. M., Gratton, S., Gregorio, A., Gruppuso, A., Guillet, V., Hansen, F. K., Hanson, D., Harrison, D. L., Helou, G., Henrot-Versillé, S., Hernández-Monteagudo, C., Herranz, D., Hivon, E., Hobson, M., Holmes, W. A., Huffenberger, K. M., Hurier, G., Jaffe, A. H., Jaffe, T. R., Jewell, J., Jones, W. C., Juvela, M., Keihänen, E., Keskitalo, R., Kisner, T. S., Kneissl, R., Knoche, J., Knox, L., Krachmalnicoff, N., Kunz, M., Kurki-Suonio, H., Lagache, G., Lamarre, J.-M., Lasenby, A., Lattanzi, M., Lawrence, C. R., Leahy, J. P., Leonardi, R., Lesgourgues, J., Levrier, F., Liguori, M., Lilje, P. B., Linden-Vørnle, M., López-Caniego, M., Lubin, P. M., Macías-Pérez, J. F., Maffei, B., Maino, D., Mandolesi, N., Mangilli, A., Maris, M., Martin, P. G., Martínez-González, E., Masi, S., Matarrese, S., Mazzotta, P., Meinhold, P. R., Melchiorri, A., Mendes, L., Mennella, A., Migliaccio, M., Mitra, S., Miville-Deschênes, M.-A., Moneti, A., Montier, L., Morgante, G., Mortlock, D., Moss, A., Munshi, D., Murphy, J. A., Naselsky, P., Nati, F., Natoli, P., Netterfield, C. B., Nørgaard-Nielsen, H. U., Noviello, F., Novikov, D., Novikov, I., Pagano, L.,

Pajot, F., Paladini, R., Paoletti, D., Partridge, B., Pasian, F., Patanchon, G., Pearson, T. J., Perdereau, O., Perotto, L., Perrotta, F., Pettorino, V., Piacentini, F., Piat, M., Pierpaoli, E., Pietrobon, D., Plaszczynski, S., Pointecouteau, E., Polenta, G., Ponthieu, N., Popa, L., Pratt, G. W., Prunet, S., Puget, J.-L., Rachen, J. P., Reach, W. T., Rebolo, R., Remazeilles, M., Renault, C., Renzi, A., Ricciardi, S., Ristorcelli, I., Rocha, G., Rosset, C., Rossetti, M., Roudier, G., Rouillé d?Orfeuil, B., Rubiño-Martín, J. A., Rusholme, B., Sandri, M., Santos, D., Savelainen, M., Savini, G., Scott, D., Soler, J. D., Spencer, L. D., Stolyarov, V., Stompor, R., Sudiwala, R., Sunyaev, R., Sutton, D., Suur-Uski, A.-S., Sygnet, J.-F., Tauber, J. A., Terenzi, L., Toffolatti, L., Tomasi, M., Tristram, M., Tucci, M., Tuovinen, J., Valenziano, L., Valiviita, J., Van Tent, B., Vibert, L., Vielva, P., Villa, F., Wade, L. A., Wandelt, B. D., Watson, R., Wehus, I. K., White, M., White, S. D. M., Yvon, D., Zacchei, A., and Zonca, A., "Planck intermediate results - xxx. the angular power spectrum of polarized dust emission at intermediate and high galactic latitudes," *A&A*, vol. 586, p. A133, 2016.

[49] G. P. Holder, M. P. Viero, O. Zahn, K. A. Aird, B. A. Benson, S. Bhattacharya, L. E. Bleem, J. Bock, M. Brodwin, J. E. Carlstrom, C. L. Chang, H.-M. Cho, A. Conley, T. M. Crawford, A. T. Crites, T. de Haan, M. A. Dobbs, J. Dudley, E. M. George, N. W. Halverson, W. L. Holzapfel, S. Hoover, Z. Hou, J. Hrubes, R. Keisler, L. Knox, A. T. Lee, E. M. Leitch, M. Lueker, D. Luong-Van, G. Marsden, D. Marrone, J. J. McMahon, J. Mehl, S. S. Meyer, M. Millea, J. J. Mohr, T. E. Montroy, S. Padin, T. Plagge, C. Pryke, C. L. Reichardt, J. E. Ruhl, J. T. Sayre, K. K. Schaffer, B. Schulz, L. Shaw, E. Shirokoff, H. G. Spieler, Z. Staniszewski, A. A. Stark, K. T. Story, A. van Engelen, K. Vanderlinde, J. D. Vieira, R. Williamson, and M. Zemcov, "A cosmic microwave background lensing mass map and its correlation with the cosmic infrared background," *The Astrophysical Journal Letters*, vol. 771, no. 1, p. L16, 2013.

[50] M. Levi, C. Bebek, T. Beers, R. Blum, R. Cahn, D. Eisenstein, B. Flaugher, K. Honscheid, R. Kron, O. Lahav, P. McDonald, N. Roe, D. Schlegel, and representing the DESI collaboration, "The DESI Experiment, a whitepaper for Snowmass 2013," *ArXiv e-prints*, Aug. 2013.

[51] Y. A. C. A. K. A. C. B. B. B. D. B. A. B. D. B. J. B. S. C. Y. C. A. C. T. d. H. M. A. D. A. D. R. D. T. E. J. E. G. F. S. F. C. F. G. F. A. J. G. N. G.-W. J. G. G. H. N. H. T. H. M. H. K. H. M. H. C. H. W. L. H. Y. H. L. H. F. I. G. J. A. J. O. J. N. K. J. P. K. K. K. B. G. K. Z. K. R. K. T. S. K. A. K. M. L. J.

A. T. L. D. L. E. V. L. L. L. F. M. T. M. N. M. K. M. J. M. M. N. H. N. H. P. J. P. D. P. G. P. C. R. R. G. M. R. C. L. R. P. L. R. C. R. K. M. R. Y. S. B. D. S. I. S. P. S. N. S. R. S. J. S. A. S. O. T. S. T. S. T. G. P. T. A. T. T. T. N. W. A. Z. O. Z. Y. Inoue, P. Ade, "Polarbear-2: an instrument for cmb polarization measurements," 2016.

[52] J. Choi, H. Ishitsuka, S. Mima, S. Oguri, K. Takahashi, and O. Tajima, "Radio-transparent multi-layer insulation for radiowave receivers," *Review of Scientific Instruments*, vol. 84, no. 11, p. 114502, 2013.

[53] P. Siritanasak, C. Aleman, K. Arnold, A. Cukierman, M. Hazumi, K. Kazemzadeh, B. Keating, T. Matsumura, A. T. Lee, C. Lee, E. Quealy, D. Rosen, N. Stebor, and A. Suzuki, "The broadband anti-reflection coated extended hemispherical silicon lenses for polarbear-2 experiment," *Journal of Low Temperature Physics*, vol. 184, pp. 553–558, Aug 2016.

[54] R. DuHamel, "Dual polarized sinuous antennas," Apr. 14 1987. US Patent 4,658,262.

[55] A. Suzuki, K. Arnold, J. Edwards, G. Engargiola, W. Holzapfel, B. Keating, A. T. Lee, X. F. Meng, M. J. Myers, R. O'Brient, E. Quealy, G. Rebeiz, P. L. Richards, D. Rosen, and P. Siritanasak, "Multi-chroic dual-polarization bolometric detectors for studies of the cosmic microwave background," *Journal of Low Temperature Physics*, vol. 176, pp. 650–656, Sep 2014.

[56] K. Hattori, Y. Akiba, K. Arnold, D. Barron, A. N. Bender, A. Cukierman, T. de Haan, M. Dobbs, T. Elleflot, M. Hasegawa, M. Hazumi, W. Holzapfel, Y. Hori, B. Keating, A. Kusaka, A. Lee, J. Montgomery, K. Rotermund, I. Shirley, A. Suzuki, and N. Whitehorn, "Development of readout electronics for polarbear-2 cosmic microwave background experiment," *Journal of Low Temperature Physics*, vol. 184, pp. 512–518, Jul 2016.

[57] D. R. Barron, *Precision measurements of cosmic microwave background polarization to study cosmic inflation and large scale structure.* PhD thesis, UC San Diego, 2015.

[58] D. N. D.B. Rutledge and D. Kasilingam, "Integrated circuit antennas," in *Infrared and Millimeter-Waves, vol.10* (K. Button, ed.), pp. 1–90, New York: Academic Press, 1983.

[59] D. F. Filipovic, S. S. Gearhart, and G. M. Rebeiz, "Double-slot antennas on extended hemispherical and elliptical silicon dielectric lenses," *IEEE Transactions on Microwave Theory and Techniques*, vol. 41, pp. 1738–1749, Oct 1993.

[60] T. H. Buttgenbach, "An improved solution for integrated array optics in quasi-optical mm and submm receivers: the hybrid antenna," *IEEE Transactions on Microwave Theory and Techniques*, vol. 41, pp. 1750–1760, Oct 1993.

[61] J. Lau, J. Fowler, T. Marriage, L. Page, J. Leong, E. Wishnow, R. Henry, E. Wollack, M. Halpern, D. Marsden, and G. Marsden, "Millimeter-wave antireflection coating for cryogenic silicon lenses," *Appl. Opt.*, vol. 45, pp. 3746–3751, Jun 2006.

[62] A. Suzuki, *Multichroic Bolometric Detector Architecture for Cosmic Microwave Background Polarimetry Experiments*. PhD thesis, UC Berkeley, 2013.

[63] R. R. O'Brient, *A Log-Periodic Focal-Plane Architecture for Cosmic Microwave Background Polarimetry.* PhD thesis, UC Berkeley, 2010.

[64] E. E. Quealy, *The Polarbear Cosmic Microwave Background Polarization Experiment and Anti-Reflection Coatings for Millimeter Wave Observations.* PhD thesis, UC Berkeley, 2012.

[65] D. Rosen, A. Suzuki, B. Keating, W. Krantz, A. T. Lee, E. Quealy, P. L. Richards, P. Siritanasak, and W. Walker, "Epoxy-based broadband antireflection coating for millimeter-wave optics," *Appl. Opt.*, vol. 52, pp. 8102–8105, Nov 2013.

[66] D. Kasilingam and D. Rutledge, "Focusing properties of small lenses," *International Journal of Infrared and Millimeter Waves*, vol. 7, pp. 1631–1647, Oct 1986.

[67] R. E. Colin, *Antennas and Radiowave Propagation*, ch. 4.5, pp. 190–194. New York: McGraw-Hill Inc., 1985.

[68] M. Kline and I. Kay, *Electromagnetic theory and geometrical optics*. Pure and applied mathematics, Interscience Publishers, 1965.

[69] A. Ludwig, "The definition of cross polarization," *IEEE Transactions on Antennas and Propagation*, vol. 21, pp. 116–119, Jan 1973.

[70] C. A. Swenson, "Linear thermal expansivity (1.5-300 k) and heat capacity (1.2-90 k) of stycast 2850ft," *Review of Scientific Instruments*, vol. 68, no. 2, pp. 1312–1315, 1997.

[71] K. G. Lyon, G. L. Salinger, C. A. Swenson, and G. K. White, "Linear thermal expansion measurements on silicon from 6 to 340 k," *Journal of Applied Physics*, vol. 48, no. 3, pp. 865–868, 1977.

[72] E. D. Mann, *LNG Materials and Fluids*. National Bureau of Standards, Cryogenics Division, 1977.

[73] O. Jeong, A. Lee, C. Raum, and A. Suzuki, "Broadband plasma-sprayed antireflection coating for millimeter-wave astrophysics experiments," *Journal of Low Temperature Physics*, vol. 184, pp. 621–626, Aug 2016.

[74] R. Datta, C. D. Munson, M. D. Niemack, J. J. McMahon, J. Britton, E. J. Wollack, J. Beall, M. J. Devlin, J. Fowler, P. Gallardo, J. Hubmayr, K. Irwin, L. Newburgh, J. P. Nibarger, L. Page, M. A. Quijada, B. L. Schmitt, S. T. Staggs, R. Thornton, and L. Zhang, "Large-aperture wide-bandwidth antireflection-coated silicon lenses for millimeter wavelengths," *Appl. Opt.*, vol. 52, pp. 8747–8758, Dec 2013.

[75] P. G. P. R. M. S. B. G. C.-M. R. D. C. D. D. J. G. S. G. C. M. J. J. M. C. D. M. M. N. S. P. G. S. Jordan D. Wheeler, Brian Koopman, "Antireflection coatings for submillimeter silicon lenses," 2014.

[76] T. Matsumura, K. Young, Q. Wen, S. Hanany, H. Ishino, Y. Inoue, M. Hazumi, J. Koch, O. Suttman, and V. Schütz, "Millimeter-wave broadband antireflection coatings using laser ablation of subwavelength structures," *Appl. Opt.*, vol. 55, pp. 3502–3509, May 2016.

[77] C. D. D. B. H. E. M. I. H. R. J. A. K. H. G. L. C. M. M. R. M. T. M. H. T. N. J. Z. Loren J. Swenson, Peter K. Day, "Mako: a pathfinder instrument for on-sky demonstration of low-cost 350 micron imaging arrays," 2012.

[78] S.-G. Park, K. Lee, D. Han, J. Ahn, and K.-H. Jeong, "Subwavelength silicon through-hole arrays as an all-dielectric broadband terahertz gradient index metamaterial," *Applied Physics Letters*, vol. 105, no. 9, p. 091101, 2014.

[79] B. D. Sherwin, A. van Engelen, N. Sehgal, M. Madhavacheril, G. E. Addison, S. Aiola, R. Allison, N. Battaglia, D. T. Becker, J. A. Beall, J. R. Bond, E. Calabrese, R. Datta, M. J. Devlin, R. Dünner, J. Dunkley, A. E. Fox, P. Gallardo,

M. Halpern, M. Hasselfield, S. Henderson, J. C. Hill, G. C. Hilton, J. Hubmayr, J. P. Hughes, A. D. Hincks, R. Hlozek, K. M. Huffenberger, B. Koopman, A. Kosowsky, T. Louis, L. Maurin, J. McMahon, K. Moodley, S. Naess, F. Nati, L. Newburgh, M. D. Niemack, L. A. Page, J. Sievers, D. N. Spergel, S. T. Staggs, R. J. Thornton, J. Van Lanen, E. Vavagiakis, and E. J. Wollack, "Two-season atacama cosmology telescope polarimeter lensing power spectrum," *Phys. Rev. D*, vol. 95, p. 123529, Jun 2017.

[80] P. A. R. Ade, Z. Ahmed, R. W. Aikin, K. D. Alexander, D. Barkats, S. J. Benton, C. A. Bischoff, J. J. Bock, R. Bowens-Rubin, J. A. Brevik, I. Buder, E. Bullock, V. Buza, J. Connors, B. P. Crill, L. Duband, C. Dvorkin, J. P. Filippini, S. Fliescher, J. Grayson, M. Halpern, S. Harrison, G. C. Hilton, H. Hui, K. D. Irwin, K. S. Karkare, E. Karpel, J. P. Kaufman, B. G. Keating, S. Kefeli, S. A. Kernasovskiy, J. M. Kovac, C. L. Kuo, E. M. Leitch, M. Lueker, K. G. Megerian, C. B. Netterfield, H. T. Nguyen, R. O'Brient, R. W. Ogburn, A. Orlando, C. Pryke, S. Richter, R. Schwarz, C. D. Sheehy, Z. K. Staniszewski, B. Steinbach, R. V. Sudiwala, G. P. Teply, K. L. Thompson, J. E. Tolan, C. Tucker, A. D. Turner, A. G. Vieregg, A. C. Weber, D. V. Wiebe, J. Willmert, C. L. Wong, W. L. K. Wu, and K. W. Yoon, "Improved constraints on cosmology and foregrounds from bicep2 and keck array cosmic microwave background data with inclusion of 95 ghz band," *Phys. Rev. Lett.*, vol. 116, p. 031302, Jan 2016.

[81] A. A. J. W. A. C. L. B. F. B. M. B. M. C. D. T. C. F. C. S. D. K. D. R. D. J. E. T. E.-H. P. F. M. H. G. H. G. F. H. J. H. J. I. J. K. J. M. N. T. M. S. H. M. G. P. L. P. M. P. B. P. K. R. M. S. D. V. D. W. E. W. Z. X. L. Z. Kathleen Harrington, Tobias Marriage, "The cosmology large angular scale surveyor," 2016.

[82] Z. A. K. D. A. M. A. D. B. S. J. B. C. A. B. J. J. B. H. B. R. B.-R. I. B. E. B. V. B. J. C. J. P. F. S. F. M. H. S. H. G. C. H. V. V. H. H. H. K. D. I. J. K. K. S. K. E. K. S. K. S. A. K. J. M. K. C. L. K. E. M. L. M. L. K. G. M. V. M. T. N. C. B. N. H. T. N. R. O. R. W. O. C. P. C. D. R. S. R. R. S. C. S. C. D. S. Z. K. S. B. S. G. P. T. K. L. T. J. E. T. C. T. A. D. T. A. G. V. A. W. A. C. W. D. V. W. J. W. W. L. K. W. K. W. Y. J. A. Grayson, P. A. R. Ade, "Bicep3 performance overview and planned keck array upgrade," 2016.

[83] K. N. Abazajian, P. Adshead, Z. Ahmed, S. W. Allen, D. Alonso, K. S. Arnold, C. Baccigalupi, J. G. Bartlett, N. Battaglia, B. A. Benson, C. A. Bischoff, J. Borrill, V. Buza, E. Calabrese, R. Caldwell, J. E. Carlstrom, C. L. Chang, T. M. Crawford, F.-Y. Cyr-Racine, F. De Bernardis, T. de Haan, S. di Serego Alighieri,

J. Dunkley, C. Dvorkin, J. Errard, G. Fabbian, S. Feeney, S. Ferraro, J. P. Filippini, R. Flauger, G. M. Fuller, V. Gluscevic, D. Green, D. Grin, E. Grohs, J. W. Henning, J. C. Hill, R. Hlozek, G. Holder, W. Holzapfel, W. Hu, K. M. Huffenberger, R. Keskitalo, L. Knox, A. Kosowsky, J. Kovac, E. D. Kovetz, C.-L. Kuo, A. Kusaka, M. Le Jeune, A. T. Lee, M. Lilley, M. Loverde, M. S. Madhavacheril, A. Mantz, D. J. E. Marsh, J. McMahon, P. D. Meerburg, J. Meyers, A. D. Miller, J. B. Munoz, H. N. Nguyen, M. D. Niemack, M. Peloso, J. Peloton, L. Pogosian, C. Pryke, M. Raveri, C. L. Reichardt, G. Rocha, A. Rotti, E. Schaan, M. M. Schmittfull, D. Scott, N. Sehgal, S. Shandera, B. D. Sherwin, T. L. Smith, L. Sorbo, G. D. Starkman, K. T. Story, A. van Engelen, J. D. Vieira, S. Watson, N. Whitehorn, and W. L. Kimmy Wu, "CMB-S4 Science Book, First Edition," *ArXiv e-prints*, Oct. 2016.

[84] T. Matsumura, Y. Akiba, K. Arnold, J. Borrill, R. Chendra, Y. Chinone, A. Cukierman, T. de Haan, M. Dobbs, A. Dominjon, T. Elleflot, J. Errard, T. Fujino, H. Fuke, N. Goeckner-wald, N. Halverson, P. Harvey, M. Hasegawa, K. Hattori, M. Hattori, M. Hazumi, C. Hill, G. Hilton, W. Holzapfel, Y. Hori, J. Hubmayr, K. Ichiki, J. Inatani, M. Inoue, Y. Inoue, F. Irie, K. Irwin, H. Ishino, H. Ishitsuka, O. Jeong, K. Karatsu, S. Kashima, N. Katayama, I. Kawano, B. Keating, A. Kibayashi, Y. Kibe, Y. Kida, K. Kimura, N. Kimura, K. Kohri, E. Komatsu, C. L. Kuo, S. Kuromiya, A. Kusaka, A. Lee, E. Linder, H. Matsuhara, S. Matsuoka, S. Matsuura, S. Mima, K. Mitsuda, K. Mizukami, H. Morii, T. Morishima, M. Nagai, T. Nagasaki, R. Nagata, M. Nakajima, S. Nakamura, T. Namikawa, M. Naruse, K. Natsume, T. Nishibori, K. Nishijo, H. Nishino, T. Nitta, A. Noda, T. Noguchi, H. Ogawa, S. Oguri, I. S. Ohta, C. Otani, N. Okada, A. Okamoto, A. Okamoto, T. Okamura, G. Rebeiz, P. Richards, S. Sakai, N. Sato, Y. Sato, Y. Segawa, S. Sekiguchi, Y. Sekimoto, M. Sekine, U. Seljak, B. Sherwin, K. Shinozaki, S. Shu, R. Stompor, H. Sugai, H. Sugita, T. Suzuki, A. Suzuki, O. Tajima, S. Takada, S. Takakura, K. Takano, Y. Takei, T. Tomaru, N. Tomita, P. Turin, S. Utsunomiya, Y. Uzawa, T. Wada, H. Watanabe, B. Westbrook, N. Whitehorn, Y. Yamada, N. Yamasaki, T. Yamashita, M. Yoshida, T. Yoshida, and Y. Yotsumoto, "Litebird: Mission overview and focal plane layout," *Journal of Low Temperature Physics*, vol. 184, pp. 824–831, Aug 2016.

[85] P. A. R. Ade, Z. Ahmed, R. W. Aikin, K. D. Alexander, D. Barkats, S. J. Benton, C. A. Bischoff, J. J. Bock, J. A. Brevik, I. Buder, E. Bullock, V. Buza, J. Connors, B. P. Crill, C. D. Dowell, C. Dvorkin, L. Duband, J. P. Filippini, S. Fliescher, S. R. Golwala, M. Halpern, S. Harrison, M. Hasselfield, S. R. Hilde-

brandt, G. C. Hilton, V. V. Hristov, H. Hui, K. D. Irwin, K. S. Karkare, J. P. Kaufman, B. G. Keating, S. Kefeli, S. A. Kernasovskiy, J. M. Kovac, C. L. Kuo, E. M. Leitch, M. Lueker, P. Mason, K. G. Megerian, C. B. Netterfield, H. T. Nguyen, R. O?Brient, R. W. O. IV, A. Orlando, C. Pryke, C. D. Reintsema, S. Richter, R. Schwarz, C. D. Sheehy, Z. K. Staniszewski, R. V. Sudiwala, G. P. Teply, K. L. Thompson, J. E. Tolan, A. D. Turner, A. G. Vieregg, A. C. Weber, J. Willmert, C. L. Wong, K. W. Yoon, K. Array, and B. Collaborations, "Bicep2/keck array v: Measurements of b-mode polarization at degree angular scales and 150 ghz by the keck array," *The Astrophysical Journal*, vol. 811, no. 2, p. 126, 2015.

[86] T. Louis, E. Grace, M. Hasselfield, M. Lungu, L. Maurin, G. E. Addison, P. A. R. Ade, S. Aiola, R. Allison, M. Amiri, E. Angile, N. Battaglia, J. A. Beall, F. de Bernardis, J. R. Bond, J. Britton, E. Calabrese, H. mei Cho, S. K. Choi, K. Coughlin, D. Crichton, K. Crowley, R. Datta, M. J. Devlin, S. R. Dicker, J. Dunkley, R. Dünner, S. Ferraro, A. E. Fox, P. Gallardo, M. Gralla, M. Halpern, S. Henderson, J. C. Hill, G. C. Hilton, M. Hilton, A. D. Hincks, R. Hlozek, S. P. Ho, Z. Huang, J. Hubmayr, K. M. Huffenberger, J. P. Hughes, L. Infante, K. Irwin, S. M. Kasanda, J. Klein, B. Koopman, A. Kosowsky, D. Li, M. Madhavacheril, T. A. Marriage, J. McMahon, F. Menanteau, K. Moodley, C. Munson, S. Naess, F. Nati, L. Newburgh, J. Nibarger, M. D. Niemack, M. R. Nolta, C. Nuñez, L. A. Page, C. Pappas, B. Partridge, F. Rojas, E. Schaan, B. L. Schmitt, N. Sehgal, B. D. Sherwin, J. Sievers, S. Simon, D. N. Spergel, S. T. Staggs, E. R. Switzer, R. Thornton, H. Trac, J. Treu, C. Tucker, A. V. Engelen, J. T. Ward, and E. J. Wollack, "The atacama cosmology telescope: two-season actpol spectra and parameters," *Journal of Cosmology and Astroparticle Physics*, vol. 2017, no. 06, p. 031, 2017.